Department of Physics and Astronomy

University of Heidelberg

Master thesis

in Physics

submitted by

Sascha Simon Dreyer

born in Göttingen

2019

Statistical Combination of Searches for Invisible Higgs Boson Decays with the ATLAS Experiment

This Master thesis has been carried out by

Sascha Simon Dreyer

at the

Kirchhoff-Institute for Physics

under the supervision of

Herrn Priv.-Doz. Dr. Oleg Brandt

Statistische Kombination von Suchen nach unsichtbaren Zerfällen des Higgs Bosons mit dem ATLAS Detektor

Das Standardmodell (SM) sagt unsichtbare Zerfälle des Higgs Bosons über den $H \to ZZ^* \to 4\nu$ Kanal mit einem Verzweigungsverhältnis von $\approx 10^{-3}$ voraus – zu klein, um es am Großen Hadronenbeschleuiger (LHC) nachzuweisen. Mehrere Erweiterungen des SM sagen indes unsichtbare Zerfälle des Higgs Bosons in Dunkle Materie-Teilchen voraus. Nach solchen Zerfällen wird mit dem ATLAS Detektor in den Vektor-Boson-Fusions- (VBF) und Higgsstrahlungstopologien (ZH, WH) gesucht. Präsentiert werden eine statistische Kombination der Suchen in VBF, $Z(\to \text{Leptonen})H$ und $V(\to \text{Hadronen})H$ Topologien mit 36 fb^{-1} von Proton-Proton Kollisionsdaten bei einer Schwerpunktsenergie von $\sqrt{s} = 13\,\text{TeV}$ aus der zweiten Datennahmeperiode des LHCs, sowie die Kombination mit den Ergebnissen der ersten Datennahmeperiode des LHCs bei $\sqrt{s} = 7\,\text{TeV}$ und $8\,\text{TeV}$. In der Gesamtkombination wird eine Ausschlussgrenze auf das unsichtbare Verzweigungsverhältnis des Higgs Bosons von 0.26 ($0.17^{+0.07}_{-0.05}$) auf einem Konfidenzniveau von 95% beobachtet (erwartet). Ein besonderer Fokus liegt auf der Konstruktion eines Modells zur Korrelation der verschiedenen Quellen von systematischer Unsicherheit. Die Ergebnisse werden im Rahmen von Higgs-Portal Modellen mit Ausschlussgrenzen anderer Experimente, die auf dem Prinzip der direkten Detektion beruhen, verglichen, wobei eine individuelle Komplementarität der Ansätze festgestellt wird.

Statistical Combination of Searches for Invisible Higgs Boson Decays with the ATLAS Experiment

The Standard Model (SM) predicts invisible decays of the Higgs boson via the $H \to ZZ^* \to 4\nu$ channel with a branching ratio of $\approx 10^{-3}$, too small to be experimentally confirmed at the Large Hadron Collider (LHC). Several extensions of the SM predict invisible decays of the Higgs boson to Dark Matter particles. Such decays are searched for using the ATLAS detector in the Vector-Boson-Fusion (VBF) and Higgsstrahlung (ZH, WH) topologies. A statistical combination of searches in the VBF, $Z(\to \text{leptons})H$ and $V(\to \text{hadrons})H$ topologies with 36 fb^{-1} of proton-proton collision data from the second data-taking period of the LHC at a centre-of-mass energy of $\sqrt{s} = 13\,\text{TeV}$, as well as the combination with results from the first data-taking period of the LHC at $\sqrt{s} = 7\,\text{TeV}$ and $8\,\text{TeV}$ are presented. An upper exclusion limit on the invisible branching ratio of the Higgs boson of 0.26 ($0.17^{+0.07}_{-0.05}$) is observed (expected) at a confidence level of 95% in the total combination. A special focus is placed on the construction of the correlation model between the various sources of systematic uncertainty. The results are compared to exclusion limits from other experiments based on the principle of direct detection using the framework of Higgs portal models, which indicates individual complementarity of the approaches.

Contents

1. Introduction and Motivation

The Higgs boson was predicted in the mid 1960's and observed experimentally in 2012 by the ATLAS [1] and CMS [2] collaborations at the Large Hadron Collider (LHC) located at the European Organization for Nuclear Research (CERN). Interactions with the Higgs boson constitute the fundamental mechanism by which elementary particles acquire their rest mass in the Standard Model of Particle Physics (SM).

It is now of great interest to further investigate the properties of the Higgs boson, particularly its couplings to the SM fermions and gauge bosons. Another important test of the Higgs sector are potential decays to particles that do not interact electromagnetically or strongly with the detector material, called invisible. The SM predicts such decays via $H \to ZZ^\star \to 4\nu$ with a branching ratio of around 0.1 %, below the sensitivity of current experiments. A significantly higher invisible branching fraction of the Higgs boson $\mathcal{B}_{H\to\text{inv}}$ would thus be a clear sign for couplings to yet unobserved realms of nature.

One of the currently most sought after phenomena in physics is dark matter (DM), accounting for around five times the mass of the known baryonic matter in the universe. No experimental observation clarifies the nature of DM yet, although there is a wealth of astrophysical evidence for its existence. The theoretical framework of Higgs portal models connect the Higgs boson directly to particle candidates for DM that could account for these astrophysical effects. It is motivated by the fact that the Higgs boson couples to mass and DM is known to be massive. This type of link would allow the Higgs boson to decay invisibly to pairs of DM particles if kinematically accessible. Stringent experimental limits on $\mathcal{B}_{H\to\text{inv}}$ could thus help to shed light on the dark sector and its interplay with the known universe.

Searches for invisible decays at hadron colliders involve the experimental signature of missing transverse momentum $E_{\text{T}}^{\text{miss}}$, which indirectly indicates a particle that escaped detection. The ATLAS collaboration performed searches for invisible decays of the Higgs boson in different event topologies assuming SM Higgs boson production: vector boson fusion (VBF), Higgsstrahlung from a Z boson decaying into charged leptons ($Z_{\ell\bar{\ell}}H$), and Higgsstrahlung from a W or Z boson decaying into hadrons ($V_{q\bar{q}}H$). A statistical combination of results from these searches conducted using LHC Run 1 data was performed [3]. More recently, direct searches were conducted using 36 fb^{-1} of pp collision data recorded 2015 and 2016 by ATLAS as part of LHC Run 2, in the VBF [4], $Z_{\ell\bar{\ell}}H$ [5] and $V_{q\bar{q}}H$ [6] topologies (referred to as Run 2 results in the following). The CMS collaboration performed similar searches [7–11].

This Thesis presents the statistical combination of the Run 2 searches for invisible decays of the Higgs boson using the ATLAS detector. Subsequently, a statistical combination with the combined Run 1 result [3] from ATLAS is performed. The combined upper limit on $\mathcal{B}_{H\to\text{inv}}$ is compared to results from direct detection experiments using the framework of Higgs portal models. The impact of different categories of systematic

uncertainty on the resulting limit and fitted invisible branching ratio is estimated. Cross-checks are performed on the combined result including scans of the likelihood functions, rankings of systematic uncertainties, alternative correlation assumptions, and the compatibility between results of both studied LHC Runs. The results presented in this Thesis are submitted for publication [12].

The Thesis is structured as follows: The SM is introduced together with the phenomenon of DM and experimental search techniques in Chapter 2. The LHC and the ATLAS detector are described in Chapter 3. Subsequently, the methodology behind the statistical interpretation and combination of the searches is discussed in Section 4.1 and 4.1.3. The terminology for reconstructed objects in ATLAS searches is explained in Section 4.2. The searches forming the input to the statistical combination with their event selections and treatment of systematic uncertainties are introduced in Chapter 5. An important part of a combination of search results is the consideration of correlations between systematic uncertainties. The correlation model that is used in the statistical combinations is presented in Section 6.1. Combination results for Run 2 are discussed in Section 6.2 and for Run 1+2 in Section 6.3. The Thesis concludes with a summary of the studies and an outlook to forthcoming results in Chapter 7.

1.1. Authors Contribution

The work in a collaboration such as ATLAS is always a shared effort of many individuals. A lot of the work that is discussed in the context of this Thesis was performed in collaboration with others. This section clarifies the contribution of the author to the studies and results presented in this Thesis.

The input analyses to the statistical combinations, in particular the searches and the combination performed using LHC Run 1 data as well as the described Run 2 searches for invisible decays of the Higgs boson shown in Chapter 5 were performed by different analyses groups of the ATLAS collaboration and the author did not take part in these.

The work the author performed includes the identification of a suitable correlation model for the systematic uncertainties of the searches in Section 6.1, with the cross-checks to justify these correlation assumptions shown in Appendix B. The author performed the actual statistical combination and set upper exclusion limits on $\mathcal{B}_{H\to\text{inv}}$ using ATLAS software in Section 6.2 and 6.3. This includes in particular, the comparison of the combinations in terms of the rankings, correlations and profiled values of the systematic uncertainties, between the input analyses as discussed in Sections 6.2.3 and 6.3.3 as well as Appendix D. The author performed the scans of the likelihood functions shown in Sections 6.2.1 and 6.3.1, and the estimation of the impact of systematic uncertainty sources on the final result in Sections 6.2.4 and 6.3.5. The evaluation of the compatibility between the Run 1 and 2 combinations shown in Section 6.3.6 was performed by the author. The translation of the limit on the branching fraction into limits on the WIMP - nucleon cross section in terms of Higgs portal models in Section 6.3.7 was studied in collaboration with Tae Min Hong (U. of Pittsburgh). The code that was written and adapted by the author in context of the combination can be used by ATLAS collaborators to perform future combinations of searches for DM.

2. Theoretical Framework

This chapter gives an introduction into the theoretical framework of the Standard Model of Particle Physics, which is discussed in Section 2.1, as well as into the phenomenon of Dark Matter, described in Section 2.2.

2.1. The Standard Model

The *Standard Model of Particle Physics* (SM) emerged during the $60's$ as a relativistic quantum field theory with major contributions from Weinberg, Glashow and Salam [13–15]. It describes three of the four known fundamental interactions, the strong, weak and electromagnetic forces. There is no existing theory that fully includes gravity as a quantum field theory, though there are attempts at large scales such as String Theory. The predictions of the SM describe most of the experimental data [16]. However, certain observations cannot be explained by the SM. These include the observed large matter - antimatter asymmetry, oscillation of neutrino flavours leading to massive neutrinos, and Dark Matter.

The SM relies on invariance of the Lagrange density under local gauge transformations of the fields. The corresponding equations of motion are obtained from the principle of least action. The underlying symmetries can be described in terms of Lie groups. In the SM, these are

$$\mathbb{SU}(3)_C \otimes \mathbb{SU}(2)_L \otimes \mathbb{U}(1)_Y. \tag{2.1}$$

Here, C stands for the colour-charge quantum number of the strong interaction, L for the left-handed nature of the weak interaction and Y for the hypercharge quantum number associated to the $\mathbb{U}(1)$ symmetry. The generators of the symmetry groups in the adjoint representation enter observations as spin 1 gauge bosons mediating the interaction between fermionic matter particles. The Lagrange density of the SM is given by (in compact notation):

$$\mathcal{L}_{SM} = -\frac{1}{4}F^{\mu\nu}F_{\mu\nu} + \bar{\psi}(\not{\mathcal{D}} - m)\psi - \frac{1}{2}\mathcal{D}_\mu\mathcal{D}^\mu\phi - V(\phi) + h.c\,, \tag{2.2}$$

where $F_{\mu\nu}$ are the field strength tensors of the gauge boson fields, $\mathcal{D}_\mu$ the covariant derivative including the gauge fields, $\not{\mathcal{D}} = \gamma_\mu\mathcal{D}^\mu$ the contraction of the covariant derivative with the gamma matrices, ϕ the Higgs field, and $V(\phi)$ the potential of the Higgs field.

2.1.1. Bosonic Sector

The SM Lagrange density term describing a free massless vector field A_μ is:

$$\mathcal{L}_{boson} = -\frac{1}{4}F^{\mu\nu}F_{\mu\nu}\,, \tag{2.3}$$

where the field strength tensor can be obtained from the commutator of the covariant derivative $\mathcal{D}_\mu = \partial_\mu - ig_A A_\mu$ including the bosonic vector field A_μ and the strength of the corresponding interaction g_A via $F_{\mu\nu} = \frac{i}{g_A}[\mathcal{D}_\mu, \mathcal{D}_\nu]$. Under a local gauge transformation with an element $U(x)$ of the Lie group corresponding to the gauge boson, the vector field transforms as follows:

$$gA_\mu \rightarrow iU(x)\mathcal{D}_\mu U^\dagger(x)\,. \tag{2.4}$$

For a Lie group, the transformation can be written in terms of generators of the corresponding Lie algebra $w(x)$:

$$U(x) = e^{iw(x)}\,. \tag{2.5}$$

Considering an infinitesimal transformation, the gauge field thus has to be an element of the Lie algebra. There are $N^2 - 1$ generators of the adjoint representation in a $\mathbb{SU}(\mathrm{N})$ group. This corresponds to eight colour charged gluons for $\mathbb{SU}(3)_C$, three weak bosons $W_{1,2,3}$ for $\mathbb{SU}(2)_L$. The $\mathbb{U}()_Y$ generator is the neutral boson B^0. The bosonic part of the SM Lagrange density thus includes an implicit sum over all gauge fields belonging to the gauge group. The gauge symmetry forbids a mass term for the bosons, $m_A A_\mu A^\mu$, connecting the gauge field to itself. Without a further mechanism, gluons, the W_i and the B^0 are therefore massless. The physical electroweak gauge bosons $W^\pm$, Z and the photon γ correspond to linear combinations of $\mathbb{SU}(2)_L$ and $\mathbb{U}(1)_Y$ generators. These are obtained after including a scalar Higgs field and spontaneously breaking the electroweak symmetry as will be described in Section 2.1.3. This gives rise to mass terms for the electrically charged $W^\pm$ and the neutral Z fields while the neutral photon remains massless. The bosonic sector of the SM is listed in Table 2.1.

	Mass	Q_{EM}	Discovery
W^+	80.385 ± 0.015	$+1$	1983
W^-	80.385 ± 0.015	-1	1983
Z	91.1876 ± 0.0021	0	1983
γ	0	0	ca. 1900
Gluons	0	0	1979
H	125.09 ± 0.24	0	2012

Table 2.1.: Table of elementary bosons in the SM where Q_{EM} describes the electric charge. Values taken from [16].

2.1.2. Fermionic Sector

Fermionic particles in the SM are described by spinor fields ψ. These contain particle and antiparticle fields, hence there is a corresponding anti-fermion to every fermion in the SM with an inverse charge-like quantum number. The Lagrange density of a free massless fermionic field is given by:

$$\mathcal{L}_{fermion} = \bar{\psi}\gamma_\mu\partial^\mu\psi \equiv \bar{\psi}\not{\partial}\psi\,, \tag{2.6}$$

where the adjoint spinor $\bar{\psi}$ is defined by $\bar{\psi} = \psi^\dagger \gamma^0$. Fermionic fields can be de-composed into left- and right-handed chiral states $\psi_{L/R}$. The left-handed state of particles and the right-handed state of antiparticles obtain a $\mathbb{SU}(2)$ quantum number called weak isospin T_3. The $W^\pm$ as well as the $\mathbb{SU}(2)$ part of the Z and γ couple to the weak isospin. The other chiral state does not interact with the charged $W^\pm$. The transformation behaviour of fermions is exemplary shown for a $\mathbb{U}(1)$ field A_μ, such as the SM photon, with corresponding gauge transformation $U(x)$:

$$\psi \to U(x)\,\psi = e^{iA_\mu(x)}\,\psi\,. \tag{2.7}$$

To ensure invariance of the fermionic Lagrange density 2.6 under transformations of the SM gauge groups the partial derivative is replaced by a covariant derivative $\mathcal{D}_\mu$ including the A_μ field corresponding to the gauge groups generator:

$$\bar{\psi}\not{\partial}\psi \to \bar{\psi}\gamma_\mu(\partial^\mu - igA^\mu)\psi \equiv \bar{\psi}\not{\mathcal{D}}\psi\,. \tag{2.8}$$

The invariance of this equation under gauge transformations is ensured by the transformation properties for bosonic 2.4 and fermionic 2.7 fields. This introduces interaction terms, that are proportional to $ig_A\bar{\psi}A_\mu\psi$, between fermionic and bosonic particles with a coupling strength g_A. The fermionic part of the SM Lagrange density 2.2 sums over all fermions and the covariant derivative include all gauge fields the individual fermions couple to. The free fermionic Lagrange density does not allow for a mass term of the form $m_{\bar{\psi}}^2(\bar{\psi_L}\psi_R + \bar{\psi_R}\psi_L)$ due to gauge symmetry similar to the bosonic case.

Quarks are fermions interacting with all gauge bosons. This is implemented by non-trivial gauge transformations of quark fields for all SM symmetry groups. The transformation behaviours of quark fields are:

- As a $\mathbb{SU}(3)_C$ triplet carrying the three different colour charges.
- The left-handed fields transforms as $\mathbb{SU}(2)_L$ doublet formed by an up- u and a down-type d quark:

  $$Q_L = \begin{pmatrix} u \\ d \end{pmatrix}_L\,. \tag{2.9}$$

  The upper part of the doublet transforms with the weak quantum number $T_3 = +1/2$, the lower part with $T_3 = -1/2$. The right handed quark fields u_R and d_R is a singlet under $\mathbb{SU}(2)_L$.
- The Q_L transform under $\mathbb{U}(1)_Y$ with hypercharge $Y = 1/6$. The u_R (d_R) transform with $Y = +2/3\,(-1/3)$.

Experimentally observed are three generations of fermions, increasing in mass. The up-type quarks are called *up* (u), *charm* (c) and *top* (t) while the down-types are called *down* (d), *strange* (s), and *bottom* or *beauty* (b).

Leptons are fermions with weak and electromagnetic but without colour charge, thus interacting with all gauge bosons but gluons. The transformation behaviours of lepton fields are:

- As singlets under $\mathbb{SU}(3)_C$.
- The left-handed fields transform as $\mathbb{SU}(2)_L$ doublet formed by a neutrino ν and a charged lepton ℓ:

$$\ell_L = \begin{pmatrix} \nu_\ell \\ \ell \end{pmatrix}_L . \tag{2.10}$$

  Neutrinos in the SM have only a left-handed chiral state and thus are massless. The weak quantum numbers are assigned analogous to the left-handed quark field Q_L.
- The ℓ_L transform under $\mathbb{U}(1)_Y$ with $Y = -1/2$. Right-handed charged leptons e_R transform with $Y = -1$, and neutrinos with $Y = -1/2$.

The charged leptons of the three mass generations are called *electron* (e), *muon* (μ) and *tau* (τ). Neutrinos are referred to by the charged lepton of their generation (ν_e, ν_μ and ν_τ). The fermionic sector of the SM is listed in Table 2.2.

		Mass	Q_{EM}	Discovery
Leptons	ν_e	$< 2.2\,\text{eV}$	0	1956
	e	$0.511 \pm 10^{-8}\,\text{MeV}$	-1	1897
	ν_μ	$< 0.19\,\text{MeV}$	0	1962
	μ	$105.7 \pm 4 \otimes 10^{-6}\,\text{MeV}$	-1	1936
	ν_τ	$< 18.2\,\text{MeV}$	0	2000
	τ	$1776.86 \pm 0.12\,\text{MeV}$	-1	1975
Quarks	u	$2.3 \pm 0.7\,\text{MeV}$	$+\frac{2}{3}$	1968
	d	$4.8 \pm 0.5\,\text{MeV}$	$-\frac{1}{3}$	1968
	c	$1.275 \pm 0.025\,\text{GeV}$	$+\frac{2}{3}$	1974
	s	$95 \pm 5\,\text{MeV}$	$-\frac{1}{3}$	1968
	t	$173.2 \pm 0.9\,\text{GeV}$	$+\frac{2}{3}$	1995
	b	$4.18 \pm 0.03\,\text{GeV}$	$-\frac{1}{3}$	1977

Table 2.2.: Table of elementary fermions in the SM where Q_{EM} describes the electric charge. Values taken from [16].

2.1.3. Higgs Sector

The Higgs field [17, 18] was introduced to generate mass terms for fermions and the electroweak gauge bosons by spontaneously breaking the electroweak symmetry. The SM Lagrange density terms for the complex scalar Higgs field ϕ are given by:

$$\mathcal{L}_H = \frac{1}{2}\mathcal{D}_\mu \mathcal{D}^\mu \phi - V(\phi)\,, \tag{2.11}$$

where ϕ is an electroweak doublet which is composed of an electrically charged and a neutral field:

$$\phi = \begin{pmatrix} \phi^+ \\ \phi^0 \end{pmatrix} . \tag{2.12}$$

Four different degrees of freedom result from $\phi^\dagger$ being independent of ϕ. The Higgs field couples to the $\mathbb{SU}(2)_L$ and $\mathbb{U}(1)_Y$ gauge fields which are summed over in the covariant derivative $\mathcal{D}_\mu$. Of particular interest is the form of the Higgs potential:

$$V(\phi) = \mu^2 \phi^\dagger \phi + \lambda (\phi^\dagger \phi)^2 , \tag{2.13}$$

with negative value of μ^2 and a positive λ. The potential possesses a finite minimum or vacuum expectation value (VEV) v_0 at:

$$v_0 \equiv \langle \phi \rangle = \sqrt{\frac{-\mu^2}{\lambda}} . \tag{2.14}$$

Electroweak Symmetry Breaking

The $\mathbb{SU}(2)_L \otimes \mathbb{U}(1)_Y$ symmetry is spontaneously broken to $\mathbb{U}(1)_{EM}$ when the Higgs field settles in the minimum of its potential. This refers to the invariance under $\mathbb{U}(1)$ transformations with a charge of $Q_{EM} = T_3 + Y$, which the Lagrange density possesses in the broken Higgs phase. The physical Higgs boson h is described by a perturbation of the Higgs field in the direction perpendicular to the minimum. A common choice is to expand around the neutral entry of ϕ. The field can now be represented in polar form as:

$$\phi(x) = \frac{(h(x) + v_0)}{\sqrt{2}} \exp(i\sigma(x)/v_0) , \tag{2.15}$$

where the $\sigma(x)$ are called Goldstone bosons and describe the remaining directions of the Higgs field. They are absorbed by a redefinition of the electroweak gauge fields, thereby interpreted as additional longitudinal degrees of freedom. A $\mathbb{SU}(2)_L$ gauge transformation, referred to as unitary gauge, is employed to write:

$$\phi(x) = \frac{1}{\sqrt{2}} \begin{pmatrix} 0 \\ h(x) + v_0 \end{pmatrix} . \tag{2.16}$$

The Higgs boson mass and self-interaction terms are obtained by inserting this equation into the Higgs Lagrange density in 2.11 and expanding the potential. The mass term is given by:

$$m_h = \sqrt{2\lambda} v_0 . \tag{2.17}$$

Electroweak Gauge Boson Masses and Couplings to the Higgs Boson

To obtain the mass terms of the electroweak gauge bosons, the following definitions are used:

$$\begin{aligned} W^\pm &= W_1 \mp i W_2 , \\ \cos\theta_W &= \frac{g}{\sqrt{g^2 + g'^2}} , \\ \begin{pmatrix} \gamma \\ Z \end{pmatrix} &= \begin{pmatrix} \cos\theta_W & \sin\theta_W \\ -\sin\theta_W & \cos\theta_W \end{pmatrix} \begin{pmatrix} B^0 \\ W_3 \end{pmatrix} , \end{aligned} \tag{2.18}$$

where B^0 and the interaction strength g correspond to $\mathbb{U}(1)_Y$, and g' describes the interaction strength of $\mathbb{SU}(2)_L$. The Weinberg angle θ_W is a free parameter of the model and is measured experimentally. The expansion of the kinetic term in the broken phase of the Higgs Lagrange density in 2.11 yields:

$$\begin{aligned} m_\gamma &= 0 \\ m_W &= \frac{g' v_0}{2} \\ m_Z &= \frac{m_W}{\cos\theta_W} \end{aligned} \tag{2.19}$$

The coupling strengths describing the radiation of the Higgs boson from a W or Z boson, $2ig_{\mu\nu}M^2_{W/Z}/v_0$, follow from the same expansion and using the Minkowski metric $g_{\mu\nu}$.

Fermion Masses

Fermion masses are obtained by forming $\mathbb{SU}(2)_L \otimes \mathbb{U}(1)_Y$ singlets from the Higgs doublet and fermion fields. With the definition of $\tilde{\phi} = i\sigma_2\phi^\star$, where the Pauli matrix σ_2 was used, the mass terms for SM fermions are be obtained in the broken Higgs boson phase. By implicitly summing over fermion generations:

$$Y_\ell \bar{\ell_L} \phi e_R + Y_u \bar{Q_L} \tilde{\phi} u_R + Y_d \bar{Q_L} \phi d_R + h.c.\,. \tag{2.20}$$

The Y_i are called Yukawa couplings and describe the strength of the interaction between the Higgs and the fermion i, thus setting its mass relative to the Higgs VEV:

$$m_i = Y_i \frac{v_0}{\sqrt{2}}\,. \tag{2.21}$$

Higgs Boson Production

The Higgs boson can be produced through its couplings to massive particles. At the Large Hadron Collider (LHC), bunches of protons are brought to collision with each other at different centre-of-mass energies $\sqrt{s}$. The amount of data is described in by the integrated luminosity $\mathcal{L}_{\text{int}}$ which is defined as the proportionality factor between the expected number of interactions N and the cross section σ for a specific process,

$$N = \mathcal{L}_{\text{int}}\sigma\,. \tag{2.22}$$

The running periods of the ATLAS detector together with the corresponding centre-of-mass energies and recorded luminosities are given in Table 2.3.

The production of the Higgs boson at the LHC depends on the structure of the colliding protons. The proton consists of two u and one d quark, determining the quantum numbers of the proton. Probed at large energy scales, the proton features gluons and sea quarks ($q\bar{q}$ pairs) with low momentum fraction of the proton. The *Parton Distribution Functions* (PDFs) describe the distributions of proton constituents (partons) as a function of the momentum fraction. These have to be taken into account for predictions. PDFs can be measured e.g. by deep inelastic scattering experiments such as performed at the HERA

Run	Year	$\sqrt{s}$	$\mathcal{L}_{\text{int}}$
1	2011	7 TeV	$4.7\,\text{fb}^{-1}$
	2012	8 TeV	$20.3\,\text{fb}^{-1}$
2	2015+2016	13 TeV	$36.1\,\text{fb}^{-1}$
	2017+2018	13 TeV	$107.5\,\text{fb}^{-1}$

Table 2.3.: List of data taking periods of the ATLAS detector with corresponding centre-of-mass energies and recorded luminosity. The Run 2 periods are split since the searches combined in this Thesis use the 2015+2016 data set.

collider [19]. Due to the large centre-of-mass energies at the LHC, sea quarks and gluons can produce heavy particles despite their small fraction of the overall momentum.

The main production modes of the Higgs boson at the LHC together with the corresponding cross section predictions [20] for the LHC at $\sqrt{s} = 13\,\text{TeV}$ are:

- the fusion of two gluons into a top quark loop coupling to the Higgs boson (gluon-gluon fusion or ggF channel), with $\sigma_{\text{ggF}} = 48.61\,\text{pb}$.
- the fusion of two vector bosons that have been radiated off initial state quarks (vector boson fusion or VBF channel), with $\sigma_{\text{VBF}} = 3.77\,\text{pb}$.
- the associated production with a vector V boson (either W or Z) radiating off a Higgs boson (VH channel or associated production), with $\sigma_{WH} = 1.36\,\text{pb}$ and $\sigma_{ZH} = 0.88\,\text{pb}$.
- the splitting of two gluons into top pairs with one top pair annihilating into a Higgs boson (ttH channel), with $\sigma_{ttH} = 0.61\,\text{pb}$.

Feynman diagrams of these channels are shown in Figure 2.1.

Decays of the Higgs and Electroweak Bosons

The Higgs couplings to fermions are proportional to the fermion masses, thus the Higgs boson decays preferably to heavy particles if kinematically accessible. Decays to pairs of V bosons work at rest with one vector boson on mass-shell and the second off-shell. Gluons and photons do not couple directly to the Higgs boson, thus requiring an additional loop of heavy fermions (predominantly tops), similar to the production via ggF. The main decay modes [16] are with decreasing branching ratio: pairs of b quarks, W bosons, gluons, and τ leptons.

The decay modes of the electroweak W and Z bosons [16] are important for the searches combined here. The primary decay mode of both bosons is to pairs of quarks (hadronic) with a branching ratio of close to 70%. The W boson decays to charged leptons and the associated neutrinos with a branching ratio of around 10% per generation. The Z boson decays leptonically to charged leptons pairs with a branching ratio of slightly above 3% per generation, or invisibly to pairs of neutrinos with a branching ratio of close to 20%.

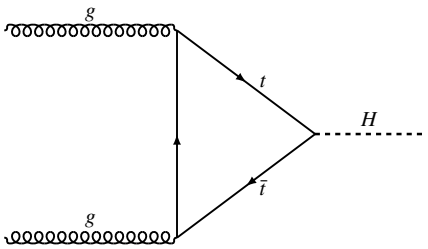

(a) Gluon gluon fusion (ggF).

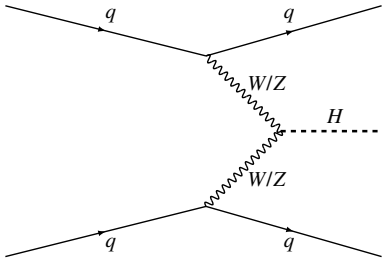

(b) Vector boson fusion (VBF).

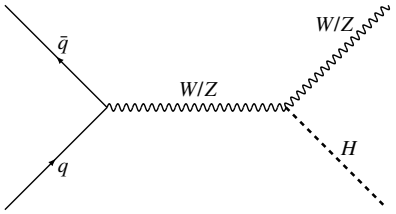

(c) Associated production (VH).

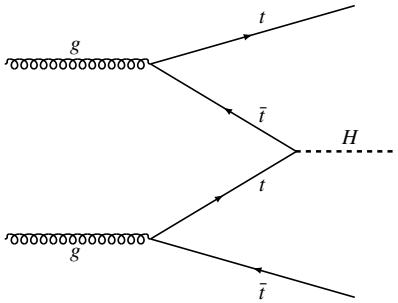

(d) Top pair associated (ttH).

Figure 2.1.: Feynman diagrams of the main Higgs boson production modes at the LHC together.

2.2. Dark Matter

Several astrophysical and cosmological observations indicate the existence of large amounts of non-luminous matter, called Dark Matter (DM), and are briefly discussed in 2.2.1. Strategies for particle DM detection are described in Section 2.2.2 based on [21–23]. Higgs Portal models can be used as a possible interpretation of invisible Higgs boson decays and are introduced in Section 2.2.3.

2.2.1. Astrophysical Evidence

Evidence for DM was found in several analyses that are not directly related to each other and probe dissimilar observables as well as length and energy scales.

Galaxy Rotation Curves

The rotation of matter such as stars around the centre of galaxies can be approximated with Newtonian dynamics. Setting the centripetal force equal to the gravitational attraction predicts for the rotational velocity as a function of the radial distance to the centre:

$$v(r) = \sqrt{\frac{GM(r)}{r}}\,, \tag{2.23}$$

where G describes the gravitational constant and $M(r)$ is the total mass within the radius r. The expected velocity should thus drop proportional to $\frac{1}{\sqrt{r}}$ outside the spherical bulk constituted by stars, accounting for most of the visible matter. The observed mass distribution in contrast scales like $M(r) \propto r$ up to large radii outside the luminous bulk [24]. A possible explanation are large halos of DM around galaxies that modify the overall mass distribution. Further explanatory ansatzes include the modification of either Newtonian gravity or general relativity but fail to simultaneously explain other observations. The observed distribution and predictions for visible and dark matter are shown in Figure 2.2.

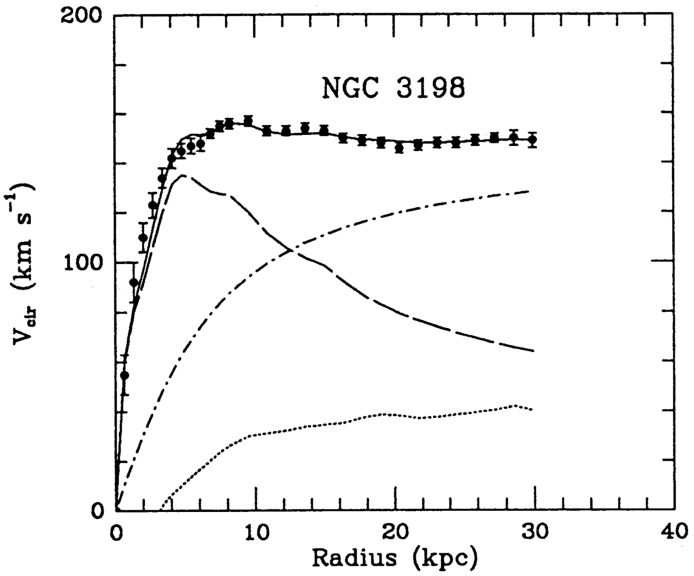

Figure 2.2.: Galactic rotation curve from the spiral galaxy NGC 3198 [24]. Experimental observation (points), predictions for the visible component (dashed curve), for the gas (dotted line), for the dark-halo (dashed-dotted), and for a fit of all three components to the observation (solid).

Cosmic Microwave Background

The Cosmic Microwave Background (CMB) consists of photons that were produced when the hot plasma cooled enough to form neutral atoms, and photons could traverse freely. The temperature in the universe at this point was around 3000 K. The distribution of the relic photons produced in this era was measured by the PLANCK collaboration [25]. The relic photons cooled down since the decoupling due to the further expansion of the universe and match today a black body spectrum at 2.2725 ± 0.0006 K. A map of the CMB is shown in Figure 2.3. The angular distribution of the relic photons is nearly isotropic featuring small anisotropies that can be parametrised by an expansion into spherical harmonic modes. The zeroth mode corresponds to the CMB temperature, the first mode to the largest anisotropy caused by the velocity of the solar system with respect to the CMB. Higher modes can be described by thermal quantum fluctuations in the density of the universe at the time of decoupling, that expanded over time to observable sizes. However,

baryonic density fluctuations alone are not sufficient to explain the observed anisotropies. Additional fluctuations in the DM density can account for the discrepancy and a DM relic density was derived from these considerations by the PLANCK collaboration to $\Omega_\chi h^2 = 0.1186 \pm 0.0020$ [25]. The relic density of baryonic matter by contrast amounts to around a fifth $\Omega_b h^2 = 0.02222 \pm 0.00023$.

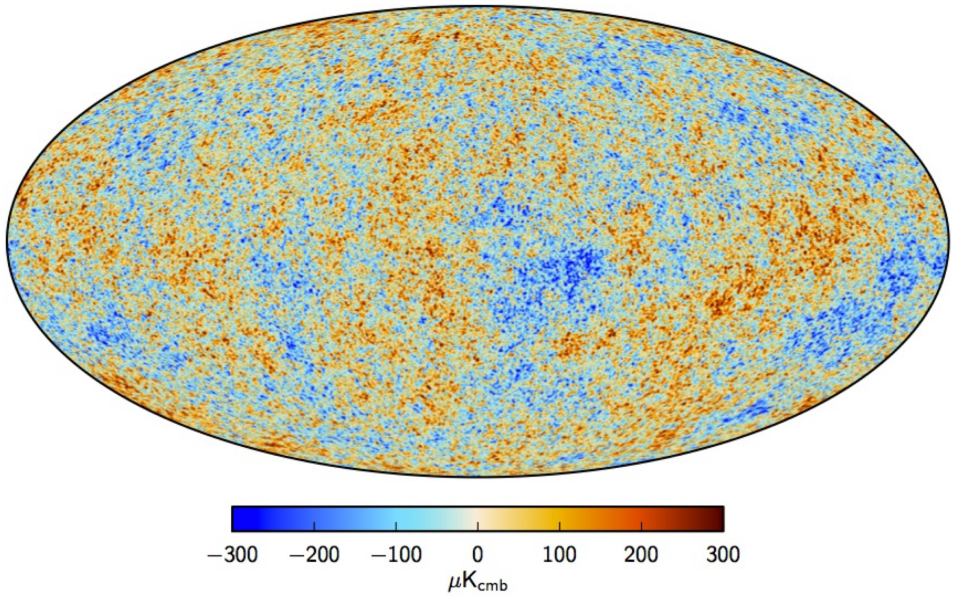

Figure 2.3.: A map of the dipole subtracted Cosmic Microwave Background [25].

Bullet Cluster

The Bullet Cluster 1E 0657-558 [22] consists of two clusters that collided and are currently passing through each other. Indication for the existence of DM is based on the interplay of optical, x-ray and gravitational lensing data of this system. Hot gas clouds can be measured in the x-ray spectrum and interact electromagnetically, thus slowing down each other significantly and producing an observable shock front. The hot gas clouds amount for a dominant fraction of the visible matter in the clusters, thus gravitational lensing measurements should indicate the mass distributions to be centred around the gas clouds. In contrary, gravitational lensing data [26] shows that most of the mass is distributed in halos around the optically visible parts of the clusters. These parts pass through each other nearly unaffected due to the large distances between the objects that interact dominantly gravitational. Dark matter halos around these galaxies that interact gravitationally but not electromagnetically can, unlike modifications of gravity, describe this observation [26]. Figure 2.4 shows the colliding clusters in the three spectra.

Nature of DM

The common and strongest conclusion is the existence of a yet unknown type of matter that interacts gravitationally (thus massive) with structures formed by SM particles.

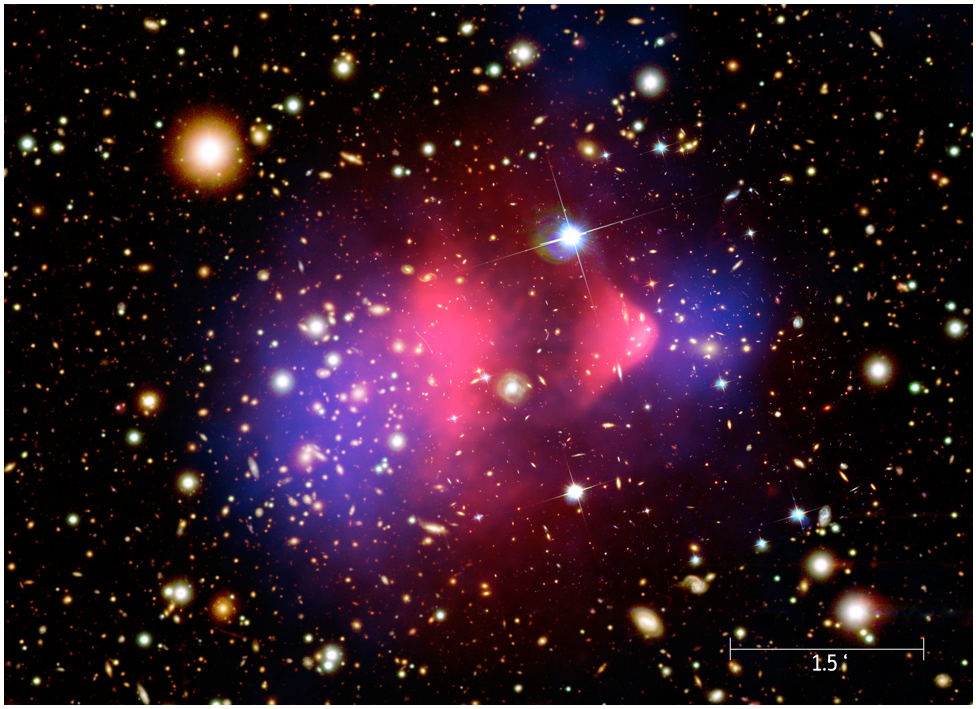

Figure 2.4.: The Bullet Cluster 1E 0657-558 in the optical spectrum, the x-ray image of the gas clouds in red, and the mass distribution from gravitational lensing in blue [27].

Beyond this, DM consisting of particles that do not couple electromagnetically or strongly represents one of the more extensively studied hypotheses [23]. Electroweak or new types of interactions that couple weakly can not be fully excluded and provide a way to construct models that can be tested experimentally. These particles are called *Weakly Interacting Massive Particles* (WIMPs) and can explain most of the observations, including the relic density [28]. DM particles are usually assumed to be non, or only weakly self-interacting [29]. Options for particle-DM that are being discussed and searched for include the Lightest Supersymmetric Particle (LSP) [28], additional Higgs bosons [30], and Axions or axion like particles (ALPs) [31, 32].

2.2.2. Search Strategies

Dark matter is searched for using various experimental techniques given its unknown nature and possible interactions with SM particles. Experiments are generally differentiated by three categories, depending on the type of interaction that is probed between DM and SM particles, as shown in the symbolic Feynman diagram in Figure 2.5.

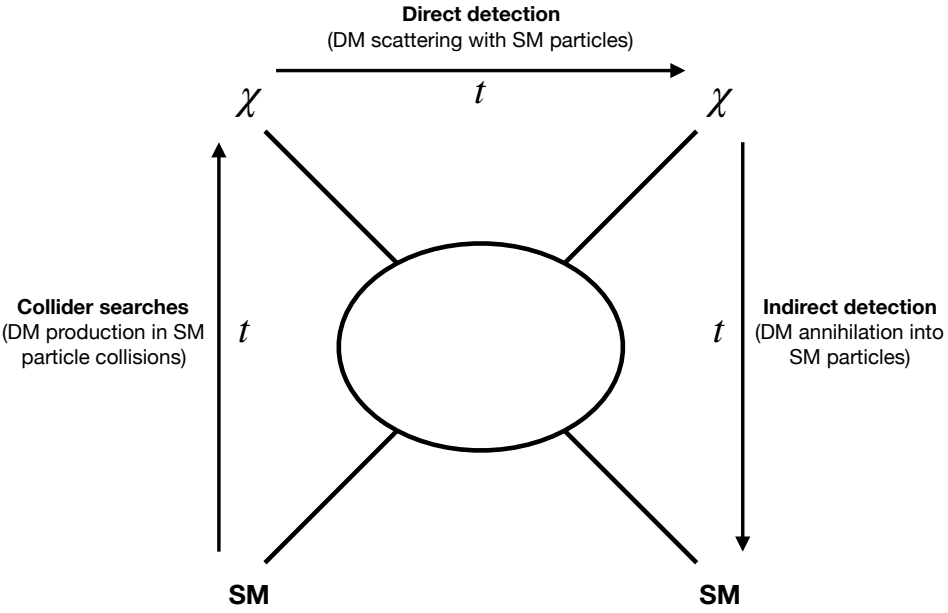

Figure 2.5.: The three main categories of experiments searching for DM particles χ and the generalised interaction that is probed, adapted from [33].

Direct Detection

Direct detection experiments [33] are designed to search for scattering of relic DM particles that are assumed to be concentrated in a halo around the galaxy with particles of the detector material. Large active volumes are often used to increase the interaction and thereby detection probability, since WIMP couplings to the SM are expected to be weak. The rate of expected events can be calculated [23]:

$$R \approx \sum_{i \in \text{ nuclei species}} N_i n_\chi \langle \sigma_{i\chi} \rangle \ , \tag{2.24}$$

with the number of target nuclei of species i in the detector N_i, the local WIMP density n_χ dependent on the WIMP energy density and mass, and the WIMP-nucleon scattering cross section averaged over the relative WIMP velocity $\langle \sigma_{i\chi} \rangle$. Expected are typically $\mathcal{O}(0.1)$ events per year and kg of detector material [34]. The interaction and resulting measured cross section can be further differentiated in spin-dependent and spin-independent [23]:

- *spin-dependent* (SD) interactions occur for axial-vector (or pseudo-scalar) couplings between nucleus and WIMP and the cross section is dependent on the total spin of the nucleus.

- *spin-independent* (SI) interactions occur for scalar (or vector) couplings and increase strongly with the target nucleus mass, hence the preferable use of active material with a high mass such as Xenon 131.

The sensitivity to the small nuclear recoil from possible scattering of DM with the atomic nuclei of the detector material has to be high, thus requiring low energy thresholds for detection and data acquisition. Furthermore, shielding from and vetoing of backgrounds such as radiation from cosmic and natural radioactive sources as well as the precise knowledge of remaining background spectra are important. Typical background minimising techniques include the localisation of the experiment in underground areas, further shields around the active detector material and the construction of detector parts as free as possible from radioactive isotopes.

A list of direct detection experiments with a brief description is given in the following. Spin-independent results from several direct detection experiments are shown in Figure 2.6.

- Cresst-III [35] is based beneath the Gran Sasso massif and uses cryogenic calorimeters based on scintillating crystals measuring phonons and light allowing for particle identification.

- The Large Underground Xenon (LUX) [36] experiment (USA), PandaX-II [37] (China), Xenon1T [38] (Gran Sasso) and DarkSide50 [39] (Gran Sasso) use time projection chambers with liquid Xenon (Argon for DarkSide50) and photo multiplier tubes to detect the scintillation light with dual-phase readout designs measuring prompt and secondary photons allowing to differentiate between signal types.

Indirect Detection

Indirect detection [23, 29, 41] experiments search for the annihilation of cosmic DM particles into pairs of SM particles by measuring the spectra of SM particles from astrophysical sources and comparing these to the expectations derived from known processes. Typical particle spectra that are measured are photon (pairs), electron-positron pairs, protons and neutrinos. These may be direct products of DM annihilation or from further decays of unstable SM particles that have been produced in the annihilation. These typically include pairs of W bosons, top or bottom quarks, and muons or taus.

The main difficulty is the modelling of the propagation of (charged) particles in the galaxy, leading to different predicted distributions of DM. Furthermore, spectra from known physics objects such as pulsars are often difficult to distinguish from possible DM signals [42]. Observable fluxes of particles from DM annihilation are expected primarily from locations with large DM density compared to the galaxy halo. These include the centre of the galaxy or dwarf spheroidal satellite galaxies of the milky way. The centre of the galaxy however is a source of substantial radiation, proving it impractical to point detectors directly at the centre. Several indirect detection experiments are listed in the following.

- The Fermi Large Area Telescope [43] on the International Space Station (ISS) measures gamma-rays.

- The Alpha Magnetic Spectrometer [44] is a general purpose particle detector on the ISS and measures positron, antiproton and gamma-ray fluxes.

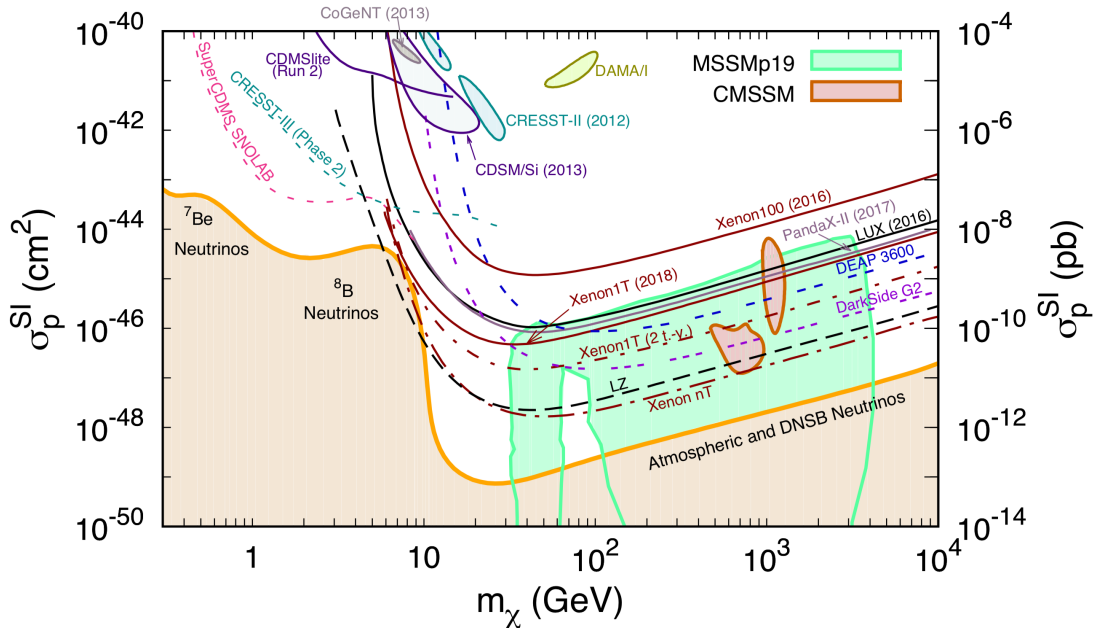

Figure 2.6.: Spin-independent (SI) exclusion limits on the WIMP-nucleon cross section and projections (dashed and dotted) from several direct detection experiments as a function of the WIMP mass [40]. The green and red shaded areas are preferred by supersymmetric models. The shaded areas on top of the plot correspond to the favoured regions for DM interpretations of anomalies. The yellow band corresponds to the neutrino bound.

- H.E.S.S. [45] is a ground-based array of Cherenkov telescopes searching for gamma-rays e.g. from the inner parts of the milky way.
- IceCube [46] employs a grid of optical sensors to detect Cherenkov radiation in the Antarctic ice, to search e.g. for highly energetic cosmic neutrinos.

Collider Searches

Collider searches can probe DM production in the annihilation of SM particles, quarks and gluons in the case of the LHC. Signatures can include a resonance in di-quark final states, or missing transverse momentum together with SM particles, further described in the following. Models that are used to describe the interaction between DM and the nucleus in direct detection experiments are often *Effective Field Theories* (EFTs) using contact interaction terms. The internal dynamics of the particle mediating the interaction is not considered (integrated out) in these EFTs, which is justified for the low energies probed compared to possible mediator scales. Hadron colliders such as the LHC however operate at much larger energy scales, thus requiring to consider the mediator as well [47]. Typical models include the DM candidate particles, and a new mediating particle connecting the SM with the dark sector. These so-called *Simplified Models* [48] include the masses of the new particles, as well as the couplings of the new mediator to the SM and DM particles as parameters. The relic density can guide the choice of parameter values, and existing

exclusion limits are taken into account [29]. A selection of models that are tested by the ATLAS collaboration is given in the following.

- Vector mediator models [49–51] predict a new spin-1 mediator particle similar to the vector bosons in the SM that couples to SM particles as well as to the dark sector. This can be done by adding a new $U'(1)$ group to the gauge sector giving rise to a Z' boson. Similarly, scalar or pseudoscalar mediators are considered as well.

- Two Higgs doublet models [30] include a second Higgs doublet that mixes with the SM Higgs sector and acts as mediator between the SM Higgs boson and DM candidates. *Two Higgs Doublet Models with Pseudoscalar Mediator* (2HDM+a) [52, 53] extend 2HDMs with an additional pseudoscalar a that interacts with fermionic DM particles. The coupling to the Higgs sector is established by mixing between the pseudoscalar and its counterpart in the 2HDM. This results in couplings between the Higgs boson and the pseudoscalar mediator on one side, and decays of this mediator to fermionic DM particles on the other. An advantage is the prediction of several experimentally accessible signatures depending on the chosen set of parameters.

- *Higgs Portal* models connect the dark sector directly to the SM with the Higgs boson as mediator and are introduced in the following Section 2.2.3.

The DM particles generally leave the detector without deposition of energy, similar to neutrinos due to the weak coupling to SM particles. Primarily, two techniques are employed to measure DM production at colliders:

1. In the case of a vector mediator model as described above, the mediator between DM and SM particles can be produced in the annihilation of initial state quarks. Hence, it is able to decay into pairs of quarks via the same coupling. This enables typical resonance searches to scan for possible new mediator particles in the mass spectra of final state systems consisting of two quarks.

2. The initial energy of the colliding partons in beam direction is not known precisely due to the varying momentum fraction. However, transverse to the beam direction the energy is vanishing in the initial, and hence in the final state. The imbalance of the transverse momenta of reconstructed objects $E_{\mathrm{T}}^{\mathrm{miss}}$, can thereby hint to particles which escaped detection. The search for a specific SM signature X together with $E_{\mathrm{T}}^{\mathrm{miss}}$ is a powerful probe for DM production at colliders. Typical signatures that ATLAS searches for in association with MET include a single quark or gluon [54], a Z boson decaying to pairs of electrons or muons [5], a photon [55] or a vector boson decaying hadronically [6].

A collection of exclusion limits on simplified DM models with a vector mediator from various ATLAS searches is shown in Figure 2.7.

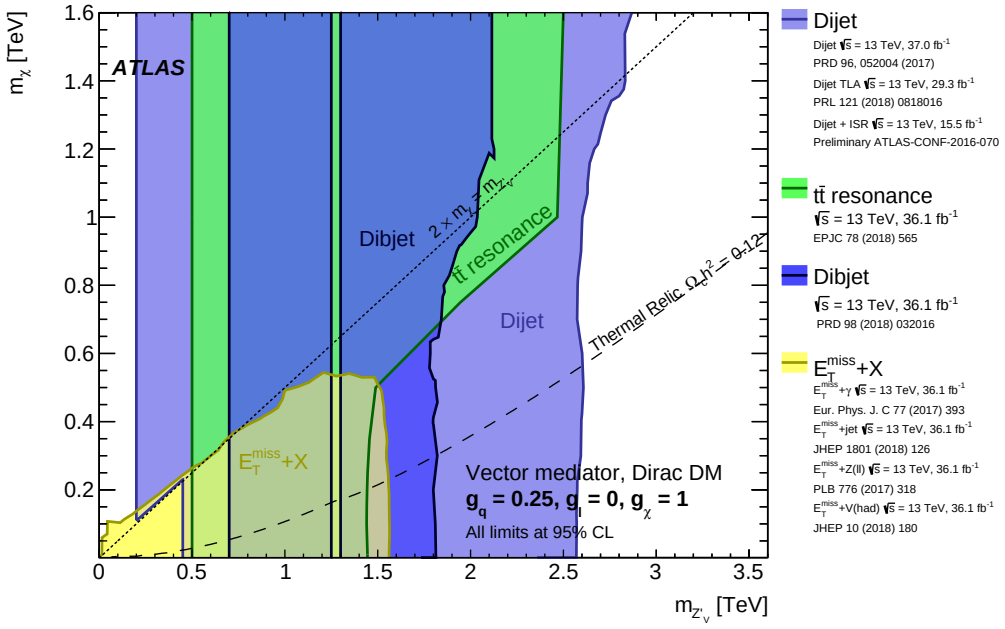

Figure 2.7.: A collection of exclusion limits in the DM particle mass m_χ and vector mediator mass $m_{Z'_V}$ plane from several searches conducted by the ATLAS collaboration [56].

2.2.3. Higgs Portal Models

Higgs Portal models [57–73] connect the dark sector to the SM directly through the Higgs boson by allowing the Higgs boson to decay invisibly to DM particles, if kinematically accessible. Such a Higgs portal framework can be used to compare the exclusion limits on $\mathcal{B}_{H\to\text{inv}}$ with exclusion limits from direct detection experiments on $\sigma_{\text{WIMP-nucleon}}$. Adopting formulas from [62], fermionic χ and scalar S WIMP candidates can be added by a coupling to the Higgs sector in an EFT approach:

$$\begin{aligned}\Delta\mathcal{L}_S &= -\frac{1}{2}m_S^2 S^2 - \frac{1}{4}\lambda_S S^4 - \frac{1}{4}\lambda_{hSS} H^\dagger H S^2\,,\\ \Delta\mathcal{L}_\chi &= -\frac{1}{2}m_\chi \bar{\chi}\chi - \frac{1}{4}\frac{\lambda_{h\chi\chi}}{\Lambda} H^\dagger H \bar{\chi}\chi\,,\end{aligned} \tag{2.25}$$

where m_S and m_χ are the scalar and fermionic WIMP masses, and λ_{hSS} and $\frac{\lambda_{h\chi\chi}}{\Lambda}$ describe the coupling strength of the SM Higgs to scalar and fermionic WIMPs. The EFT approach assumes that the scale of new physics is of the order of a few TeVor higher, well above the scale of the Higgs boson mass. A further $\mathbb{Z}_2$ symmetry is imposed under which SM and DM particles transform with reversed signs. This excludes an instability of the WIMP candidates due to terms proportional to $SH^\dagger H$. These would result, depending on the WIMP mass, in on- or off-shell decays via two Higgs bosons to lighter SM particles such as b quarks. The VEV of the scalar WIMP is set to zero in order to maintain the SM values for the couplings of the Higgs boson to the electroweak gauge bosons, defining their

masses. The physical WIMP masses arise after electroweak symmetry breaking:

$$\begin{aligned} M_S^2 &= m_S^2 + \frac{1}{2}\lambda_{hSS} v_0^2 \,, \\ M_\chi &= m_\chi + \frac{1}{2}\frac{\lambda_{h\chi\chi}}{\Lambda} v_0^2 \,. \end{aligned} \tag{2.26}$$

The invisible Higgs decay widths to scalar and fermionic WIMPs are then given by:

$$\begin{aligned} \Gamma^{inv}_{h\to SS} &= \frac{\lambda_{hSS}^2 v_0^2 \beta_S}{64\pi m_h} \,, \\ \Gamma^{inv}_{h\to\chi\chi} &= \frac{\lambda_{h\chi\chi}^2 v_0^2 m_h \beta_\chi^3}{32\pi\Lambda^2} \,, \end{aligned} \tag{2.27}$$

with a kinematic factor of $\beta_X = \sqrt{1-4(M_X^2/m_h^2)}$ and the effective couplings of the Higgs boson to the scalar λ_{hSS}^2 and fermionic $\lambda_{h\chi\chi}^2/\Lambda^2$ WIMP candidates.

The WIMP-nucleon cross section as probed by direct detection experiments can be computed by elastic scattering through exchange of the Higgs boson. The resulting cross section is spin-independent due to the scalar Higgs boson mediator:

$$\begin{aligned} \sigma^{\mathrm{SI}}_{S-N} &= \frac{\lambda_{hSS}^2}{16\pi m_h^4}\frac{m_N^4 f_N^2}{(M_S+m_N)^2} \,, \\ \sigma^{\mathrm{SI}}_{\chi-N} &= \frac{\lambda_{h\chi\chi}^2}{4\pi\Lambda^2 m_h^4}\frac{m_N^4 M_\chi^2 f_N^2}{(M_\chi+m_N)^2} \,, \end{aligned} \tag{2.28}$$

with m_N as the mass of the nucleon. The additional term f_N is the form-factor describing the interaction between the Higgs boson and a nucleon which can be obtained from lattice calculations. The value that is used for the comparison shown in this Thesis is given by $f_N = 0.308 \pm 0.018$ [74]. The invisible branching fraction can thus be translated into $\sigma_{\text{WIMP-}N}$ via the effective coupling to the WIMP candidate. This translation assumes that all invisible decays of the Higgs boson are to the WIMP candidates. The addition of other phenomena leading to invisible decays would strengthen the exclusion limit on $\sigma_{\text{WIMP-}N}$. A Higgs portal model introduced as described does not significantly alter the production mechanisms or cross sections for the Higgs boson through interactions of SM particles at a collider. The translation of exclusion limits on $\mathcal{B}_{H\to\text{inv}}$ obtained from direct searches assuming SM Higgs boson production, into exclusion limits on $\sigma_{\text{WIMP}-N}$ employing the framework of Higgs portal models is therefore justified.

3. The LHC and the ATLAS Experiment

This Chapter describes the experimental framework of the searches presented and statistically combined in this Thesis. The Large Hadron Collider accelerator complex is briefly introduced in Section 3.1. The ATLAS detector used to measure the products of proton-proton collisions at the LHC is described in Section 3.2.

3.1. The Large Hadron Collider

The Large Hadron Collider (LHC) [75] is located at the European Organization for Nuclear Research (CERN), in the tunnel of the former electron - positron collider LEP, between 45 m and 170 m below the surface. It is the most powerful particle accelerator built to date and is used to accelerate, and bring into collision beams of protons, or heavy ions such as lead. Superconducting Nb-Ti magnetic field coils are cooled to 1.9 K using supra-fluid helium. A magnetic field strength of up to 8.33 T is achieved, which is required to hold the accelerated particles on their circular path. The accelerator complex at CERN features a chain of pre-accelerators employed before injection into the LHC, see Figure 3.1. The linear accelerator LINAC2 accelerates protons obtained from hydrogen atoms. In addition, three circular colliders are passed successively: the BOOSTER, the Proton Synchrotron (PS) and the Super Proton Synchrotron (SPS). The protons acquire an energy of 450 GeV before reaching the LHC. The proton beams are injected into the LHC in up to 2808 bunches of roughly 10^{11} protons spaced 25 ns apart. The bunch structure is an effect of the radio frequency (RF) cavities used as accelerating structures. The protons are further accelerated in the LHC by RF cavities with a field strength of 2 MV/m to currently up to 6.5 TeV per beam. Quadrupole magnets focus and squeeze the beams, thereby increasing the interaction rate.

Two important parameters characterize the performance of a particle collider, the center-of-mass energy $\sqrt{s}$ and the instantaneous luminosity $\mathcal{L}$. The center-of-mass energy describes the maximum energy that can be transferred in an interaction, which is $\sqrt{s} = 13\,\text{TeV}$ for a beam energy of 6.5 TeV. The instantaneous luminosity is connected to the interaction rate, and is given by the rotation frequency of the beams in the tunnel f, the number of particles per colliding bunch $N_{1,2}$ and the geometry of the beam at the interaction point A:

$$\mathcal{L} = \frac{N_1 N_2 f}{A}\,. \tag{3.1}$$

The instantaneous luminosity achieved in operation ranges around $10^{34}\ \text{cm}^{-2}\,\text{s}^{-1}$. The integration over a period of data-taking time yields a measure that is directly propor-

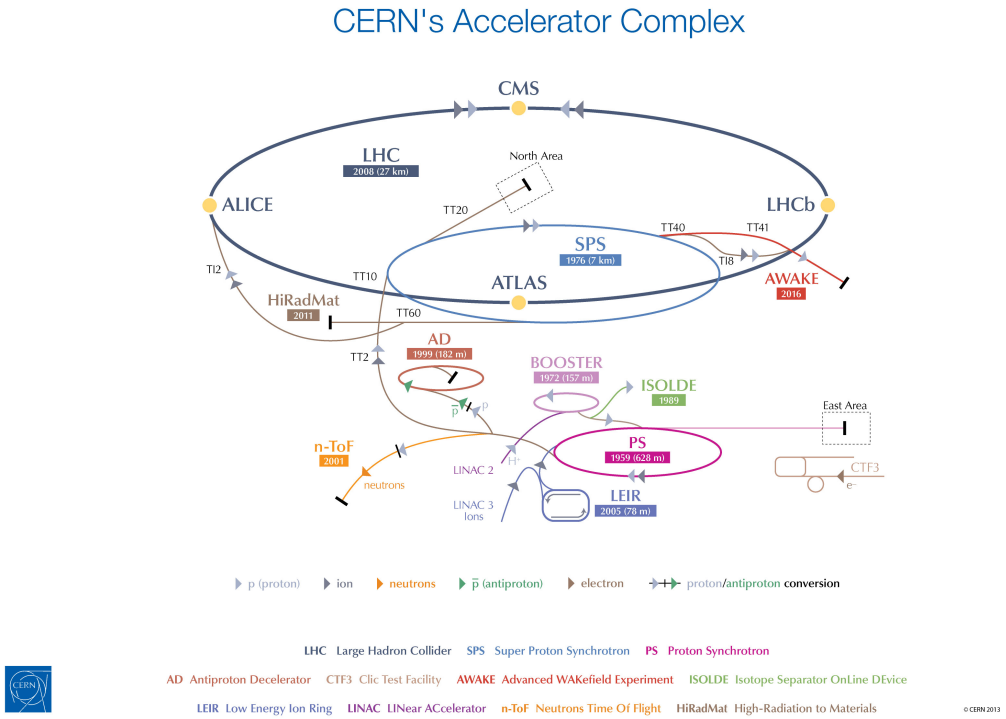

Figure 3.1.: The CERN accelerator complex [76].

tional to number of expected events for a process with cross section σ as described in Section 2.1.3:

$$R = \frac{\mathrm{d}N}{\mathrm{d}t} = \mathcal{L}\sigma\,, \qquad N = \mathcal{L}_{\mathrm{int}}\sigma\,. \tag{3.2}$$

The expected number of simultaneous proton-proton interactions in a single bunch-crossing is $\langle\mu\rangle = 33.7$ averaged over the LHC Run 2, and increases with the instantaneous luminosity. The mostly low energetic additional *pile-up* interactions next to the studied hard-scattering represent a challenge to the triggering and analysis of events. The luminosity delivered by the LHC and recorded by the ATLAS experiment, together with the profile of interactions per bunch-crossing in different data-taking periods is shown in Figure 3.2.

There are four large scale experiments located around the LHC, each at a different interaction point in the 26.7 km long tunnel, see Figure 3.1.

- ALICE (A Large Ion Collider Experiment) [78] was built to study the collisions of heavy ions such as lead at high energies. Predictions of the strong interaction can be probed in these collisions.

- ATLAS [79] is a multi-purpose experiment built for a variety of searches for new physics and precise measurements of SM predictions, including the Higgs boson and Super Symmetric (SUSY) extensions of the SM.

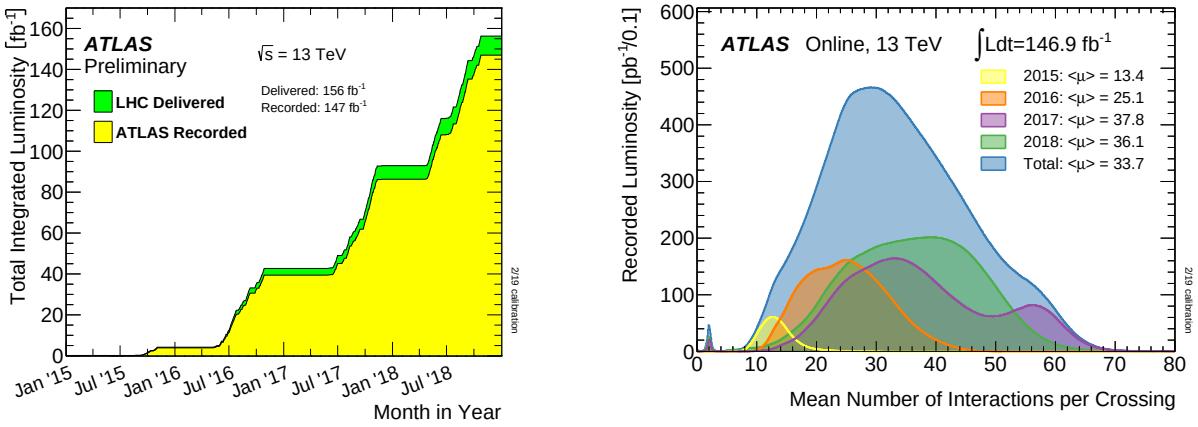

(a) **(b)**

Figure 3.2.: The integrated luminosity as delivered by the LHC (green) and recorded by the ATLAS experiment (yellow) for Run 2 **(a)** and the profile of interactions per bunch-crossing $\langle\mu\rangle$ **(b)** [77].

- CMS (Compact Muon Solenoid) [80] is a multi-purpose similar to ATLAS in the physics programme based on different detector technologies.
- The LHCb (Large Hadron Collider beauty) [81] experiment is a forward spectrometer, primarily designed to precisely measure the production and rare decays of hadrons including b quarks. This enables the study of CP-violation and matter-antimatter asymmetry.

3.2. The ATLAS Experiment

The ATLAS experiment [79] is one of the four large experiments at the LHC, designed for a versatile physics programme focussing on proton-proton collisions. It is a classically structured collider experiment with layers of different subdetectors around the interaction point (IP). The subsystems are chosen to allow for the reconstruction of as many particle types as possible. The inner detector (ID) is formed by a tracking system, see Section 3.2.1. The tracker is surrounded by the calorimeter consisting of an electromagnetic (EMcal) and a hadronic (Hcal) layer, introduced in Section 3.2.2. The outer most layers are occupied by the muon system, described in Section 3.2.3. The trigger system combines the information of different subsystems in order decide whether an event is recorded, and is detailed in Section 3.2.4. An overview of the ATLAS detector is given in Figure 3.3.

ATLAS uses a right-handed coordinate system with its origin at the interaction point. The positive z-axis is defined in beam direction while the transverse plain is described by the y-axis pointing upwards and the x-axis aiming to the center of the LHC ring. The azimuthal angle ϕ is defined from the positive x-axis around the beam line, and the polar angle θ describes the displacement from the z-axis. The rapidity is given by $y = \text{atanh}\,(\frac{p_z}{E})$ and features the advantage that rapidity differences are invariant under Lorentz-boosts in beam direction. Commonly used is the pseudorapidity $\eta = \text{atanh}\,(\frac{p_z}{|p|}) = -\ln[\tan\frac{\theta}{2}]$,

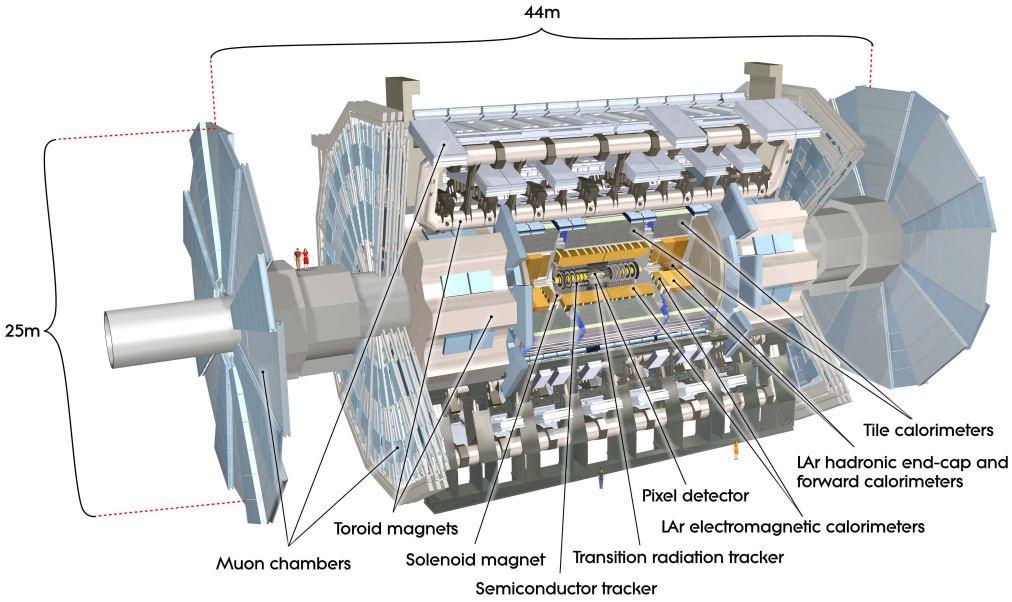

Figure 3.3.: Cut-away view of the ATLAS detector [79].

which is equivalent to the rapidity in the limit $v \to c$. Angular distances are measured in units of $\Delta R = \sqrt{\Delta\eta^2 + \Delta\phi^2}$. Particle momenta are measured in the plane transverse to the beam direction using the p_{T} observable since the incident momenta of the colliding particles in the z-direction are unknown.

3.2.1. Inner Detector

The inner part of the detector is used to measure the trajectories of charged particles and shown in Figure 3.4. A highly radiation hard set-up is required to maintain long-time stability due to the tremendous amount of scattering processes. However, there should be as less as possible material in front of the calorimeter to minimize previous energy loss. Photons can further interact with the ID material and convert into electron positron pairs.

Charged particles leave tracks due to ionisation of the detector material. Their trajectories are bent by the Lorentz force in the 2 T field of the solenoid magnet located between the ID and the EMcal. The resulting curvature provides information about the transverse momenta p_{T}, and the sign of the charge of the traversing particles. Energy depositions in the calorimeter can be linked to vertices, and by precisely resolving the locations of primary and secondary vertices it is possible to exploit the comparably long lifetime of heavier particles such as b-hadrons or tau leptons to tag those.

The tracking part is 6.2 m long, 2.1 m high, and is divided into three different regions, see Figure 3.4. A high granularity silicon pixel detector is used in the inner layers around the beryllium beam pipe, with a new layer installed after Run 1. Silicon Strip Detectors are installed further apart of the interaction point (IP). The outermost part of the ID is covered by the Transition Radiation Tracker, which is instrumented with gaseous straw tubes. The relative transverse momentum resolution is given by $\frac{\sigma_{p_{\mathrm{T}}}}{p_{\mathrm{T}}} = (4.83 \pm 0.16) \times$

$10^{-4} \times p_{\mathrm{T}}$ [GeV]. The vertex reconstruction resolution improves with the number of tracks and ranges between 20 µm and 160 µm longitudinally, and between 40 µm and 340 µm transversally. The different subsystems of the ID are detailed in the following.

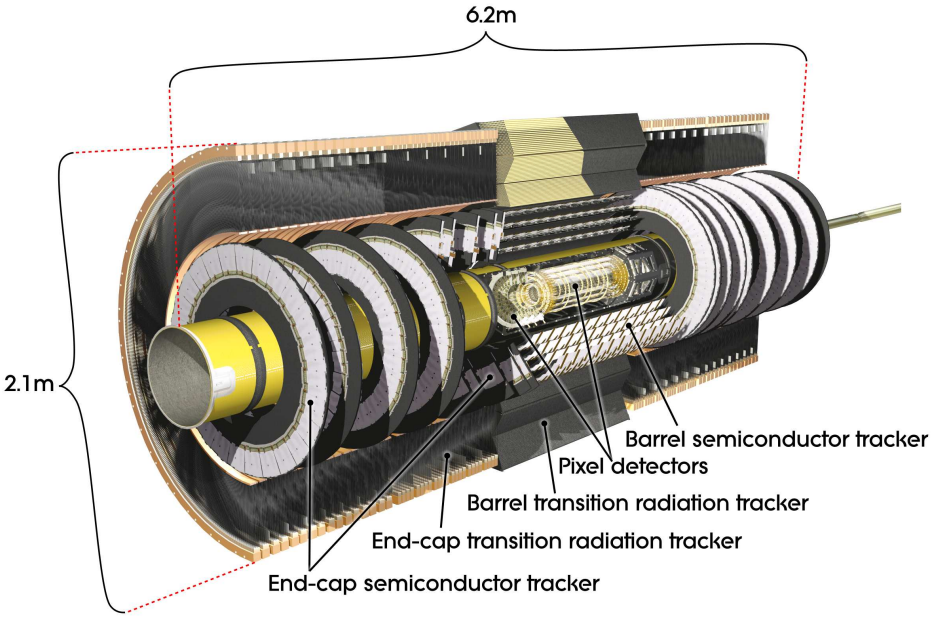

Figure 3.4.: The inner detector with its subsystems [79].

Silicon Pixeldetector

A highly accurate measurement of discrete space-points in the Pixel Detector is provided by 80.4 million single pixels, sized 50×400 µm^2 for 90% and 50×600 µm^2 for the remaining 10% of the pixels in the front-end electronic regions, grouped into 1744 sensor modules. The design of three barrel layers and two end-caps with three disc layers each, covers a region up to $|\eta| < 2.5$. The resolution of about 10 µm in R-ϕ and 115 µm in z (barrel layers) and 10 µm in R-ϕ and 115 µm in R (disks) guarantees an accurate vertex reconstruction. The 250 µm thick silicon sensor modules are using oxygenated n-type wafers with n-type readout which ensures radiation tolerance to charged hadrons. The read out is connected directly to the sensors which are operated at temperatures below 0 °C to reduce thermal noise that increases due to irradiation.

Insertable B-Layer

The Insertable B-Layer (IBL) [82] was integrated into the ID during the shut down after Run 1, in conjunction with a smaller beam pipe. It is located between the new beam pipe and the first layer of the Pixel Detector. The addition of a fourth space point mainly improves b-tagging, and counters degradation effects due to the high radiation environment in the course of time. The layer consists of 26880 silicon pixels arranged in 80 columns and 336 rows with a size of 50×250 µm, covering a range up to $|\eta| < 3.0$.

Silicon Strip Detector

The overall design of the Silicon Strip Detector (SCT) is similar to the pixel detector with four cylindrical layers and nine disk layers per end-cap with a coverage of $|\eta| < 2.5$. There are 4088 modules, split into 2112 barrel and 1976 end-cap modules. Each module is 6.4 cm × 80 µm in size, and composed of two silicon strip sides glued back-to-back, producing stereo pairs of hits. One half of the barrel (end-cap) SCT is aligned longitudinally to the beam axis (in R), the other half is tilted by an angle of 40 µrad to improve the resolution. The resolution of the SCT with 17 µm in R-ϕ and 580 µm in z for the barrel, respectively R for disks, is well suited for the primary task of transverse momentum determination. The technology used for the 285 µm thick sensors is a single-sided p-in-n one with AC-coupled readout strips.

Transition Radiation Tracker

The Transition Radiation Tracker (TRT) uses polyimide drift (straw) tubes to detect transition radiation produced by charged particles passing through inhomogeneous media. The volume between the tubes if filled with polypropylene. The tubes feature a diameter of 4 mm, and a length of 144 cm in the barrel region, and 37 cm in the end-cap region. They are filled with a mixture containing 70 % Xe, 27 % CO_2 and 3 % O_2 at a pressure of about $5 - 10$ mbar. A gold plated central tungsten wire serves as anode. The tubes are arranged in parallel to the beam pipe, and segmented into 32 read-out ϕ-sectors resulting in a reduced coverage of $|\eta| < 2.0$ and no measurement in z-direction. On average, 36 hits per track are measured by the TRT, which are used for pattern recognition. Two different thresholds are used to distinguish between tracking signals and low energetic transition radiation photons as they produce a much larger amplitude. The resolution of the TRT is given by 130 µm in R-ϕ.

3.2.2. Calorimetry

The ATLAS calorimeters stop and measure the energy and direction of most of the particles exiting the tracker, the systems are shown in Figure 3.5. Neutrinos and muons generally pass through the calorimeters. The particles entering the calorimeter cause showers of secondary particles, which are stopped inside the detector to precisely measure the energy. The electromagnetic layer is optimised for the measurement of showers generated by photons and electrons. Hadronic showers usually are much larger and are stopped in the proceeding hadronic layer. The measurement of hadronic showers used information from both layers. All calorimeters are of sampling type, alternating an absorbing material with an active material. The showers develop mainly in the absorbers with high Z. The thereby produced secondary particles generate signals in the active material proportional to the energy of the incident particle by ionization or excitation. Electromagnetic showers are caused by electrons and photons which interact with the detector material at higher energies via bremsstrahlung and pair-production. This generates a cascade of secondary particles, while the energy per particle is successively decreasing. A passive material with high Z amplifies this process. At lower energies, these particles interact primarily via

the photoeffect and ionisation, measured in the active material. Highly energetic hadrons are decelerated by inelastic nuclear scattering (spallation). They are stopped due to the energy transfer of ionisation, or are absorbed by a nucleus, when the energy decreased sufficiently. The spallation yields cascades of secondary particles such as neutrons, resulting in a hadronic shower, described by the nuclear absorption length λ. Hadrons will start showering in the electromagnetic layer but pass through and are stopped in the larger hadronic layer. This reflects the slower interaction rate of nuclear, compared to electromagnetic interactions. The energy resolution of a measured hadronic shower is limited by several effects, including: nuclei can be excited to longer lived states, different responses to the electromagnetic and hadronic parts of the shower, and the statistical distribution of pions which constitute the main part of the shower. The π^0 decays primarily to two photons interacting electromagnetically, the charged pions can decay weakly to a neutrino and muon, which escape detection. The electromagnetic and hadronic layers are detailed in the following.

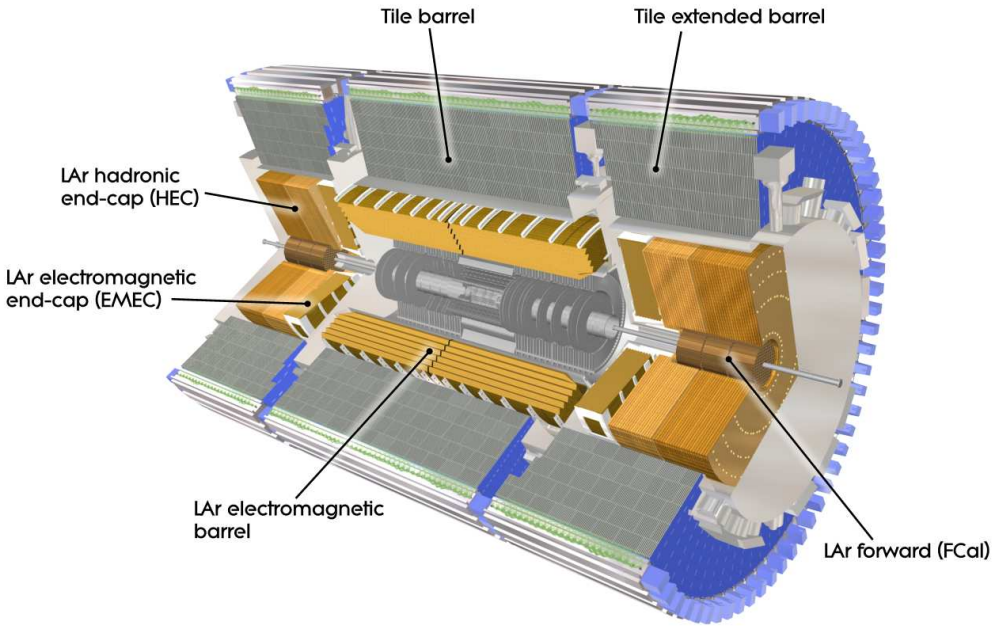

Figure 3.5.: The ATLAS calorimeter with its subsystems [79].

Electromagnetic Calorimeter

The electromagnetic layer (EMCal) is thick enough (> 22 radiation lengths) to stop most electromagnetic showers and covers a region up to $\eta < 3.2$. It is split into a barrel part ($|\eta| < 1.475$) and two wheels per end-cap, which cover $1.375 < |\eta| < 2.5$ and $2.5 < |\eta| < 3.2$. The transition region between barrel and end-cap at around $|\eta| = 1.4$ features an increased amount of non-active material (around 11 radiation lengths), which decreases the accuracy of measurements. The absorbing medium is accordion-shaped lead, with liquid-argon filled between the layers acting as active detection material. The

geometry is used to improve the acceptance in ϕ. Copper electrodes cover the lead surface and collect the ionisation signal generated by the shower components in the liquid argon. The segmentation is given by 0.025×0.025 in $\eta \times \phi$ within the middle layer, where most of the energy is deposited. This region is instrumented with a fine readout, in contrast to the remaining parts featuring a coarser segmentation. In $|\eta|$, the spatial resolution is best for values smaller 2.5. The energy resolution in the electromagnetic calorimeter is given by $\frac{\sigma_E}{E\,[\mathrm{GeV}]} = \frac{10\%}{\sqrt{E}\,[\mathrm{GeV}]} \oplus 0.7\%$

Hadronic Calorimeter

The Hadronic layer (HCal) is split into a barrel part (coverage of $|\eta| < 1.7$), end-caps ($1.5 < |\eta| < 3.2$) and a Forward Calorimeter (FCal) which covers $3.1 < |\eta| < 4.9$. They are equipped with different absorbing and active materials. Liquid-argon is employed in the end-caps and the FCal, whereas the barrel is constructed from scintillating tiles. Steel is used as absorbing material for the barrel, copper for the end-caps and the FCal part closer to the IP, and tungsten for the remaining FCal. The probability for a punch-through of a hadronic shower is very small due to the thickness of $7.4\,\lambda$ for the barrel, and $9.7\,\lambda$ for EMCal plus HCal. The numbers do not take into account support structures and instrumentation such as cables, which further increase the effective value. The energy resolution of the hadronic calorimeter in the barrel region is given by $\frac{\sigma_E}{E\,[\mathrm{GeV}]} = \frac{50\%}{\sqrt{E}\,[\mathrm{GeV}]} \oplus 3\%$, and in the end-caps by $\frac{\sigma_E}{E\,[\mathrm{GeV}]} = \frac{100\%}{\sqrt{E}\,[\mathrm{GeV}]} \oplus 10\%$.

3.2.3. Muon Spectrometer

Muons pass the calorimeters in the majority of cases due to their minimal ionizing nature. The larger mass compared to electrons reduces effects of Bremsstrahlung, and interactions with hadrons are reduced since muons do not couple strongly. The Muon Spectrometer (MS) hence covers the largest and outermost part of the ATLAS detector, as shown in Figure 3.6. Muon trajectories are bend due to the magnetic fields generated by eight large toroidal coils in the barrel region, and two smaller sets of four end-cap toroidal coils. The barrel section extends up to $|\eta| < 1.4$ and the end-caps cover a range of $1.6 < |\eta| < 2.7$. The magnetic field reaches 0.5 T in the barrel region, and 1 T in the end-caps. Both magnetic fields are superposed in the region $1.4 < |\eta| < 1.6$. In conjunction with different tracking systems, this allows for a stand-alone p_{T} measurement up to 3 TeV. The MS is used to measure the trajectories of muons, trigger the data acquisition, and to identify bunch-crossings as well as backgrounds due to cosmic rays. Four different subsystems are installed: the Monitored Drift Tube Chambers (MDTs) and Cathode Strip Chambers (CSCs) are employed for precise measurements of the trajectories, and Resistive-Plate Chambers (RPCs) and Thin-Gap Chambers (TGCs) are used for triggering and bunch-crossing identification. The combined MS yields a resolution of around 10% for a muon with $p_{\mathrm{T}} = 1\,\mathrm{TeV}$, which is further improved by matching tracks to the ID.

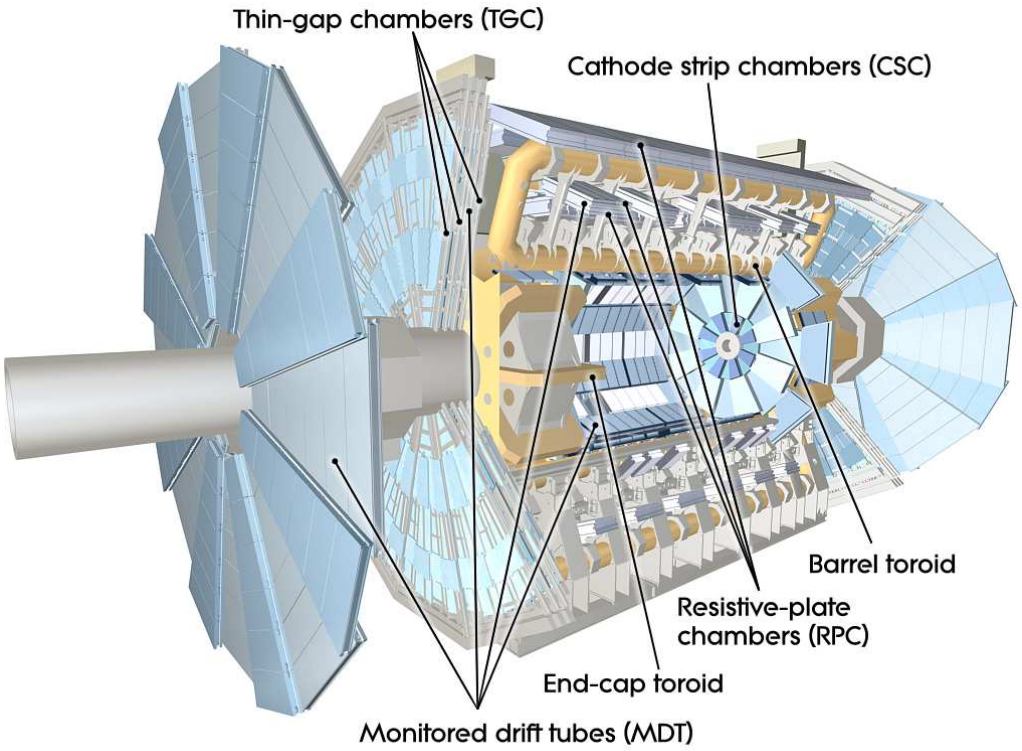

Figure 3.6.: Cut-away view of the muon system [79].

Precision Subsystems

The MDTs cover a range of $|\eta| < 2.7$ and consist of drift tubes perpendicular to the r-z plane, filled with 93% Argon and 7% CO_2 at a pressure of 3 bar. The central wires are constructed from an alloy of tungsten and rhenium. The resolution of the MDTs is given by 35 µm in r-z. CSCs are employed in the inner-most layer of the end-caps, corresponding to a range of $2.0 < |\eta| < 2.7$, instead of MDTs due to cope with the higher rates in this region. They are constructed as multi-wire proportional chambers filled with 80$ Argon and 20% CO_2. The information on the r-z coordinate is retrieved from cathode wires perpendicular to the anodes. The ϕ coordinate is similarly obtained from parallel cathode wires. The resolution of the CSCs is given by 40 µm in r-z and about 5 mm for ϕ.

Fast Timing Subsystems

The RPCs consist of two highly resistive electrodes separated by 2 mm filled with a gas mixture of (fluorinated)hydrocarbon and SF_6. High-voltage is applied to the plates to achieve an electric field of $4.9\,\mathrm{kV\,mm^{-1}}$ between these. This results in a high time resolution of around 1.5 ns suitable for triggering and bunch-crossing identification in the RPC region of $|\eta| < 1.05$. The multi-wire proportional TGCs are installed in the $1.05 < |\eta| < 2.4$ region. The anode wires are placed in a chamber with conducting walls serving as cathode, filled with a mixture of CO_2 and n-pentane. A high time resolution

of about 4 ns is ensured by a quasi-saturated operation. Both the RPCs and TGCs also provide supplementary hit measurements in ϕ direction not resolved by the MDTs.

3.2.4. Trigger

The Trigger system aims to reduce the overwhelming amount of data produced by the ATLAS detector at an bunch-crossing rate of 40 MHz and an event size of order 1 MB to a degree that is feasible for storage technologies. This is done with a system composed of a hardware and a software trigger by selecting events with a high momentum transfer or other characteristics that increase their relevance for physics studies. Trigger items that are selected by the two staged system can be e.g. a single lepton or a jet with a certain p_{T} or energy threshold. Some of these items would be accepted with a rate that exceeds the trigger bandwidth limited by the reconstruction and storage. This can be the case for items with a low threshold. These may be interesting for certain measurements or searches. A prescale of value S is applied to those items in order for the trigger system to accept only one event out of S fulfilling the requirements on this item.

The first part of the trigger is the Level 1 Trigger (L1) composed of custom-hardware FPGAs, which identifies certain Regions-of-Interest (RoIs) and selects events using detector information with reduced granularity in $\eta \times \phi$. The L1 trigger reduces the event rate from 40 MHz to about 100 kHz. Events are selected by L1 in view of signatures such as the scalar sum of transverse energy, electromagnetic objects, muons, jets or $E_{\mathrm{T}}^{\mathrm{miss}}$ exceeding certain thresholds. It receives information from the calorimeters as well as from the muon systems. Tracks from the finely segmented ID can not be reconstructed at L1 due to time constraints. The second part is the High Level Trigger (HLT), based on software run on commercially available CPUs. It has access to the full detector information including reconstructed ID tracks, mostly in the ROIs provided by L1 to reduce computation time. In the HLT, events are reconstructed step by step, running decisively algorithms as soon as the event building progressed sufficiently. The HLT reduces the event rate from 100 kHz to around 1 kHz.

Events that pass L1 and the HLT are then stored permanently and reconstructed offline at the ATLAS Tier-0 site with information from all detector subsystems. Most analyses use events of the physics stream that were triggered by the various physics items defined in the trigger menu. Several other data streams exit for special purposes. This includes a calibration stream with events e.g. from empty bunch-crossings, and an express stream of events which are reconstructed with high priority and used for the on-line monitoring of the data quality.

4. Methodology

This Chapter describes the methodologies used throughout this Thesis. The statistical models behind the description and interpretation of the data as well as the setting of exclusion limits are introduced, together with a description of the technical framework employed for the combination, in Section 4.1. The terminology and the reconstruction techniques for the most important objects used by the searches: electrons, muons, jets and the missing transverse momentum $E_{\mathrm{T}}^{\mathrm{miss}}$ are briefly introduced in Section 4.2.

4.1. Statistical Analysis

The statistical interpretation of the data relies on likelihoods models, introduced in 4.1.1, used to describe the probability of the observed distributions given specific hypotheses on parameters and incorporating the effects of sources of systematic uncertainty. The modified frequentists CL_S technique detailed in 4.1.2, is employed to derive exclusion limits on a given model parameter from observed data, as well as their expectations given the experimental sensitivity to the hypothesis. The statistical and technical combination procedure is described in 4.1.3.

4.1.1. Likelihood Model

The statistical model used for the description of the data is based on *likelihood functions* $\mathcal{L}$. Part of the notation used in the discussion of the likelihood model and limit setting is adapted from [83]. A single measurement of the value x is described by a *probability density function* (pdf) $f(x \,|\, \boldsymbol{\theta})$, with parameters $\boldsymbol{\theta}$ characterising the shape of the pdf. The likelihood function for the measurement of n independent values $\boldsymbol{x}$ is obtained by the product of the probabilities for each measured value of $x_i \in \boldsymbol{x}$:

$$\mathcal{L}(\boldsymbol{x} \,|\, \boldsymbol{\theta}) = \prod_{i=1}^{n} f(x_i \,|\, \boldsymbol{\theta})\,. \tag{4.1}$$

The data are commonly analysed in histograms, counting events binned in specific observables such as $E_{\mathrm{T}}^{\mathrm{miss}}$. The statistical interpretation makes use of the predictions for a background hypothesis, typically the SM, and a signal hypothesis such as invisible decays of the Higgs boson. The expected number of events in one bin n_i is given by the number of expected background events, b_i and signal events, s_i in this bin:

$$E[n_i] = \mu s_i + b_i\,, \tag{4.2}$$

where μ is the signal strength, scaling the signal hypothesis such that it can be quoted as measurement, or exclusion limits can be set upon. It is referred to as parameter of

interest in the statistical interpretation. The s_i and b_i are obtained from the corresponding signal and background pdfs, integrated over the boundaries of the bin. This yields the probability for an event to be found in bin i when scaled by the total number of expected signal or background events:

$$\begin{aligned} s_i &= s_{\text{total}} \int_{\text{bin } i} f_s(x \,|\, \theta_s)\, \mathrm{d}x \,, \\ b_i &= b_{\text{total}} \int_{\text{bin } i} f_b(x \,|\, \theta_b)\, \mathrm{d}x \,. \end{aligned} \tag{4.3}$$

While b_{total} is usually a parameter of the statistical model, s_{total} is fixed to the nominal signal hypothesis. A common choice is the cross section of a process under study relative to the SM prediction, corresponding to $\mu = 1$ for the background-only case. In the searches combined here, the common parameter of interest is the invisible branching fraction of the Higgs boson, $\mathcal{B}_{H\to\text{inv}}$, whose value is zero for the background-only hypothesis (SM prediction $\approx 10^{-3}$) and one for a nominal signal hypothesis of 100% of Higgs bosons decaying invisibly. The most compatible value for $\mathcal{B}_{H\to\text{inv}}$ measured in these searches can reach negative values due to statistical fluctuations in the background distributions and comparably small signal expectations.

At particle colliders such a counting experiment is repeated with high statistics and the distribution of events in a single bin is described by a Poisson distribution with expected number of events $E[n_i]$. The likelihood function for the parameter of interest describes the compatibility of the signal hypothesis with the observed data. It is computed by the product of Poisson terms for all bins with observed numbers of events n_i:

$$\mathcal{L}(\mu \,|\, \boldsymbol{\theta}) = \prod_{i=1}^{N} \frac{(\mu s_i + b_i)^{n_i}}{n_i\,!} e^{-(\mu s_i + b_i)} \,. \tag{4.4}$$

Search Regions

Information can be added from distributions in other observables, from different search regions characterised by selection criteria, or even from completely different searches given that these are statistically independent.

A *signal region* (SR) is a region of the phase space probed by a search where the signal model predicts a significant excess of events over the background prediction. Kinematic cuts are placed on the events to obtain a signal significance as optimal as possible [84]. Background *control regions* (CRs) are constructed to yield a large amount of background events while still retaining kinematic similarity to the SR. This can be achieved e.g. by inverting kinematic cuts that are employed in the SR to lower the contamination of the specific background. The CRs are used to infer information on characteristics of the background distributions in the SR. Typical parameters are the normalisation in form of b_{total}, or information on the background shape. This can be done by so-called *transfer factors* that are estimated in the CRs and and modify the background prediction in the SR. Adding the bins j of a CR, with the expectation value u_j of the yield in bin j, and

the observed number of events in this bin m_j into the likelihood model yields:

$$\mathcal{L}(\mu \,|\, \boldsymbol{\theta}) = \prod_{i=1}^{N} \frac{(\mu s_i + b_i)^{n_i}}{n_i\,!} e^{-(\mu s_i + b_i)} \prod_{j=1}^{M} \frac{u_j^{m_j}}{m_j\,!} e^{-u_j}\,, \tag{4.5}$$

where the background predictions in the SR b_i depend on the observed events in the CR m_j. Further regions that might be added to the statistical model are *validation regions* (VRs) in a phase space between CR and SR where the predictions from the CRs for background distributions in the SR are validated.

Systematic Uncertainties and Profiling

Sources of systematic uncertainty affect the predictions for different processes. They are implemented via *nuisance parameters* (NPs), each usually corresponding to a specific source of systematic uncertainty. Nuisance parameters represent most of the parameters $\boldsymbol{\theta}$ describing the signal and background predictions. Examples of systematic uncertainties are the value of the integrated luminosity which has an associated uncertainty, residual effects of calibrations, and uncertainties on theory predictions.

The size of a systematic uncertainty is commonly estimated via auxiliary measurements or theory calculations yielding information on the mean value θ_i^0 and width σ_i of the parameter θ_i. The corresponding nuisance parameter in the likelihood model has its nominal value at θ_i^0. The nuisance parameter is typically constrained by a Gaussian, log-normal, or gamma distribution $f(\theta_i \,|\, \theta_i^0, \sigma_i)$ with the width σ_i. The prior can take a flat form in some cases such as certain theory uncertainties. The effect of nuisance parameters on the modelling is normalised to yield $\theta_i^0 = 0$ and $\sigma_i = 1$, in order to facilitate numeric computation. With these constraining priors for the systematic uncertainties in the form of nuisance parameters, and explicitly showing the dependence on them, the likelihood function reads:

$$\mathcal{L}(\mu \,|\, \boldsymbol{\theta}) = \prod_{i=1}^{N} \frac{(\mu s_i(\boldsymbol{\theta}) + b_i(\boldsymbol{\theta}))^{n_i}}{n_i\,!} e^{-(\mu s_i((\boldsymbol{\theta})) + b_i(\boldsymbol{\theta}))} \prod_{j=1}^{M} \frac{u_j(\boldsymbol{\theta})^{m_j}}{m_j\,!} e^{-u_j(\boldsymbol{\theta})} \prod_{\theta_k \in \boldsymbol{\theta}} f(\theta_k \,|\, \theta_k^0, \sigma_k). \tag{4.6}$$

The maximisation of the likelihood function, or equivalently the numerically more accessible minimisation of $-2 \ln \mathcal{L}(\mu \,|\, \boldsymbol{\theta})$ with respect to the parameter of interest, yields the best-fit or most probable value $\hat{\mu}$. This value characterises the hypothesis for the underlying model resulting in the largest agreement with the given observed data. The nuisance parameters are simultaneously varying within their priors in the minimisation process. This modifies the signal and background predictions within the systematic uncertainty for a more accurate modelling of the data. Thereby, an excess or phase space differences between the auxiliary measurement and the search regions may be compensated. The resulting most-probable values for the nuisance parameters are denoted by $\hat{\boldsymbol{\theta}}$:

$$\max \mathcal{L}(\mu \,|\, \boldsymbol{\theta}) \equiv \mathcal{L}(\hat{\mu} \,|\, \hat{\boldsymbol{\theta}})\,. \tag{4.7}$$

Large deviations from the nominal values penalise the likelihood due to the decreasing nature of the prior distributions off the mean θ_i^0. A parameter is referred to as *profiled* if

it varies in the minimisation process to increase the agreement. Its value resulting from the minimisation of $-2\ln\mathcal{L}(\mu\,|\,\boldsymbol{\theta})$ is referred to as *profiled value* or *pull*. The profiling of the nuisance parameters and μ enables the search to measure the parameter of interest and the effect of systematic uncertainties in a single procedure.

The likelihood model may be sensitive to a specific nuisance parameter resulting in a stronger constraint on it compared to the input uncertainty σ_i. This is reflected by the *post-fit* uncertainty on the profiled nuisance parameter to be smaller than the *pre-fit* uncertainty σ_i. Here, a search is sensitive enough to a specific source of systematic uncertainty in the probed phase space to use this stronger constraint respectively smaller uncertainty in the statistical interpretation of the data. Analogously, CRs can provide information not only on background distributions, but can also constrain specific uncertainties in the SR. The post-fit uncertainty is typically computed either by the second derivative at the minimum (HESSE algorithm [85]), or by the interval in which $-2\ln\mathcal{L}(\mu\,|\,\boldsymbol{\theta})$ as a function of the specific nuisance parameter rises by 0.5 with respect to the most-probable value at the minimum (MINOS algorithm [85]).

4.1.2. Setting of Confidence Limits

A suitable test statistic is needed to differentiate between the agreement of a given signal, characterised by a value for μ, and of the background-only hypotheses with the observed data. The Neyman-Pearson lemma [86] states that the ratio of likelihoods constitutes an optimal test statistic. Hence, an appropriate choice is a test statistic based on the profile likelihood ratio:

$$\Lambda(\mu) = \frac{\mathcal{L}(\mu\,|\,\hat{\hat{\boldsymbol{\theta}}})}{\mathcal{L}(\hat{\mu}\,|\,\hat{\boldsymbol{\theta}})}\,, \tag{4.8}$$

where the parameters $\hat{\hat{\boldsymbol{\theta}}}$ are defined to yield the maximum likelihood for the specific value of μ and $(\hat{\mu},\,\hat{\boldsymbol{\theta}})$ are again the parameters that globally maximise the likelihood, thereby yielding $0 \leq \Lambda(\mu) \leq 1$. The test statistic is specified as profile likelihood ratio since the nuisance parameters are profiled for each value of μ individually.

Different types of test statistics can be constructed from the profile likelihood ratio Λ. The specific choice depending on whether one- or two-sided confidence limits are to be placed, and on physics assumptions of μ. The following definition [83] is used to set upper confidence limits on $\mathcal{B}_{H\to\text{inv}}$ in this Thesis:

$$\tilde{q}_\mu = \begin{cases} 0 & \mu < \hat{\mu}\,, \\ -2\ln\dfrac{\mathcal{L}(\mu\,|\,\hat{\hat{\boldsymbol{\theta}}}(\mu))}{\mathcal{L}(\hat{\mu}\,|\,\hat{\boldsymbol{\theta}})} & 0 \leq \hat{\mu} \leq \mu\,. \\ -2\ln\dfrac{\mathcal{L}(\mu\,|\,\hat{\hat{\boldsymbol{\theta}}}(\mu))}{\mathcal{L}(0\,|\,\hat{\hat{\boldsymbol{\theta}}}(0))} & \hat{\mu} < 0\,, \end{cases} \tag{4.9}$$

The motivation of the different terms is specified in the order of appearance:

1. To set a one-sided *upper* limit on $\mu = \mathcal{B}_{H\to\text{inv}}$, there is no need to consider data with a value of μ below the most probable value $\hat{\mu}$ as less compatible than the obtained data.

2. The region above the most-probable value, $\hat{\mu} < \mu$, is covered by the nominal $-2\ln\Lambda(\mu)$, if $\hat{\mu}$ is positive.

3. The true value for the invisible branching fraction of the Higgs boson is assumed to be non-negative, although the most-probable value for a data set can be negative due to statistical downward fluctuations of backgrounds, and variations within systematic uncertainties. For a negative most-probable value $\hat{\mu} < 0$, the largest agreement between the data and the signal model is assumed at $\mathcal{B}_{H\to\text{inv}} = 0$, hence the likelihood is normalised to the maximum likelihood at $\mathcal{B}_{H\to\text{inv}} = 0$.

The test statistic based on $\Lambda(\mu)$ yields higher levels of disagreement between the underlying model with μ and the data for increasing $\tilde{q}_\mu$. The information that is needed to compute exclusion limits is the probability density function of the test statistic $f(\tilde{q}_\mu \,|\, \mu)$ under the assumption of the model corresponding to μ.

The Asymptotic Approximation

The distributions of the test statistic $\tilde{q}_\mu$ under the background and signal hypothesis can be estimated by MC simulations. This is done by evaluating $\tilde{q}_\mu$ for large numbers of pseudo-data sets, separately for each signal hypothesis μ. This estimation becomes increasingly computational demanding due to the potentially complex likelihood function involving a large number of bins and nuisance parameters. Approximative techniques are employed instead.

With a result from Wald [87], the following approximation holds for the distribution of the profile likelihood ratio in the large sample limit for a Gaussian distributed $\hat{\mu}$ with mean value μ' and width σ:

$$-2\ln\Lambda(\mu') = \frac{(\mu' - \hat{\mu})}{\sigma^2}\,. \tag{4.10}$$

The resulting distribution for $\tilde{q}_\mu$ using the Wald approximation and setting $\mu' = \mu$ to test the signal hypothesis μ is derived in [83]:

$$f(\tilde{q}_\mu \,|\, \mu) = \frac{1}{2}\delta(\tilde{q}_\mu) + \begin{cases} \dfrac{1}{2}\dfrac{1}{\sqrt{2\pi}}\dfrac{1}{\sqrt{\tilde{q}_\mu}}e^{-\tilde{q}_\mu/2} & 0 < \tilde{q}_\mu \leq \mu^2/\sigma^2\,, \\ \dfrac{1}{\sqrt{2\pi}(2\mu/\sigma)}\exp\left[-\dfrac{1}{2}\dfrac{(\tilde{q}_\mu + \mu^2/\sigma^2)^2}{(2\mu/\sigma)^2}\right] & \tilde{q}_\mu > \mu^2/\sigma^2\,. \end{cases} \tag{4.11}$$

This reduces the problem of computing the test statistic distribution $f(\tilde{q}_\mu \,|\, \mu)$ to derive a sufficient estimate for the standard deviation σ of $\hat{\mu}$. The *Asimov data set* [83] is introduced for this purpose. It is defined via the equation for the likelihood 4.6, setting the number of events for each bin (n_i, m_j) equal to their expectation values according to the hypothesis μ. Hence, the parameter values yielding the maximum likelihood for

the Asimov data set are the true parameter values. There are two options to define the Asimov data set for a given μ. The *pre-fit* Asimov adopts the numbers of expected signal and background events according to nominal values of the parameters $\boldsymbol{\theta}$. The *post-fit* Asimov data set employs the numbers of expected events according to the profiled parameter values for the given hypothesis, $\hat{\hat{\boldsymbol{\theta}}}(\mu)$. The likelihood function constructed using the Asimov data for μ can be shown [83] to yield an estimate for the width σ_{Asimov}, which can be used to compute the distribution $f(\tilde{q}_\mu \,|\, \mu)$:

$$\sigma_{\text{Asimov}} = \frac{(\mu - \hat{\mu})}{\sqrt{q_{\mu,\text{Asimov}}}}\,, \tag{4.12}$$

with $q_{\mu,\text{Asimov}} = -2\ln\Lambda_{\text{Asimov}}(\mu)$.

The Modified Frequentist CL_S Method

The upper exclusion limit can be calculated from the p-value, the probability to obtain a result at least as extreme as the observed result under the assumption of the signal hypothesis μ. Integrating the distribution of the test statistic $f(\tilde{q}_\mu \,|\, \mu)$ assuming μ, and using the test statistic corresponding to the observed data, $\tilde{q}_{\mu,\text{obs}}$, yields:

$$CL_{S+B}(\mu) \equiv P(\tilde{q}_\mu \geq \tilde{q}_{\mu,\text{obs}} \,|\, S+B) = \int_{\tilde{q}_{\mu,\text{obs}}}^{\infty} f(\tilde{q}_\mu \,|\, \mu)\,\mathrm{d}\tilde{q}_\mu\,. \tag{4.13}$$

Choosing a confidence level (CL) in advance of the computation, a hypotheses yielding a $CL_{S+B} < \alpha$ can be excluded at a CL of $1-\alpha$. The commonly quoted CL of 95% corresponds to an upper exclusion limit on μ at which a scanned, or an iteratively computed $CL_{S+B} < \alpha = 0.05$ is found.

However, this method yields some undesired behaviour in situations where the test statistic distribution for the background-only hypothesis $f(\tilde{q}_\mu \,|\, 0)$ features an overlap with the signal+background distribution $f(\tilde{q}_\mu \,|\, \mu)$. With increasing overlap, the search becomes less sensitive to the signal model studied due to diminishing power to distinguish between the background-only and the signal case. This is the case since both hypothesis model the observation nearly equally. The computation of CL_{S+B} alone does not account for this decreasing sensitivity. A possible result is illustrated by two searches with the same signal prediction. In case of a downward fluctuation of the background, the search with a higher background prediction would quote a stronger observed exclusion limit.

The CL_S method [88] accounts for that effect by penalising the confidence in cases of similarly good or poor compatibility between the observed result and the background-only hypothesis described by $1 - CL_B$:

$$1 - CL_B(\mu) \equiv P(\tilde{q}_\mu \leq \tilde{q}_{\mu,\text{obs}} \,|\, B) = \int_{-\infty}^{\tilde{q}_{\mu,\text{obs}}} f(\tilde{q}_\mu \,|\, 0)\,\mathrm{d}\tilde{q}_\mu\,. \tag{4.14}$$

The value of CL_S is defined by:

$$CL_S(\mu) \equiv \frac{CL_{S+B}(\mu)}{1 - CL_B(\mu)}\,. \tag{4.15}$$

The procedure results in a less stringent exclusion limit due to $CL_S \geq CL_{S+B}$, hence some level of conservatism is introduced. For well separated distributions $f(\tilde{q}_\mu \,|\, 0)$ and $f(\tilde{q}_\mu \,|\, \mu)$, corresponding to a significant signal, the CL_S value approaches CL_{S+B}. The CL_S value is not strictly a p-value any longer, the derived upper limits from its value are therefore referred to as *modified* frequentist limits.

The *observed* upper exclusion limits at 95% thus exclude signal hypotheses with values of $CL_S \leq 0.05$ computed with the test statistic corresponding to the observed data, $\tilde{q}_{\mu,\text{obs}}$. The derivation is implemented technically employing an iterative approach to estimate the value of $\mathcal{B}_{H\to\text{inv}}$ resulting in $CL_S = 0.05$ with a relative precision of 0.05%.

The sensitivity of the search is assessed with the median upper exclusion limit that would be obtained if no signal were present. This corresponds to the *expected* upper limit which is computed with the CL_S method using the test statistic given by the median of the background-only distribution, $f(\tilde{q}_\mu \,|\, 0)$. This median is derived from the Asimov data set: $\text{med}[f(\tilde{q}_\mu \,|\, 0)] = \tilde{q}_{\mu,\text{Asimov}}$. The uncertainty bands on the expected limit describe by how much the observed limit is expected to vary given statistical and systematic fluctuations. They are computed by repeating the CL_S method with the test statistics corresponding to the quantiles around the median $\tilde{q}_{\mu,\text{Asimov}}$ which cover the intervals according to one and two standard deviations.

4.1.3. Combination Method

The combination of the statistical models of different searches for invisible decays of the Higgs boson is performed on the level of their likelihood functions. The underlying method is illustrated in the following with an example of two searches, the extension to larger numbers of searches being combined uses the same principle. Considering searches A and B with fully defined likelihood functions $(\mathcal{L}_A, \mathcal{L}_B)$ including sets of nuisance parameters $(\boldsymbol{\theta}^A, \boldsymbol{\theta}^B)$ and parameters of interest $(\mathcal{B}^A_{H\to\text{inv}}, \mathcal{B}^B_{H\to\text{inv}})$, the combined likelihood function is obtained by a product of the likelihood functions of the two searches, consistent to combining different bins:

$$\mathcal{L}_{\text{comb.}}(\mathcal{B}^{\text{comb.}}_{H\to\text{inv}} \,|\, \boldsymbol{\theta}^A, \boldsymbol{\theta}^B) = \mathcal{L}_A(\mathcal{B}^A_{H\to\text{inv}} \,|\, \boldsymbol{\theta}^A) \times \mathcal{L}_B(\mathcal{B}^B_{H\to\text{inv}} \,|\, \boldsymbol{\theta}^B)\,, \tag{4.16}$$

where the individual parameters of interest were mapped onto a single combined parameter $\mathcal{B}^{\text{comb.}}_{H\to\text{inv}}$, which is from here on referred to as $\mathcal{B}_{H\to\text{inv}}$.

This construction assumes that there are no correlations between the nuisance parameters. Hence, the combined likelihood features two independent sets of parameters. However, some sources of systematic uncertainty are correlated between the searches combined in this Thesis. They are conducted using same detector (instrumental) and may use predictions for signal or background processes calculated with the same method (theory). One example is the uncertainty on the integrated luminosity and its associated nuisance parameter which is here assumed to be identical in both searches. An increase in the integrated luminosity within its uncertainty should affect the predictions in both searches simultaneously. Contrarily, profiling the combined likelihood will result in both luminosity nuisance parameters to vary independently, possibly in different directions. This is in disagreement with the fact that both parameters describe the same instrumental effect.

If two systematic uncertainties corresponding to the nuisance parameters (θ_X^A, θ_X^B) are identified to describe the same effect X, this correlation assumption has to be implemented into the combined likelihood. Both nuisance parameters and their constraining priors are replaced by a single nuisance parameter $\theta_X^{A,B}$ with constraining prior that acts simultaneously on both searches in the profiling procedure. Splitting the sets of nuisance parameters into correlated and uncorrelated parts yields for the combined likelihood function:

$$\begin{aligned} &\mathcal{L}_{\text{comb.}}(\mathcal{B}_{H\to\text{inv}} \,|\, \boldsymbol{\theta}^{A,B}_{\text{correlated}}, \boldsymbol{\theta}^{A}_{\text{uncorrelated}}, \boldsymbol{\theta}^{B}_{\text{uncorrelated}}) = \\ &\mathcal{L}_A(\mathcal{B}^A_{H\to\text{inv}} \,|\, \boldsymbol{\theta}^{A}_{\text{correlated}}, \boldsymbol{\theta}^{A}_{\text{uncorrelated}}) \times \mathcal{L}_B(\mathcal{B}^B_{H\to\text{inv}} \,|\, \boldsymbol{\theta}^{B}_{\text{correlated}}, \boldsymbol{\theta}^{B}_{\text{uncorrelated}}) \,, \end{aligned} \tag{4.17}$$

where the nuisance parameters identified as correlated between the individual searches ($\boldsymbol{\theta}^A_{\text{correlated}}, \boldsymbol{\theta}^B_{\text{correlated}}$) were mapped into a single set $\boldsymbol{\theta}^{A,B}_{\text{correlated}}$ affecting both searches in the combined likelihood.

The combined likelihood as defined in Equation 4.17 can be used to compute the most probable value for $\mathcal{B}_{H\to\text{inv}}$ given the combined statistical model when profiled to the combined observed data set. Upper exclusion limits are derived by constructing the test statistic $\tilde{q}_\mu$ as described above from the combined likelihood. Regions of different searches can constrain nuisance parameters across the searches in the combined likelihood, analogously to the addition of regions into the likelihood of a single search. The profiling acts then as simultaneous measurement of the invisible branching fraction of the Higgs boson and of all included systematic uncertainties in all signal topologies combined.

Technical Implementation

The technical implementation of the studies is based on the ROOT framework [89]. Furthermore, functionalities from RooStats and RooFit are used which provide container objects for the statistical models of a search, and functionalities for likelihood minimisations and the derivation of exclusion limits. The MINOS algorithm is employed to derive uncertainties on the most probable value for $\mathcal{B}_{H\to\text{inv}}$ in the estimation of the impact of systematic uncertainty sources. The HESSE algorithm was found to yield results not accurate enough because of non-linearities in the combined likelihood model, in particular for the increasingly complex combination of Run 1+2 searches.

4.2. Object Definitions

This section gives an introduction into the reconstruction, and sources of systematic uncertainty of the main objects used in the ATLAS searches for invisible Higgs boson decays combined in this Thesis.

4.2.1. Jets

The hadronic final state of an interaction in particle colliders consists of strongly interacting quarks and/or gluons. However, the strong force precludes the measurement of

free partons inasmuch that it allows only for colour neutral objects (confinement). The strong force features a running coupling that is large at low energies. At high energies, as achieved in collider experiments, the coupling becomes weaker and partons can be described as asymptotically free.

The final state partons are in a state of asymptotic freedom. Gluons are radiated off with a high cross section, and split further into quark anti-quark pairs. This fragmentation and showering process continues until the coupling is strong enough for confinement to set in due to the decreasing energy per parton. The particles form colourless bound states that may decay further to longer lived particles. The parton showering process is not calculable perturbatively because of the large large coupling in this energy regime. Two models are primarily used for the description, the cluster hadronisation [90, 91], and the Lund string model [92].

The collimated sprays of hadrons resulting from the hadronisation are described by jets. The particles deposit energy in the calorimeter with a characteristic shower shape. The charged part of the shower additionally produces tracks in the inner detector. Clustering algorithms based on sequential recombination are used to combine the detector signals into the jet observable. The aim of this algorithms is to describe the spray of hadrons as exact as possible. The jet algorithms can run on the information of calorimeter clusters (calorimeter jet) or similarly on inner detector tracks (track jets). Thereby, jets are a definition depending on the actual choice of clustering algorithm and input.

The jet algorithm mainly employed by ATLAS and used in the searches combined here is the anti-k_t algorithm [93] which produces approximately circular jets with a certain radius $R = \sqrt{\phi^2 + \eta^2}$ centred around its most energetic input cluster/track. Two different radius parameters are utilised depending on the particle being searched for and its kinematics. The radius $R = 0.4$ is used to capture the hadronisation products of a single quark or gluon. These can be final state particles or the product of further decays of massive final state particles decaying to quarks before reaching the detector. This is the case for W/Z and Higgs bosons, top quarks as well as postulated and searched for heavier particles, such as the Z' boson or gravitons. For low to medium energies, the decay products of these particles are well separated and their parton showers are captured by individual $R = 0.4$ jets. The angle between the decay products decreases with the momentum p_{T} (also referred to as boost) of the mother particle of mass m, approximately with $\Delta R \approx 2m/p_{\mathrm{T}}$ for a two-body decay. At large boost, the showers of the single quarks will start to overlap and can not be described by two $R = 0.4$ jets. In that case, *Large-R jets* with $R = 1.0$ are employed that are expected to capture most of the products of the decaying particle. In addition to the jet mass, substructure techniques [94–96] are used in order to differentiate between large-R jets originating from a single quark or gluon, and large-R jets with separated energy depositions compatible with the decay of a massive particle.

The energy scale of the jets (JES) is calibrated [97] and corresponding systematic uncertainties are derived to account for effects such as: difference in calorimeter response to electromagnetic and hadronic showers, energy leakage from the calorimeter, less well instrumented parts of the detector, differences between the forward and central regions of the detector, and parts of the parton shower falling outside of the capture region of the jet. The mass scale of the large-R jets (JMS) is calibrated in a similar manner [98].

The hard-scatter *primary vertex* is defined by the searches as the vertex with the highest p_{T} sum of the tracks associated to it. The identification of jets originating from hadrons containing b-quarks (flavour tagging) [99–101] is performed using a multivariate discriminant, combined from outputs of three different algorithms. Inner detector tracks are geometrically matched to a calorimeter jet. The first input algorithm exploits the longer lifetime of b-hadrons resulting in a secondary vertex ($c\tau \approx 450\,\mu\mathrm{m}$). The longitudinal (transverse) impact parameter of a track describes the distance between the track at its closest approach and the primary vertex along the beam line (in $R - \phi$). These impact parameters are expected to be large for tracks of b-jets. The corresponding significances of both impact parameters are used to define a discriminating variable. The second input reconstructs secondary vertices by testing whether any pair of tracks inside the jet is consistent with originating from a common vertex, significantly displaced from the primary vertex. Properties such as the invariant mass of all tracks associated to the vertex, and the number of secondary vertices found in the procedure are used to define a discriminant. The third input uses the weak decay of a b-hadron by fitting a line between the primary vertex and the b- and c-hadron vertices. This approximates the line of flight of the b-hadron and the position of the vertices. A boosted decision tree is used to combine the outputs to a single discriminant *MV2* [101]. This yields efficiencies for b, c and *light* jets, where *light* jets are (u, d, s)-quark or gluon initiated.

Jets originating from pile-up are mitigated using the *jet vertex tagging* (JVT) [102, 103] algorithm providing a discriminant between hard-scatter and pile-up jets. The JVT variable is constructed by a two-dimensional likelihood obtained from the jet vertex fraction (JVF), and the R_{pT} variable. The JVF is the sum over the p_{T} of tracks associated to the jet and matched to the hard-scattering primary vertex, normalised to the sum of the p_{T} of all tracks matched to the hard-scattering primary vertex. The definition used for JVT is additionally corrected for the dependence on the number of primary vertices in the event. A low JVF value indicates that a jet is likely to originate from pile-up. The R_{pT} variable is the ratio of the p_{T} sum of all tracks associated to the jet and the hard-scattering primary vertex, and the calibrated as well as already pile-up corrected p_{T} of the jet. The mean value and spread of R_{pT} is expected to be larger for jets from the hard-scattering.

The full list of JES nuisance parameters that is provided by the jet performance group [104] to be used in analyses of 2015+2016 data contains 88 different parameters. Part of the JES is a nuisance parameter considering residual effects (nonclosure) in the calibration from central to forward regions of the detector, referred to as *eta-intercalibration*. Different levels of reduction are available for searches by diagonalisation of the effect of groups of uncertainty sources to a single parameter accounting for the combined effect of the group. This neglects some effects due to correlations between the combined sources. Further uncertainties on jets that are considered by the searches are related to the jet energy resolution (JER), properties of large-R jets including the JMS, the JVT discriminant, and the b-tagging efficiencies for b, c and *light* flavour jets.

4.2.2. Electrons

Electrons are reconstructed [105, 106] from tracks in the inner detector matched to energy depositions in the electromagnetic calorimeter where they deposit most of their energy. Two hypothesis are used for the fit of the inner detector hits to a continuous track: the pion and electron hypothesis. Both can cause an electromagnetic shower which is matched to a ID track. The hypotheses feature different assumptions on the energy loss in the detector material. If the default pion hypothesis fails, the electron hypothesis is used for a second fit. Electron candidate clusters are formed in the calorimeter with a clustering algorithm around a seed [107] and matched by ΔR to fitted tracks.

Electron identification (ID) based on a likelihood model is employed to distinguish signal electrons from photons that converted in the detector material into electron-positron pairs, or from mis-identified jets. This model uses different information, among these the shower-shape in the calorimeter, leakage into the hadronic calorimeter and pattern recognitions from the TRT. Based on the resulting likelihood, the electron candidates are assigned a quality label with increasing background rejection.

Moreover, isolation of the electron candidates is enforced to further distinguish between electrons from the hard-scattering and from decays of heavy-flavour hadrons as well as from mis-identified light hadrons. The isolation criteria require little additional activity in the detector assessed in cones around the electron candidate, based either on calorimeter or track information.

Systematic uncertainties associated to electrons [108] that are considered by the searches correspond to: the trigger efficiency, the energy scale and resolution, reconstruction, identification, and isolation.

4.2.3. Muons

Muons are reconstructed [109] primarily with information from the inner detector and the muon system but may use other information, such as from the calorimeter. Reconstructed tracks from the muon system matched to inner detector tracks form the basis of the typically used *combined muon* definition. This requirement is relaxed for *segment-tagged* muons for which the inner detector track is matched to a track reconstructed only in a segment of the MDT or CSC chambers. These are used if the muon passes only part of the muon system due to low momentum, or parts of low acceptance. Furthermore, the *calorimeter-tagged* muon definition can be used specifically in the very central region of $|\eta| < 0.1$, where the acceptance of the muon system is decreased due to instrumentation. The inner detector track is considered a muon candidate if the track is matched to energy deposits in the calorimeter that are consistent with a minimal ionising particle such as a muon.

Similarly to electrons, muon candidate undergo an identification step. Signal muons as produced directly in the decay of Z bosons are distinguished from background muons originating from secondary decays of mainly light hadrons in showers. This identification is based on the significance of the difference of charge to momentum ratios measured in the inner detector and muon systems, qualities of the track fit, and the difference between the momentum measure obtained from the inner detector and muon system separately.

Isolation criteria are used to further separate signal muons from muons that are produced in semileptonic decays. The detector activity around directly produced signal muons is expected to be lower compared to muons from kaon or pion decays resulting in jets. Therefore, calorimeter and track based isolation in cones is used for signal muon candidates as well.

Systematic uncertainties on muons [110] that are considered by the searches correspond to: the trigger efficiency, reconstruction, isolation, track to vertex association, track smearing in the inner detector and muon system to account for detector efficiency effects not well reproduced by MC simulation, the momentum scale, and charge-dependent effects on the momentum measurement.

4.2.4. Missing Transverse Momentum

The missing transverse momentum, $E_{\mathrm{T}}^{\mathrm{miss}}$, describes an imbalance in the transverse momentum of the reconstructed objects which is expected to sum to zero. A non-zero $E_{\mathrm{T}}^{\mathrm{miss}}$ value can be caused by a particle that escaped detection since its transverse momentum is not accounted for by the directly measured objects.

It is reconstructed [111] as the negative sum of the transverse momentum p_{T} of the reconstructed selected physics objects, referred to as *hard term*. This includes e.g. jets, charged leptons, and photons (which are not used in this Thesis). In addition, a *soft term* is added to the calculation based on either calorimeter or track information. The searches considered in this Thesis employ the track-based soft term which is defined by the tracks in the event that originate from the primary vertex but are not associated to any of the reconstructed objects comprising the hard term. This definition of the soft term misses charged particles but is less sensitive to pile-up due to the match between tracks and the primary vertex.

$$\begin{aligned} E_{\mathrm{T,x(y)}}^{\mathrm{miss}} &= -\sum_{\text{hard objects}} p_{x(y)} - \sum_{\text{soft term}} p_{x(y)} \\ \vec{E}_{\mathrm{T}}^{\mathrm{miss}} &= (E_{\mathrm{T,x}}^{\mathrm{miss}},\, E_{\mathrm{T,y}}^{\mathrm{miss}},\, 0) \\ E_{\mathrm{T}}^{\mathrm{miss}} &= \sqrt{(E_{\mathrm{T,x}}^{\mathrm{miss}})^2 + (E_{\mathrm{T,y}}^{\mathrm{miss}})^2} \end{aligned} \tag{4.18}$$

The reconstructed hard objects entering the calculation are used with their individual calibrations in order to arrive at a $E_{\mathrm{T}}^{\mathrm{miss}}$ quantity with optimal resolution. Systematic uncertainties on the hard objects are propagated to the missing transverse momentum. The soft term is not scale corrected but additional uncertainties are derived individually for the projections of the soft term parallel and perpendicular to the hard term [112].

In addition to particles depositing no energy in the detector, $E_{\mathrm{T}}^{\mathrm{miss}}$ can occur if the energy measurements of the involved objects vary within their systematic uncertainties. Especially jets can *fake* $E_{\mathrm{T}}^{\mathrm{miss}}$ due to (over-)underestimation of the jets energy in the calorimeters, in which case the $E_{\mathrm{T}}^{\mathrm{miss}}$ vector will point (anti-)parallel to the jet axis.

5. Inputs to the Statistical Combination

This Chapter introduces the direct ATLAS searches for invisible decays of the Higgs boson that are used in the statistical combination. The Run 2 analyses are described in Section 5.1 for $V_{q\bar{q}}H$, in Section 5.2 for $Z_{\ell\bar{\ell}}H$, and in Section 5.3 for VBF. The statistical combination of Run 1 searches is introduced in Section 5.4. This chapter concludes with a discussion on the statistical orthogonality of the analyses in Section 5.5.

5.1. Run 2 $V(\rightarrow$ hadrons$)H$

The search in the $V_{q\bar{q}}H$ topology with Run 2 data [6] is specialised on events featuring a large quantity of $E_{\mathrm{T}}^{\mathrm{miss}}$, and a hadronic system that is compatible with a W or Z boson. The Higgs boson and accordingly the $E_{\mathrm{T}}^{\mathrm{miss}}$ as the proxy for its invisible decay is expected to recoil against the hadronic system, resulting in a large separation in the transverse plane between both objects.

Two different regimes are considered depending on the boost of the vector boson V. The *resolved* regime is described by a low to intermediate energy of the vector boson resulting in a decay to well separated quarks. These are captured by two required *small-R* anti-k_t calorimeter jets with $R = 0.4$. In the *merged* regime, the two quarks are so close to each other that the showers cannot be separated reliably into two small jets. An anti-k_t calorimeter large-R jet with $R = 1.0$ is required in this regime instead.

The analysis is divided into different regions depending on the multiplicity of reconstructed b-jets, enhancing the signal sensitivity. The b-tagging algorithm identifies small-R jets containing a b-hadron. Track jets with a radius of $R = 0.2$ that are b-tagged and associated to the large-R jet are utilised in the merged regime. Three different regions are considered between zero and two reconstructed b-jets, separately for the resolved and merged regime.

The trimming [113] procedure is utilised to remove lower energetic components of the large-R jet that are expected to originate from pile-up. The mass of the large-R jet is calculated by a combination of a calorimeter-based quantity and an assisted quantity using calorimeter and tracking information [98]. This definition improves the mass resolution, in particular for very high momentum jets. Jet-substructure techniques are used in the merged regime to further differentiate between large-R jets originating from single quarks or gluons (background-like), and from two separated quarks each with significant energy (signal-like). Regions of high and low signal-like purities are defined by a cut on the D2 [94] observable in the merged zero and one reconstructed b-jet regions. The two b-jet region is statistically limited and remains inclusive.

The $E_{\mathrm{T}}^{\mathrm{miss}}$ is employed as the final discriminant for the distributions of signal and background processes. The various signal and control regions are individually represented in the statistical likelihood model of the analysis. The resulting observed (expected) CL_S upper exclusion limit on the invisible branching fraction of the Higgs boson at 95% CL is given by:

$$\mathcal{B}_{H\to\mathrm{inv}} < 0.83\ (0.58^{+0.23}_{-0.16})\,. \tag{5.1}$$

The search in the $V_{q\bar{q}}H$ topology is the least sensitive direct search for invisible Higgs boson decays due to the large backgrounds and systematic limitations, summarised below.

The main background processes are $t\bar{t}$ and V+jets production, exemplary Feynman diagrams are shown in Figure 5.3. A top quark predominantly decays to a bottom quark and a W boson. The production of top quark pairs can contribute to the signal selection in particular in the semi-leptonic decay chain. One of the W boson decays leptonically involving a neutrino yielding true $E_{\mathrm{T}}^{\mathrm{miss}}$. The second W boson decays hadronically to two quarks. The charged lepton can either escape detection or in case of a tau, can decay hadronically yielding a further jet. These events populate primarily the one and two b-jet regions due to the two b-hadrons from the top quark decays.

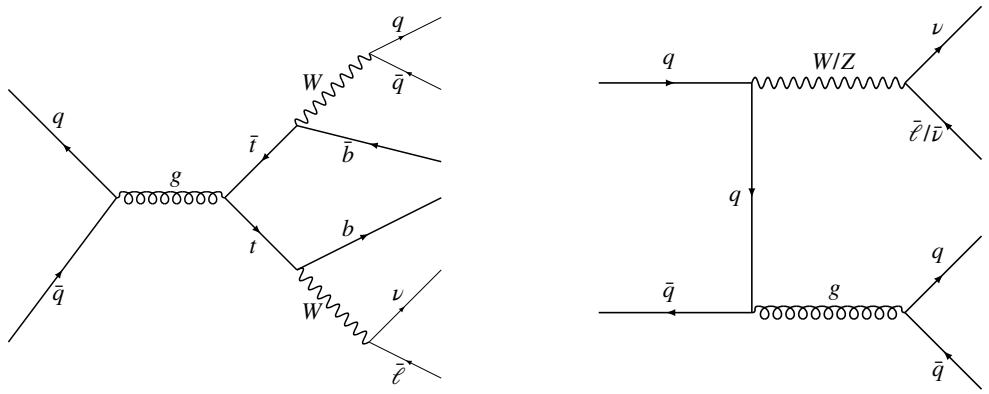

(a) Production of $t\bar{t}$ with semi-leptonic decay chain.

(b) Production of V+jets where the V boson decays leptonically.

Figure 5.1.: Exemplary Feynman diagrams for the main backgrounds in the $V_{q\bar{q}}H$ analysis.

The mass spectrum of QCD initiated jets is exponentially falling. However, a significant number of jets is expected in the mass range compatible with the V boson due to the large production rate. The $Z(\to \nu\nu)$+jets process where the jets fall into this mass window constitutes an irreducible background that cannot be distinguished from signal events. The W+jets process can contribute to the SR analogously to the discussion of the $t\bar{t}$ process for leptonic decays of the W boson. The predictions for the distribution of the $t\bar{t}$ and V+jets processes in the SR are estimated via MC simulations. The normalisations and $E_{\mathrm{T}}^{\mathrm{miss}}$ distribution shapes are additionally constrained from dedicated CRs in a data-driven way.

Minor background contributions arise from: the production of single top quarks with the W boson decaying to a tau lepton and corresponding neutrino, the production of two

vector bosons (diboson) with one boson decaying leptonically and the other hadronically, and QCD production of multiple jets (multijet) where jet energy measurements varying within experimental resolution yield fake $E_{\mathrm{T}}^{\mathrm{miss}}$. The former two processes are estimated from MC simulations. The multijet prediction from MC simulations is statistically limited and a projection based on a CR is employed instead.

5.1.1. Event Selection

The $V_{q\bar{q}}H$ search studies events which pass $E_{\mathrm{T}}^{\mathrm{miss}}$ trigger. Depending on the regime, two different sets of selection criteria are used. The selections of the merged regime are applied to an event first. If the event fails one of the criteria the selections of the resolved regime are applied.

Signal Regions

The selection criteria of the signal regions are summarised in the following:

- **Common criteria**: Events featuring any reconstructed electron or muon with $p_{\mathrm{T}} > 7\,\mathrm{GeV}$ are discarded, referred to as *lepton veto*. Further selections target the contribution from multijet processes, which are expected to feature $E_{\mathrm{T}}^{\mathrm{miss}}$ predominantly from variations in jet energy measurements. Requirements are set on the separation between the hadronic systems and the $E_{\mathrm{T}}^{\mathrm{miss}}$ to suppress this background. This accounts additionally for the signal topology of DM particles recoiling against the V boson.
  The separation in ϕ between the $E_{\mathrm{T}}^{\mathrm{miss}}$ and jets (or large-R jet) should be large: $\Delta\phi(E_{\mathrm{T}}^{\mathrm{miss}}, J\,\mathrm{or}\,jj > 120°)$, and the closest of the three leading small-R jets in ϕ is required to be separated from the $E_{\mathrm{T}}^{\mathrm{miss}}$: $\min_{i\in1,2,3}[\Delta\phi(E_{\mathrm{T}}^{\mathrm{miss}}, j_i)] > 20°$.
  The definition of a track-based missing transverse momentum $p_{\mathrm{T}}^{\mathrm{miss}}$ via the negative vector sum of the p_{T} of all tracks from the primary vertex with $p_{\mathrm{T}} > 0.5\,\mathrm{GeV}$ allows for further selections. Either $p_{\mathrm{T}}^{\mathrm{miss}} > 30\,\mathrm{GeV}$ or two b-jets are required. Furthermore, the track- and calorimeter-based $E_{\mathrm{T}}^{\mathrm{miss}}$ measures are required to be close to each other: $\Delta\phi(E_{\mathrm{T}}^{\mathrm{miss}}, p_{\mathrm{T}}^{\mathrm{miss}}) < 90°$.

- **Merged regime**: A $E_{\mathrm{T}}^{\mathrm{miss}}$ value above 250 GeV is required, corresponding to the large expected boost of the vector boson, which requires the energy of the Higgs boson ($E_{\mathrm{T}}^{\mathrm{miss}}$) to adopt higher values as well. At least one trimmed large-R jet with $p_{\mathrm{T}} > 200\,\mathrm{GeV}$ and no b-tagged track-jet outside of the highest p_{T} large-R jet which forms the W/Z boson candidate are required. The zero and one b-tag regions are divided in high and low signal purity by a cut on $D_2 < 1.2$. The allowed mass window of the large-R jet J varies for these b-tag regions. It is chosen around the W/Z mass to yield a fixed signal efficiency of 50% combining the requirements on the jet mass and D_2. The mass window for the D_2 inclusive two b-tag region is fixed to $75 < m_J^{\text{large-R}} < 100\,\mathrm{GeV}$.

- **Resolved regime**: A $E_{\mathrm{T}}^{\mathrm{miss}}$ value larger than 150 GeV is required. The hadronic system is represented by at least two small-R jets with $p_{\mathrm{T}} > 20\,(30)\,\mathrm{GeV}$ in the

central (forward) region. Maximally two b-tagged jets are allowed, targeting the $t\bar{t}$ and V+jets backgrounds with heavy flavour jets. The leading small-R jet is required to feature $p_{\mathrm{T}} > 45$ GeV, and the sum of the p_{T} of all small-R jets is asked to exceed 120 (150) GeV for events with two (three or more) jets. This is required to accurately model the trigger efficiency. The W/Z boson candidate is formed by the two reconstructed b-jets, or by the two leading jets in case of fewer b-jets. These two jets are expected to be relatively close to each other and feature a mass compatible with the W/Z boson mass. This translates into a requirement on the separation between both jets in the transverse plane of $\Delta R \lesssim 1.4$, and on the di-jet mass of $65 < m_{jj} \lesssim 105\,\mathrm{GeV}$, depending on the number of b-jets.

Background Control Regions

The CRs are divided into resolved and merged regimes, as well as b-tagging categories analogously to the SRs to select events that are kinematically similar to the corresponding SRs. No differentiation into high and low signal-like purity is employed in the CRs. Two CRs allowing for charged leptons are constructed, enriched in the main background processes. Information in these CR is used to constrain the corresponding normalisations and $E_{\mathrm{T}}^{\mathrm{miss}}$ distribution shapes in the SR. A further CR is constructed to obtain a prediction for the multijet contribution in the SRs.

The $t\bar{t}$ and W+jets backgrounds are constrained from a one-lepton CR. Selections similar to the SR are employed, but exactly one muon with $p_{\mathrm{T}} > 25\,\mathrm{GeV}$, and no further charged lepton is required. The allowance of a single muon represents the leptonic decay of the W boson (accordingly of one W boson for $t\bar{t}$), contributing to the SR if the charged lepton is not detected. The $t\bar{t}$ process is dominant in the one and two b-tag regions, whereas W+jets events are mainly expected in the zero b-tag region.
A two-lepton CR is constructed by requiring a pair of electrons or muons in the mass range $66 < m_{\ell\ell} < 116\,\mathrm{GeV}$, with $p_{\mathrm{T}} > 25\,\mathrm{GeV}$ for at least one of the charged leptons. Events passing a single lepton trigger are considered for this CR. The $Z(\to \nu\nu)$+jets background process is represented by the kinematically very similar decay to charged leptons. This allows for an extrapolation to the $Z(\to \nu\nu)$+jets prediction in the SR by scaling with the appropriate ratio of branching fractions.
The observable used in the statistical analysis of the SR is $p_{\mathrm{T}}^{V} = E_{\mathrm{T}}^{\mathrm{miss}}$. Both lepton CRs employ modified definitions of $E_{\mathrm{T}}^{\mathrm{miss}}$ and the track-based quantity $p_{\mathrm{T}}^{\mathrm{miss}}$ for the selections and statistical interpretation. Here, the contributions of the charged leptons is subtracted, $E_{\mathrm{T}}^{\mathrm{miss,\,no\,lep.}}$ and $p_{\mathrm{T}}^{\mathrm{miss,\,no\,lep.}}$. This is done to ensure kinematic similarity between the SR without charged leptons, and the CRs.

The multijet CR is constructed using the same selection as the SR, but inverting the separation requirement on the jet closest to the $E_{\mathrm{T}}^{\mathrm{miss}}$. This cut represents the most effective multijet discriminant. The resulting distribution is corrected for contributions from non-multijet processes, estimated from MC simulation. A scale factor is required to account for the difference in the distribution due to the cut inversion. The mass-sidebands (inversion of the mass window) are employed without the requirements on the separation between the closest jet and the $E_{\mathrm{T}}^{\mathrm{miss}}$, and between the calorimeter- and track-based $E_{\mathrm{T}}^{\mathrm{miss}}$. The distributions before and after the inversion of the separation requirement can

be studied in this region and the ratio is computed. The distribution in the multijet CR scaled by the ratio is then used as the multijet estimate in the SR.

5.1.2. Uncertainty Treatment

The full list of nuisance parameters and the corresponding categories of systematic uncertainty taken into account in the $V_{q\bar{q}}H$ analysis is shown in Table A.3. The categories of systematic uncertainty with the largest impact on the invisible branching fraction of the Higgs boson assessed with the nominal signal hypothesis are jets (in particular large-R), leptons, MC statistic, and the multijet and signal modelling. The analysis is found largely systematically limited with only minor impact of data-statistics. Only those sources of systematic uncertainty which require particular consideration in the construction of the correlation model are discussed in the following.

Experimental Uncertainties

- The systematic uncertainty on the JES affecting the small-R jets is represented by a strongly reduced set of three grouped NP and an additional NP accounting for the nonclosure in the eta-intercalibration.

- The systematic uncertainties on the efficiencies to identify jets containing b-hadrons (b-tagging) [114] for b, c and $light$ jets are each split into several eigenvectors ordered by impact, separately for calorimeter and track jets. Furthermore, two nuisance parameters are included corresponding to systematic uncertainties on the MC simulation based extrapolation to $p_{\mathrm{T}} > 300\,\mathrm{GeV}$ for b and c jets, where the data-based calibrations are limited by statistics [115].

Theory Uncertainties on the Signal

All three analyses assume SM Higgs boson production to generate MC signal predictions in the corresponding topologies. The Higgs boson is forced to decay invisibly via $H \rightarrow ZZ^* \rightarrow 4\nu$ with a branching ratio of 100%.

- The systematic uncertainty on the theoretical prediction for the signal process due to variations of QCD scales (renormalisation and factorisation) is estimated to account for effects of missing higher orders in perturbation theory used for the calculations. The $V_{q\bar{q}}H$ analysis considers the effect of QCD scale variations as separate nuisance parameters for the impact on the invisibly decaying Higgs boson signal cross section, acceptance, and $E_{\mathrm{T}}^{\mathrm{miss}}$ distribution shape.

- The impact due to the choice of a specific PDF set is assessed by comparison to alternative PDF sets. The systematic uncertainty is also represented with separate nuisance parameters for the impact on the signal cross section, acceptance and $E_{\mathrm{T}}^{\mathrm{miss}}$ distribution shape respectively.

- The systematic uncertainty due to the modelling of the parton shower is accounted for by comparing the results from the PYTHIA MC generator with different tune

parameters (MPI, Ren, Var1, Var2) [116, 117]. These vary the initial state radiation, final state radiation, and multi-parton interactions. The envelope of the variations compared to the nominal prediction is used as an estimate of the systematic uncertainty. Two nuisance parameters are implemented to account for the impact on the signal acceptance and $E_{\mathrm{T}}^{\mathrm{miss}}$ distribution shape. The cross section of the process is not affected by variations in the modelling of the parton shower.

5.2. Run 2 $Z(\rightarrow$ leptons$)H$

The search in the $Z_{\ell\bar{\ell}}H$ topology with Run 2 data [5] is specialised on events featuring a large quantity of $E_{\mathrm{T}}^{\mathrm{miss}}$ representing the invisible Higgs boson decay, recoiling against a pair of charged electrons or muons compatible with the decay of a Z boson.

Jets are defined with the anti-k_t algorithm using calorimeter clusters as input and a radius parameter of $R = 0.4$, requiring a minimum transverse momentum of $p_{\mathrm{T}} > 20\,\mathrm{GeV}$. The JVT discriminant is employed to differentiate between jets from the hard scattering and from pile-up in the low transverse momentum region. A flavour tagging algorithm is utilised to identify jets originating from b-hadrons.

The likelihood model of the analysis is divided into two separate SRs featuring either a pair of oppositely charged electrons or muons as Z boson candidate. The SRs are analysed in three bins of $E_{\mathrm{T}}^{\mathrm{miss}}$, which is used as final discriminant in the statistical interpretation. The resulting observed (expected) CL_S upper exclusion limit on the invisible branching fraction of the Higgs boson at 95% CL is given by:

$$\mathcal{B}_{H\rightarrow\mathrm{inv}} < 0.67\ (0.39^{+0.17}_{-0.11})\,. \tag{5.2}$$

The search in the $Z_{\ell\bar{\ell}}H$ topology is the second most sensitive direct search for invisible Higgs boson decays due to the accurately reconstructed leptonic system, and the requirements on $E_{\mathrm{T}}^{\mathrm{miss}}$. The weaker observed exclusion limit is primarily driven by an excess observed in the di-muon SR, but is not statistically significant.

The main backgrounds in the $Z_{\ell\bar{\ell}}H$ analysis are the production of two vector bosons (diboson), ZZ, and WZ, shown in the Feynman diagram in Figure 5.2.

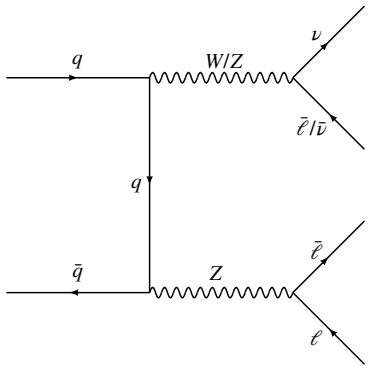

Figure 5.2.: Exemplary Feynman diagram for ZZ/WZ production with leptonic decays, constituting the main backgrounds in the $Z_{\ell\bar{\ell}}H$ analysis.

The dominant background are ZZ events where one Z boson decays into two electrons or muons, and the second decays into neutrinos. This process features $E_{\mathrm{T}}^{\mathrm{miss}}$ recoiling against two charged leptons from a Z boson. Hence, is cannot be distinguished from the signal and constitutes an irreducible background. An estimation of the ZZ distribution normalisation via $Z(\rightarrow \ell\ell)Z(\rightarrow \ell\ell)$ events and branching ratio scaling is not possible due to limited data statistics of four lepton events. A prediction based on MC simulation is used instead. The WZ process contributes to the signal selection if the Z boson decays to charged leptons, and the charged lepton from the leptonic W boson decay escapes detection or is a tau that decays hadronically. This background is estimated using MC simulation and is scaled with a factor obtained in a CR to account for possible missing higher perturbative orders in the simulation.

A further background are Z+jets events where the Z boson decays to electrons or muons. The process enters the SRs if the jet energy measurements vary considerably to yield $E_{\mathrm{T}}^{\mathrm{miss}}$ in the direction of the jets, opposite to the leptonic system. This background is estimated in a data-driven way employing several CRs, as discussed below. Moreover, two charged leptons from non-resonant decays of several particles can populate the SRs if the di-lepton system yields a mass around m_Z. Non-resonant contributions are expected from $t\bar{t}$, Wt, WW and $Z(\rightarrow \tau\tau)$ processes. A dedicated CR is constructed to estimate the yield in the SRs. Marginal backgrounds are triboson production (VVV), and $t\bar{t}$ with one or two further vector bosons. Their contributions are estimated from MC simulation.

5.2.1. Event Selection

The $Z_{\ell\bar{\ell}}H$ analysis considers events which pass single lepton trigger. The SRs for electron and muon pairs feature the same selections apart from the charged lepton flavour, and are summarised together with the background CRs in the following.

Signal Regions

Two electrons or muons with opposite electric charge are required with a $p_{\mathrm{T}} > 30\,(20)\,\mathrm{GeV}$ for the leading (subleading) lepton. Events containing a third charged lepton with $p_{\mathrm{T}} > 7\,\mathrm{GeV}$ are discarded to suppress contributions from the WZ process. The two leptons are expected to originate from a Z boson decay. Hence, the di-lepton mass is required in a window around the Z boson mass: $76 < m_{\ell\ell} < 106\,\mathrm{GeV}$. A large quantity of $E_{\mathrm{T}}^{\mathrm{miss}} > 90\,\mathrm{GeV}$ is required to account for the invisible Higgs boson decay. Contributions due to large $E_{\mathrm{T}}^{\mathrm{miss}}$ from varying jet energy measurements are reduced by defining H_T as scalar p_{T} sum of the selected jets and leptons, and requiring $E_{\mathrm{T}}^{\mathrm{miss}}/H_T > 0.6$. A minimal separation between the di-lepton system and the $E_{\mathrm{T}}^{\mathrm{miss}}$ vector of $\Delta\phi(p_{\mathrm{T}}^{\ell\ell}, E_{\mathrm{T}}^{\mathrm{miss}}) > 2.7\,\mathrm{radians}$ is imposed to account for the expected recoiling signal topology. Analogously, the two charged leptons from the Z boson decay are required to be close: $\Delta R_{\ell\ell} < 1.8$. The p_{T} of the Z boson, represented by $p_{\mathrm{T}}^{\ell\ell}$, is expected to balance the $E_{\mathrm{T}}^{\mathrm{miss}}$ in signal events. A requirement on the maximally allowed imbalance is imposed to reduce Z+jets events contributing due to a sizeable $E_{\mathrm{T}}^{\mathrm{miss}}$ soft-term: $|p_{\mathrm{T}}^{\ell\ell} - p_{\mathrm{T}}^{\mathrm{miss,\,jets}}|/p_{\mathrm{T}}^{\ell\ell} < 0.2$, where $p_{\mathrm{T}}^{\mathrm{miss,\,jets}}$ is

the $E_{\mathrm{T}}^{\mathrm{miss}}$ without the p_{T} of the selected jets. Background processes involving a top quark are suppressed by discarding events featuring any identified b-jet with $p_{\mathrm{T}} > 20\,\mathrm{GeV}$.

Background Control Regions

A scale factor for the WZ background contribution is derived from a CR that is constructed using the SR selections but requiring a third charged lepton. The third lepton represents the escaped or hadronically decaying charged lepton from the W boson. The m_T^W quantity is defined as sum of the $E_{\mathrm{T}}^{\mathrm{miss}}$ and the third leptons p_{T}. It represents the W boson and is required above 60 GeV to enrich this region further in WZ events. The SR scale factor is determined, after subtraction of further contributions from MC simulations, as ratio between the resulting and predicted distribution.

The Z+jets contribution is estimated using a technique referred to as ABCD method. It employs four regions, the SR (A) and three Z+jets enriched regions (B, C, D). These enriched regions are chosen such that the assumption on the Z+jets yield in the regions $N_A/N_B = N_C/N_D$ approximately holds. This allows for the determination of N_A in the SR from the yields in the three other regions. The closure of this assumption is found to be consistent with unity, considering the large statistical and systematic uncertainties on the yields. These uncertainties propagate further to the Z+jets estimate in the SR. Region B is defined by events which fail either $E_{\mathrm{T}}^{\mathrm{miss}} > 90\,\mathrm{GeV}$ or $E_{\mathrm{T}}^{\mathrm{miss}}/H_T < 0.6$. Events in region C satisfy both, but fail other signal selections. The remaining events populate region D.

The non-resonant contribution in the SR is estimated by the event yield after employing the signal selections on events with two oppositely charged, but different flavour leptons $e\mu$. Contributions from other backgrounds are subtracted using MC simulation. Furthermore, the difference in efficiency between selecting different and same flavour charged lepton pairs is taken into account.

5.2.2. Uncertainty Treatment

The full list of the nuisance parameters and corresponding categories of systematic uncertainty considered by the $Z_{\ell\bar{\ell}}H$ analysis is shown in Table A.2. The result of the analysis is mainly limited by data statistics. The most significant categories of systematic uncertainty are the theoretical modelling of the ZZ background, the luminosity, jets, and the predictions for WZ and Z+jets background yields by employing CRs. In the following, only those sources of systematic uncertainty are discussed which require special attention in the construction of the correlation model.

Experimental Uncertainties

- The systematic uncertainty on the JES is represented by a strongly reduced set of three grouped nuisance parameter and an additional nuisance parameter accounting for the nonclosure in the eta-intercalibration.

- The systematic uncertainties on the b-tagging efficiencies for b, c and *light* jets are each represented by a single nuisance parameter. These correspond to the combined

effect of the eigenvectors considered in the $V_{q\bar{q}}H$ analysis. Two nuisance parameters are included corresponding to systematic uncertainties on the MC simulation based extrapolation to higher p_{T} regions for b and c jets.

Theory Uncertainties on the Signal

- The systematic uncertainty on the signal prediction due to variations of the QCD scales are represented by a nuisance parameter corresponding to the effect on the cross section.
- Similarly, the impact due to the choice of a specific PDF set on the signal prediction is estimated by comparison to alternative sets, and represented by a nuisance parameter affecting the cross section.
- The systematic uncertainty due to different modelling of the parton shower is estimated, but is found to have negligible impact on the result.

Theory Uncertainties on Backgrounds

The effect of QCD scale variations on the theoretical prediction for the ZZ background process is accounted for by a corresponding nuisance parameter.

5.3. Run 2 Vector-Boson-Fusion

The search in the VBF topology with Run 2 data [4] is specialised on events featuring a large quantity of $E_{\mathrm{T}}^{\mathrm{miss}}$ corresponding to the invisible Higgs boson decay, and two very forward jets in opposite hemispheres of the detector originating from the quarks that radiated off the vector bosons.

The anti-k_t algorithm with a radius parameter of $R = 0.4$ is employed on calorimeter clusters to define jets, requiring a minimum transverse momentum of $p_{\mathrm{T}} > 25\,\mathrm{GeV}$. Pile-up jets are suppressed in the low p_{T} region by using the JVT discriminant.

The SR and correspondingly the statistical interpretation in the likelihood model is divided in three bins of $E_{\mathrm{T}}^{\mathrm{miss}}$. The largest signal sensitivity is expected in the highest $E_{\mathrm{T}}^{\mathrm{miss}}$ bin. The resulting observed (expected) CL_S upper exclusion limit on the invisible branching fraction of the Higgs boson at 95% CL is given by:

$$\mathcal{B}_{H\to\mathrm{inv}} < 0.37\ (0.28^{+0.11}_{-0.08})\,. \tag{5.3}$$

The search in the VBF topology is the most sensitive of the individual direct searches for invisible Higgs Boson decays due to the comparably large production cross section, and powerful QCD suppression achieved by the $E_{\mathrm{T}}^{\mathrm{miss}}$ and forward jets requirements summarised below.

The dominant background are V+2 jets events. These events are differentiated into two different production modes. Gluons are radiated off initial state quarks which fuse into a V boson in the *strong* production mode. The *weak* production mode resembles the Higgs boson production via VBF, but a V boson is produced instead of the Higgs boson.

Feynman diagrams for both processes are shown in Figure 5.3.

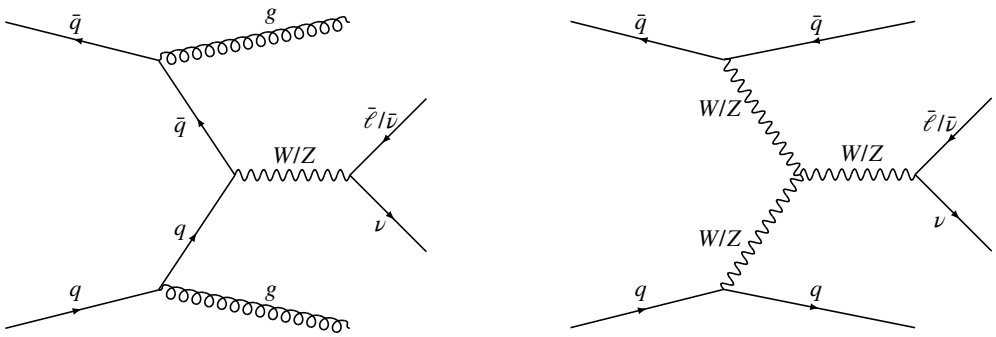

(a) Strong production of V+2 jets. **(b)** Weak production of V+2 jets.

Figure 5.3.: Exemplary Feynman diagrams for the V+2 jets production with leptonic decay of the V boson, constituting the main backgrounds in the VBF analysis.

In both cases, the additional jets are directed in the forward regions of the detector similarly to the signal topology. The $E_{\mathrm{T}}^{\mathrm{miss}}$ is yielded either by the decay of the Z boson to neutrinos, or from the W boson decaying into a leptonically, where the charged lepton escapes detection. Dedicated CRs are constructed to determine the SR normalisation of the Z+2 jets and W+2 jets distributions estimated from MC simulation. The background contribution from multijet events featuring $E_{\mathrm{T}}^{\mathrm{miss}}$ due to variations in the jet energy measurements are estimated from a multijet enriched selection of events passing a single jet trigger. Minor backgrounds are expected from processes involving top quarks and dibosons. Predictions from MC simulations are used for the SR yields of these backgrounds.

5.3.1. Event Selection

Events are considered for the VBF SR if they pass $E_{\mathrm{T}}^{\mathrm{miss}}$ trigger. The SR selections and construction of CRs for the V+2 jets and multijet backgrounds are summarised in the following.

Signal Region

The signal topology exclusively features jets and $E_{\mathrm{T}}^{\mathrm{miss}}$. Hence, events containing any reconstructed isolated electron or muon with $p_{\mathrm{T}} > 7\,\mathrm{GeV}$ are discarded. The (sub)leading jet is required with $p_{\mathrm{T}} > 80\,(50)\,\mathrm{GeV}$. Events including any reconstructed third jet with $p_{\mathrm{T}} > 25\,\mathrm{GeV}$ are vetoed. A minimum requirement of $E_{\mathrm{T}}^{\mathrm{miss}} > 180\,\mathrm{GeV}$ is imposed, representing the invisible Higgs boson decay. The $H_{\mathrm{T}}^{\mathrm{miss}}$ quantity is defined via the magnitude of the p_{T} sum of all jets, regardless of whether they pass or fail the JVT requirement. Events are selected if they additionally feature $H_{\mathrm{T}}^{\mathrm{miss}} > 150\,\mathrm{GeV}$, to account for cases in which large $E_{\mathrm{T}}^{\mathrm{miss}}$ arises due to a high-p_{T} jet failing the JVT requirement. Further selections consider the geometry of the signal topology. The jets j are expected to be separated

from the $E_{\mathrm{T}}^{\mathrm{miss}}$: $|\Delta\phi(E_{\mathrm{T}}^{\mathrm{miss}}, j)| > 1$, not be back-to-back: $|\Delta\phi_{jj}| < 1.8$, should feature a large separation in pseudorapidity: $|\Delta\eta_{jj}| > 4.8$, are expected in different hemispheres of the detector: $\eta_{j1} \times \eta_{j2} < 0$, and feature a very large di-jet mass driven by the separation: $m_{jj} > 1\,\mathrm{TeV}$.

Background Control Regions

The normalisation for the MC simulation of the $W(\to \ell\nu)$+2 jets background distribution in the SR is estimated in a CR. The CR employs the SR selections but allows for a single electron or muon, representing the leptonic decay of the W boson. The region is further divided according to the flavour and charge of the lepton. The estimate is improved by accounting for jets mis-identified as an electron. Information on mis-identified jets is obtained from additional regions split from the one electron CRs. Required is a low $E_{\mathrm{T}}^{\mathrm{miss}}$ significance, defined here as $S_{\mathrm{MET}} = E_{\mathrm{T}}^{\mathrm{miss}}/\sqrt{p_{\mathrm{T}}^{j1} + p_{\mathrm{T}}^{j2} + p_{\mathrm{T}}^{e}} < 0.4\,\sqrt{\mathrm{GeV}}$. The observable is motivated by the general form of a significance $S_x = x/\sigma(x)$, and the resolution of the energy measurement which is proportional to $\sqrt{E}$. A low S_{MET} value thus selects events which are likely to contain mis-identified jets yielding fake $E_{\mathrm{T}}^{\mathrm{miss}}$.

The normalisation for the simulated $Z(\to \nu\nu)$+2 jets background distribution in the SR is estimated in a CR allowing for two oppositely charged electrons or muons in a di-lepton mass window of 25 GeV around m_Z. Due to the similar kinematics of the Z boson decaying to charged leptons or neutrinos, this distribution can be scaled by the appropriate branching fractions and used for the estimation of the normalisation.

A $E_{\mathrm{T}}^{\mathrm{miss}}$ quantity without the contribution of the charged leptons is employed in the one and two lepton CRs, which is kinematically more similar to the $E_{\mathrm{T}}^{\mathrm{miss}}$ in the SR without charged leptons.

The multijet background prediction from MC simulation is statistically limited, similar to the $V_{q\bar{q}}H$ analysis. Instead, a multijet enriched region with events that pass a single jet trigger is used with a rebalance and smear method [118]. Some multijet events are expected to yield sufficient $E_{\mathrm{T}}^{\mathrm{miss}}$ to populate the SR due to experimental systematic variations in the energy measurements of the jets. The acceptance of these events in the SR is estimated by rebalancing the jets to yield only the $E_{\mathrm{T}}^{\mathrm{miss}}$ soft term, and subsequently smearing the jets properties multiple times with templates which model the experimental response. The method is further validated in a sideband of $1.8 < \Delta\phi_{jj} < 2.7$, allowing for a third jet, and loosening requirements on $m_{jj} > 0.6\,\mathrm{TeV}$, and on the separation in $\eta_{jj} > 3$.

5.3.2. Uncertainty Treatment

The full list of nuisance parameters and corresponding categories of systematic uncertainty is shown in Table A.1. The VBF analysis particularly benefits from larger data statistics. The most significant groups of experimental systematic uncertainty are jets, the $E_{\mathrm{T}}^{\mathrm{miss}}$ soft term, leptons, and the limited size of background MC predictions, in particular for the very high di-jet mass region. Important theory uncertainties affect the modelling of the strong and weak production modes of V+2 jets distributions. In the following, only those

sources of systematic uncertainty are discussed that require attention in the construction of the correlation model.

Experimental Uncertainties

The systematic uncertainty on the JES is represented by a category-based reduced set of 29 nuisance parameters, including a nuisance parameter accounting for the nonclosure in the eta-intercalibration. The category-based scheme reduces detector, modelling, statistical, and mixed effects to a list of combined nuisance parameters per category. Additionally featured a several nuisance parameters for flavour dependent effects, the eta-intercalibration procedure, and pile-up corrections.

Theory Uncertainties on the Signal

- A nuisance parameter corresponding to the combined effect of QCD scale variations and of the third jet veto on the signal cross section is implemented.
- The choice of a specific PDF set on the signal cross section is represented by a corresponding nuisance parameter.
- The parton shower induced uncertainty on the signal is assessed by comparing variations in the PYTHIA MC generator, and further comparing to the alternative HERWIG generator. The envelope is used as a systematic uncertainty.
- Events from the gluon-gluon fusion production process of the Higgs boson can pass the event selection of the VBF analysis if two additional quarks or gluons are radiated off (ggF+2 jets). The values for the QCD scales influence the prediction for the number of ggF+2 jets events in the signal selection of the VBF analysis. Hence, the variation of QCD scales gives rise to an additional systematic uncertainty.

5.4. Run 1 Combination

The ATLAS collaboration performed searches with Run 1 data in the VBF [119], $Z_{\ell\bar{\ell}}H$ [120], and $V_{q\bar{q}}H$ [121] topologies. Furthermore, a Mono-jet analysis for two jets and $E_{\mathrm{T}}^{\mathrm{miss}}$ was reinterpreted as a search for invisible decays of the Higgs boson. The search was statistically combined with the Run 1 VBF search, ensuring the orthogonality between the signal selections of both searches. The phase spaces probed by the Mono-jet analysis feature either a lower di-jet mass, or a smaller separation between both jets compared to the VBF analysis. They and are referred to as SR2a and SR2b in the VBF analysis [119]. These direct searches for invisible Higgs boson decays were statistically combined to a full Run 1 result [3]. The CL_S upper exclusion limits on the invisible branching fraction of the Higgs boson of the individual searches and of the combination at a confidence level of 95% are shown in Table 5.1.

Similarly to the individual Run 2 search results, the experimental sensitivity is largest for the search in the VBF topology, and decrease for the searches in the $Z_{\ell\bar{\ell}}H$, and further in the $V_{q\bar{q}}H$ topology. The result of the statistical combination is primarily driven by the

Analysis	Exclusion limit	Reference
Run 1 VBF + Mono-jet	0.28 (0.31)	[119]
Run 1 $Z_{\ell\bar{\ell}}H$	0.75 (0.62)	[120]
Run 1 $V_{q\bar{q}}H$	0.78 (0.86)	[121]
Run 1 combination	0.25 ($0.27^{+0.10}_{-0.08}$)	[3]

Table 5.1.: The observed (expected) upper CL_S exclusion limits on $\mathcal{B}_{H\to\text{inv}}$ at 95% confidence level for the combination of all searches in Run 1 compared to the results in the individual searches.

VBF analysis. However, the VBF and $V_{q\bar{q}}H$ analyses in Run 1 observe less events than expected, resulting in stronger observed exclusion limits than the expected. This feature propagates to the combined result with a slightly stronger observed limit compared to the median of the expectation.

The full list of nuisance parameters considered in the combination of Run 1 searches is shown in Table A.5. In summary, the statistical combination of the Run 1 searches considered the following sources of systematic uncertainty as correlated:

- The uncertainty on the integrated luminosity.
- The uncertainty on the JES where applicable. The analyses used different reduction schemes similarly to Run 2. Systematic uncertainties were correlated in cases of clear correspondence.
- The uncertainty on the jet energy resolution.
- The uncertainty on the signal cross section due to QCD scale variations, the choice of a specific PDF set, and the parton shower modelling.

5.5. Statistical Orthogonality

The regions probed by the searches entering the statistical combination are required to be orthogonal, in order to avoid double counting of events. The Run 1 and 2 searches use independent data sets and are thereby orthogonal by definition. The orthogonality of the Run 2 searches is discussed in the following.

The selection criteria summarised in the previous sections ensure that the individual searches are statistically orthogonal, both in the SRs and CRs. The search in the $Z_{\ell\bar{\ell}}H$ topology requires two charged leptons together with $E_{\text{T}}^{\text{miss}}$, eliminating possible overlap with the VBF and $V_{q\bar{q}}H$ selections. The VBF and $V_{q\bar{q}}H$ searches are orthogonal by construction due to the di-jet mass requirement of $m_{jj} > 1\,\text{TeV}$ in the VBF search, which is incompatible with the window around the W/Z boson mass selected in the $V_{q\bar{q}}H$ search.

The most important selections of the three Run 2 searches are summarised in Table 5.2 for the SRs, and in Table 5.3 for the main background CRs.

The orthogonality is verified explicitly by applying the selection criteria of the individual searches to a representative subset of the data, corresponding to about $0.5\,\text{fb}^{-1}$ of integrated luminosity and has a pile-up profile typical for Run 2 covering between 14.3 and 34.2 proton-proton collision in a single bunch-crossing. No common event that is used in the statistical interpretations of the data is selected by the different searches. This is true for both the SRs and CRs. Thus, it is concluded that the input searches use statically orthogonal data sets at the level of statistical precision of this test, which uses more than 1% of the analysed data set. Any statistical overlap potential at a level of below 1% would have a negligible statistical impact.

Table 5.2.: Summary of the relevant SR selections of the three input analyses using VBF, $Z_{\ell\bar{\ell}}H$ and $V_{q\bar{q}}H$ Higgs production modes.

Channel	$E_{\text{T}}^{\text{miss}}$	N(jets)	p_{T}(jet)	m_{jj}	$\Delta\eta_{jj}$
VBF	$> 180\,\text{GeV}$	exactly 2	leading $> 80\,\text{GeV}$, subleading $> 50\,\text{GeV}$	bin in m_{jj} from $1 - 1.5\,\text{TeV}$ $1.5 - 2\,\text{TeV}$ $> 2\,\text{TeV}$	> 4.8
ZH	$> 90\,\text{GeV}$	≥ 0	$> 20\,\text{GeV}$	N/A	N/A
VH	$> 150\,\text{GeV}$ resolved, $> 250\,\text{GeV}$ merged	≥ 2 $R = 0.4$ resolved, ≥ 1 large-R merged	$> 20\,\text{GeV}$ $R = 0.4$ jets, $> 200\,\text{GeV}$ large-R jets	$65 < m_{jj} < 100\,\text{GeV}$ Resolved (0,1,2 b-tag), 50% sig. eff. with D_2 cut Merged (0,1 b-tag), $75 < m_{jj} < 100\,\text{GeV}$ Merged (2 b-tag)	N/A

Channel	N(b-jet)	p_{T} (b-jet)	N(lepton)	p_{T} (lepton)	other cuts
VBF	N/A	N/A	veto	$> 7\,\text{GeV}$	$\Delta\phi_{jj} < 1.8$
ZH	veto	$> 20\,\text{GeV}$	2	leading $> 30\,\text{GeV}$, subleading $> 20\,\text{GeV}$	$76 < \text{m}_{ll} < 106\,\text{GeV}$, $\Delta R_{ll} < 1.8$, $\Delta\phi(p_{\text{T}}(ll), E_{\text{T}}^{\text{miss}}) > 2.7$, p_{T} balance > 0.2, $E_{\text{T}}^{\text{miss}}/\text{HT} > 0.6$
VH	0/1/2	$> 20\,\text{GeV}$	veto	$> 7\,\text{GeV}$	merged: D_2 cut (for 0/1 b-tag), $\Delta\Phi(E_{\text{T}}^{\text{miss}}, \text{jet(s)}) > 120°$, $\Delta\Phi_{j1,j2} < 140°$, $\Delta R_{(j1,j2)} < 1.4(1.25)$ for 0,1(2) b-tags

Table 5.3.: Summary of the relevant CR selections of the three input analyses using VBF, $Z_{\ell\bar{\ell}}H$ and $V_{q\bar{q}}H$ Higgs production modes.

Channel	$E_{\mathrm{T}}^{\mathrm{miss}}$	N(jets)	p_{T}(jet)	m_{jj}	$\Delta\eta_{jj}$
VBF	$> 180\,\mathrm{GeV}$	exactly 2	leading $> 80\,\mathrm{GeV}$, subleading $> 50\,\mathrm{GeV}$	bin in m_{jj} from $1 - 1.5\,\mathrm{TeV}$ $1.5 - 2\,\mathrm{TeV}$ $> 2\,\mathrm{TeV}$	> 4.8
ZH	$> 90\,\mathrm{GeV}$	≥ 0	$> 20\,\mathrm{GeV}$	N/A	N/A
VH	$> 150\,\mathrm{GeV}$ resolved, $> 250\,\mathrm{GeV}$ merged, use $E_{\mathrm{T}}^{\mathrm{miss,\ no\ lep.}}$	≥ 2 $R = 0.4$ resolved, ≥ 1 large-R merged	$> 20\,\mathrm{GeV}$ $R = 0.4$ jets, $> 200\,\mathrm{GeV}$ large-R jets	see SR	N/A

Channel	N(bjet)	p_{T} (bjet)	N(lepton)	p_{T} (lepton)	other cuts
VBF	N/A	N/A	1 lepton W+jets CR, 2 leptons $Z(\ell\ell)$+jets CR	$> 30\,\mathrm{GeV}$ leading, $> 10\,\mathrm{GeV}$ subleading ($Z(\ell\ell)$+jets CR)	$\Delta\Phi(jj) < 1.8$, $S_{\mathrm{MET}} < 0.4$ W+jets CR for mis-ident. jets
ZH	veto	$> 20\,\mathrm{GeV}$	3 lep. (W/Z) CR, opp. sign $e\mu$ pair (non-resonant CR)	see SR for pair, $> 20\,\mathrm{GeV}$ third lepton	same as in SR +, 3 lep. CR: $m_{\mathrm{T}}(\mathrm{W}) > 60\,\mathrm{GeV}$, ABCD Z+jets: B:$E_{\mathrm{T}}^{\mathrm{miss}} < 90\,\mathrm{GeV}$ or $E_{\mathrm{T}}^{\mathrm{miss}}/H_{\mathrm{T}} < 0.6$, C: $E_{\mathrm{T}}^{\mathrm{miss}} > 90\,\mathrm{GeV}$ and $E_{\mathrm{T}}^{\mathrm{miss}}/H_{\mathrm{T}} > 0.6$, but fail other cuts, D: rest
VH	0/1/2	$> 20\,\mathrm{GeV}$	1 lepton W+jets CR, 2 leptons $Z(\ell\ell)$+jets CR	$> 7\,\mathrm{GeV}$ W+jets CR, $> 25\,\mathrm{GeV}$ $Z(\ell\ell)$+jets CR	$\Delta\Phi(E_{\mathrm{T}}^{\mathrm{miss,\ no\ lep.}}, \mathrm{jet(s)}) > 120°$, $\Delta\Phi_{j1,j2} < 140°$

6. Statistical Combination

This Chapter presents the statistical combinations of the searches for invisible Higgs boson decays. The model used to correlate systematic uncertainties between input channels for the Run 2 combination and between Run 1 and Run 2 are shown in Section 6.1. The results are shown in Section 6.2 for the Run 2 combination and in Section 6.3 for the Run 1+2 combination.

6.1. Correlation Model

The correlation model is the set of assumptions on the correlations between the sources of systematic uncertainty in the inputs to the statistical combinations.

The input searches employ *pruning* procedures which reduce the number of systematic uncertainties in their statistical analyses. Only those sources of systematic uncertainty that impact the parameter of interest, $\mathcal{B}_{H\to\text{inv}}$ non-negligibly are included. One example is the systematic uncertainty on the muon momentum scale which is insignificant for the result of the $V_{q\bar{q}}H$ search. The global correlation models for the combinations thus only take into account sources of systematic uncertainty that affect the result.

The nuisance parameters representing a given source of systematic uncertainty are constrained in the individual profile likelihood fits of the input searches as described in Section 4.1.1. In the context of this Thesis, a nuisance parameter is referred to as *over-constrained* either if it is constrained to 50% of the prior uncertainty, or is profiled to a value above $0.7\,\sigma$ with respect to the nominal. When correlating a given nuisance parameter between searches, care must be taken since this constraint is propagated between analyses. Its value becomes rather specific to the region of phase space considered in a given search, and may not be representative for the regions of phase space selected in the other searches. Furthermore, propagating strong constraints through correlations can introduce tensions and artificial biases in the profile likelihood fit. In accordance with the recommendations of the ATLAS *Higgs combinations* group and other measurements of Higgs boson couplings [122], the over-constrained nuisance parameters are uncorrelated while the corresponding nuisance parameters of the remaining input searches are correlated where applicable.

The input searches use different approaches to estimate several systematic uncertainties. Similarly, the representation of systematic uncertainties may differ between searches, e.g. due to reduction schemes. In such situations, there is no clear mapping between the nuisance parameters in the respective input searches. Examples include the systematic uncertainty on the *Jet Energy Scale* and the *parton shower modelling* which are described below. Assuming full correlation by introducing a common nuisance parameter in the combined profile likelihood model does not reflect the distinct estimation procedures.

Nuisance parameters are treated as uncorrelated in these situations since assuming a correlation would imply that there is an understanding and control over the source of systematic uncertainty that in fact there is not. Additional combined likelihood models are constructed with alternative correlation assumptions between nuisance parameters. The effect on the result is assessed by the exclusion limit on $\mathcal{B}_{H\to\text{inv}}$ compared to the exclusion limit obtained with the default correlation model. Their impact is small compared to the systematic uncertainties on the combined results and detailed in Appendix B.

6.1.1. Run 2 Combination

The Run 2 combination correlation model is described in the following. It includes systematic experimental uncertainties, and theory uncertainties on the invisibly decaying Higgs boson signal prediction. The methods used to estimate the different sources of backgrounds vary significantly between the input searches. The nuisance parameters reflecting the experimental and theory uncertainties on the background predictions are tailored to the specific techniques being used and the phase spaces being probed. Accordingly, there is no correlation assumed between systematic uncertainties on the background predictions.

Experimental Uncertainties

Many experimental uncertainties are treated coherently by the three input analyses and are represented by the same set of nuisance parameters in their statistical models. The corresponding nuisance parameters and their prior constraint are measured by performance groups inside the ATLAS collaboration, who provide recommendations for the analyses. Their correlation is technically realised as described in Section 4.1.3. The correlation model is discussed in the following and is summarised in Table 6.1.

- The systematic uncertainty on the integrated luminosity [123] is correlated across all input searches.

- The systematic uncertainties related to the detection of muons [109, 110] and electrons [108, 124] are correlated if they are taken into account by the searches. Nuisance parameters corresponding to systematic uncertainties on electrons describe the uncertainty on the triggering of electrons, on isolation requirements, on electron reconstruction, and on the energy scale and resolution. For muon detection, the nuisance parameters for systematic uncertainties on triggering, isolation, reconstruction, and the association of tracks to the primary vertex are split into systematic and statistical components. Further uncertainties on muons arise from track smearing in the inner detector and muon systems, the momentum scale, and charge dependent effects on the momentum scale [110].

- The systematic uncertainties on the jet energy scale (JES) for anti-k_t calorimeter jets with a radius parameter of $R = 0.4$ are considered to be partly correlated. The VBF search utilises a category-based reduction scheme with 29 nuisance parameters. Effects of categories such as detector, modelling and statistical uncertainties are

grouped into a list of combined nuisance parameters [104]. The $Z_{\ell\bar{\ell}}H$ and $V_{q\bar{q}}H$ searches are less sensitive to the individual components of the JES. They use a strongly reduced set of JES uncertainties that is described by three grouped nuisance parameters and a nuisance parameter for the eta-intercalibration nonclosure [104]. This set is a further reduction, combining effects across categories as well. The four strongly reduced nuisance parameters are treated as correlated between the $Z_{\ell\bar{\ell}}H$ and $V_{q\bar{q}}H$ searches. The eta-intercalibration nonclosure nuisance parameter is present in both reduction schemes and is thus correlated between all channels. There is no clear correspondence between the remaining individual nuisance parameters of both schemes. Hence, no correlation between the grouped nuisance parameters in the strong and the nuisance parameters in the category based JES reduction schemes is implemented.

The $Z_{\ell\bar{\ell}}H$ and VBF searches implement an uncertainty on the JVT discriminant [103] and the corresponding nuisance parameter is correlated.

The systematic uncertainties on jets with a radius parameter of $R = 1.0$ present in the $V_{q\bar{q}}H$ search have no counterparts in the VBF and $Z_{\ell\bar{\ell}}H$ searches that use only R = 0.4 jets and are therefore not correlated.

- The systematic uncertainties on the b-tagging efficiencies [114] are partly correlated. The $V_{q\bar{q}}H$ search explicitly uses information on the jet flavour to improve the sensitivity. Here, the b-tagging uncertainties for b, c, as well as *light* jets are each split into several eigenvectors ordered by impact. By contrast, flavour information plays a minor role in the $Z_{\ell\bar{\ell}}H$ search and the corresponding uncertainties are represented by one single combined nuisance parameter for each of the three categories of b, c, and *light* jets. Since the nuisance parameters in the $Z_{\ell\bar{\ell}}H$ search strictly correspond to a combination of individual eigenvectors in the $V_{q\bar{q}}H$ search, the leading nuisance parameter for each of the three categories from the $V_{q\bar{q}}H$ search is correlated with the corresponding combined nuisance parameter from the $Z_{\ell\bar{\ell}}H$ search. The VBF search is flavour-inclusive and thus no uncertainties related to b-tagging apply.

- The systematic uncertainties related to the reconstruction of the soft $E_{\mathrm{T}}^{\mathrm{miss}}$ components from tracks originating from the primary vertex and not associated to physics objects are correlated. These include uncertainties on the scale of soft components, and the resolutions of the soft components parallel and perpendicular to the $E_{\mathrm{T}}^{\mathrm{miss}}$ direction [114].

- The pile-up profile in the detector is estimated using MC simulations and the corresponding systematic uncertainty is correlated across all input searches.

Some sources of systematic uncertainty are strongly constrained in the $V_{q\bar{q}}H$ search that uses CRs with large numbers of data events. Here, the criteria outlined above for not correlating these are met. Those nuisance parameters are indicated by an asterisk ($\star$) in Table 6.1. Since their strong constraint originates from the $V_{q\bar{q}}H$ search, they are uncorrelated between the $V_{q\bar{q}}H$ and the other two searches, but are correlated between the VBF and $Z_{\ell\bar{\ell}}H$ searches.

Source	VBF	$Z_{\ell\bar{\ell}}H$	$V_{q\bar{q}}H$
Luminosity	✓	✓	✓
Muon trigger efficiency statistical	✓	✓	—
Muon trigger efficiency systematic	✓	✓	—
Muon isolation efficiency statistical	✓	✓	—
Muon isolation efficiency systematic	✓	✓	✓
Muon reconstruction efficiency statistical	✓	✓	✓
Muon reconstruction efficiency systematics	✓	✓	✓
Muon track to vertex association eff. statistical	✓	✓	✓
Muon track to vertex association eff. systematic	✓	✓	✓
Muon track smearing in inner detector	✓	✓	—
Muon track smearing in muon system	✓	✓	—
Muon momentum scale	✓	✓	—
Muon momentum scale charge dependent	✓	✓	—
Muon momentum scale charge dependent residual	✓	✓	—
Electron trigger efficiency	✓	✓	✓
Electron isolation efficiency	✓	✓	✓
Electron identification efficiency	✓	✓	✓
Electron reconstruction efficiency	✓	✓	✓
Electron energy resolution	✓	✓	✓
Electron energy scale	✓	✓	✓
Jet energy resolution	✓	✓	✓, $\star$
Jet eta-intercalibration nonclosure	✓	✓	✓
Jet energy scale strong reduction first	—	✓	✓, $\star$
Jet energy scale strong reduction second	—	✓	✓
Jet energy scale strong reduction third	—	✓	✓
Jet vertex tagging efficiency	✓	✓	—
Flavour tagging b systematics	—	✓	✓, $\star$
Flavour tagging c systematics	—	✓	✓
Flavour tagging $light$ systematics	—	✓	✓
Flavour tagging extrapolations for b	—	✓	✓
Flavour tagging extrapolations for c	—	✓	✓
$E_{\mathrm{T}}^{\mathrm{miss}}$ soft term resolution parallel	✓	✓	✓, $\star$
$E_{\mathrm{T}}^{\mathrm{miss}}$ soft term resolution perpendicular	✓	✓	✓
$E_{\mathrm{T}}^{\mathrm{miss}}$ soft term track momentum scale	✓	✓	✓, $\star$
Pile-up reweighting	✓	✓	✓
QCD scale variation (signal cross section)	–	✓	✓
PDF set choice (signal cross section)	✓	✓	✓

Table 6.1.: Summary of experimental and theoretical sources of systematic uncertainty and their correlation between the individual searches. A ✓ indicates that a given nuisance parameter is considered in the correlation model, while a dash indicates that a given nuisance parameter was either pruned or does not apply to the search. Nuisance parameter marked with an asterisk ($\star$) are over-constrained and are not correlated, see details in the text.

Theoretical Uncertainties

The sources of systematic theory uncertainty on the signal predictions, and the correlations between those implemented into the correlation model are described in the following. Generally, there is different level of detail in the parameterisation of the effect of theory uncertainties in the individual searches:

- The $V_{q\bar{q}}H$ search estimates the systematic uncertainty due to variations of the QCD renormalisation and factorisation scales, as well as due to the choice of a specific PDF set separately for the signal cross section, acceptance, and $E_{\mathrm{T}}^{\mathrm{miss}}$ distribution shape. These are represented by individual nuisance parameters.

- The $Z_{\ell\bar{\ell}}H$ search takes into account the systematic uncertainty on the signal cross section due to the choice of QCD scales and PDF set. Each of the two effects is represented by a corresponding nuisance parameter.

- The VBF search studies the effect of both choices on the signal cross section similarly to the $Z_{\ell\bar{\ell}}H$ search. However, *one common* nuisance parameter is employed representing the *combined* effect of QCD scale variations and of the veto of events with a third jet on the signal prediction. Hence, the disentanglement of the two effects for a correlation of the uncertainty due to QCD scale variation with other searches is impossible.

The uncertainties due to choice of a PDF set on the signal cross section are correlated across all input searches since they are consistently represented by the same nuisance parameter. The production of the Higgs boson via VBF has a different Feynman diagram than the Higgsstrahlung ($Z_{\ell\bar{\ell}}H$ and $V_{q\bar{q}}H$). The variations of QCD scales are studied to estimate the impact of higher order diagrams. These uncertainties are not correlated between searches for VBF and Higgsstrahlung final states, since those higher order diagrams will in general be different. Different nuisance parameters are preserved for the VBF and Higgsstrahlung production modes in the combined likelihood model. Because of the different diagrams and the combined effect considered by the VBF search, only uncertainties on the signal cross section due to QCD scale variations in the $Z_{\ell\bar{\ell}}H$ and $V_{q\bar{q}}H$ searches are correlated.

The modelling of the parton shower gives rise to an additional source of systematic uncertainty. The generators employ different theoretical approaches for the description of the non-perturbative hadronisation process behind the parton showering.

- The parton showering induced systematic uncertainty on the signal in the $V_{q\bar{q}}H$ search is estimated by variations in the tune parameters of the PYTHIA generator (MPI, Ren, Var1, Var2) [116, 117]. The uncertainty is represented as separate nuisance parameters for the effects on the signal cross section and acceptance.

- The VBF search studies the same variations in PYTHIA, but additionally estimates an uncertainty due to modelling differences between the PYTHIA and HERWIG generators. Both effects are combined into a single nuisance parameter which is dominated by the difference between the generators.

- The corresponding uncertainty in the $Z_{\ell\bar{\ell}}H$ search was found to have a negligible impact on the individual result. It was therefore pruned away in the input search.

Due to the different determination methods and the large impact of the generator differences in VBF, a full correlation of parton shower uncertainties is not justified. The parton shower uncertainties on the signal prediction of the VBF and $V_{q\bar{q}}H$ searches are therefore not correlated.

6.1.2. Run 1+2 Combination

The Run 2 combination of searches for invisible decays of the Higgs boson is further combined with the combined result of all ATLAS Run 1 searches [3]. The inputs to this combination are the combined search from Run 1, and the combination of Run 2 searches employing the correlation scheme discussed above. The correlation assumptions between the Run 1 and 2 combinations are described in the following.

Experimental Uncertainties

The correlations between Run 1 and 2 for the experimental uncertainties related to lepton identification, flavour tagging, and $E_{\mathrm{T}}^{\mathrm{miss}}$ reconstruction are assumed to be negligible. This is due to the changes in the detector layout, in particular the inclusion of the Inner-B-Layer (IBL), in the detector conditions like the calorimeter gain settings, in the reconstruction algorithms and their calibrations, in the discrimination variables and the choice of the operating points. Those changes in reconstructions and calibrations propagate to the estimation methods and parameterisations of systematic uncertainties as nuisance parameters. Hence, full correlation between these uncertainties is not taken into account. The uncertainty on the integrated luminosity is determined independently for the different data-taking periods and is thus not correlated.

Recommendations exist for the correlation of JES uncertainties given the full list of nuisance parameters in both runs. A *weak* correlation model and a *strong* correlation model are proposed. The weak correlation scheme includes no correlations between JES uncertainties. The strong correlation scheme assumes full correlation between nuisance parameters describing systematic and modelling effects. In both combinations, searches employ different reduction schemes for uncertainties on the JES. Moreover, theses schemes have changed between the runs. The proposed strong correlation model is implemented by only correlating those parameters that are modelled in both runs. This corresponds to nuisance parameters from the category based reduction in the Run 2 VBF search. In Run 1, these nuisance parameters are either already correlated between inputs, or originate from a specific search. Combined likelihood models are constructed using both scenarios and the strong correlation model is chosen for the combination of Run 1+2 searches due to the resulting slightly weaker and hence more conservative limit on $\mathcal{B}_{H\to\mathrm{inv}}$, see Appendix B for details. The systematic uncertainty on the jet energy resolution (JER) is over-constrained in the Run 1 combination, and the criterion outlined above for not correlating the nuisance parameters between Run 1 and 2 is met. The uncertainty is kept correlated between the Run 2 $Z_{\ell\bar{\ell}}H$ and VBF searches. The correlated nuisance parameters between Run 1 and 2 are summarised in Table 6.2.

Source	Run 1	Run 2
Modelling of eta-intercalibration	correlated	VBF
Statistics of eta-intercalibration	$V_{q\bar{q}}H$	VBF
Pile-up corrections, three individual nuisance parameters	$V_{q\bar{q}}H$	VBF
Pile-up corrections	Monojet	VBF
Calorimeter response to different jet flavours	correlated	VBF
Uncertainty due to flavour composition of jets	correlated	VBF
JES specific for b-quark jets	$V_{q\bar{q}}H$	VBF
Leading combined modelling effects	correlated	VBF
Sub-leading combined modelling effects	Monojet	VBF
Leading combined detector effects	Monojet	VBF
QCD scale variation on the signal cross section	$Z_{\ell\bar{\ell}}H$	$Z_{\ell\bar{\ell}}H$ + $V_{q\bar{q}}H$
QCD scale variation on diboson prediction	$Z_{\ell\bar{\ell}}H$	$Z_{\ell\bar{\ell}}H$
Parton shower modelling on signal acceptance	$V_{q\bar{q}}H$	$V_{q\bar{q}}H$
Fraction of ggF+2jets events in the signal region	VBF	VBF

Table 6.2.: Summary of sources of systematic uncertainty that are correlated in the total combination of the input Run 1 and Run 2 combinations. Nuisance parameters are either correlated parameters from several input searches, labelled as *correlated*, or originate from a specific search, labelled as such.

Theoretical Uncertainties

Searches in the same final state but in different runs estimate some sources of theoretical uncertainty by employing analogous techniques. In such cases a correlation is adopted in the combined likelihood model. A full correlation is not justified for the remaining theory nuisance parameters. The theoretical uncertainties that are correlated between runs are discussed in the following, and summarised in Table 6.2.

- Different sets of **PDFs** are used in Run 1 and 2 for the nominal signal prediction, as well as to assess the systematic uncertainty arising due to these choices. Hence, a full correlation of these systematic uncertainties across runs is not implemented in the combination.

- The impact of the **parton shower modelling** on the signal cross section is assessed by the Run 1 VBF search using different schemes of the SHERPA MC generator, and by the Run 2 VBF search using different PYTHIA tunes combined with a comparison to HERWIG. A full correlation is thus not assumed. Contrarily, both $V_{q\bar{q}}H$ searches consider the effect of parton shower modelling on the signal acceptance comparing PYTHIA tunes and the uncertainty is treated as correlated.

- The systematic uncertainty due to the variation of **QCD scales** on the $V_{q\bar{q}}H$ signal in Run 1 is split into impacts on $gg \to ZH$ and $qq \to VH$. There are no counterparts in Run 2 that could be correlated as these are split into effects on cross section, acceptance and $E_{\mathrm{T}}^{\mathrm{miss}}$ shape.

The Run 1 $Z_{\ell\bar{\ell}}H$ search estimates the systematic uncertainty due to QCD scale variations on the signal cross section similarly to the Run 2 searches. These systematic uncertainties are thus correlated between runs.

The QCD scale variation induced systematic uncertainty on the prediction for background processes involving two vector bosons (diboson) in the $Z_{\ell\bar{\ell}}H$ searches is correlated.

- The effect of QCD scale variations on the ggF+2jet yield in the VBF SR is estimated in both runs by using the same method. The nuisance parameters are thus correlated.

6.2. Results for Run 2

In the following, the results of the combination of searches for invisible decays of the Higgs boson in the VBF, $Z_{\ell\bar{\ell}}H$ and $V_{q\bar{q}}H$ topologies using $36\,\text{fb}^{-1}$ of pp collision data taken by the ATLAS experiment in 2015+2016 are presented. The statistical combination is performed on the level of individual likelihood functions as described in Section 4.1.3 and adopts the model for correlations between sources of systematic uncertainties discussed in Section 6.1.1.

6.2.1. Scans of the Likelihood Functions

The expected and observed profile likelihood ratios of the input searches and the combination as a function of the invisible branching fraction $\mathcal{B}_{H\to\text{inv}}$ are shown in Figure 6.1. Post-fit Asimov data sets as introduced in Section 4.1.1 are used to obtain the expected

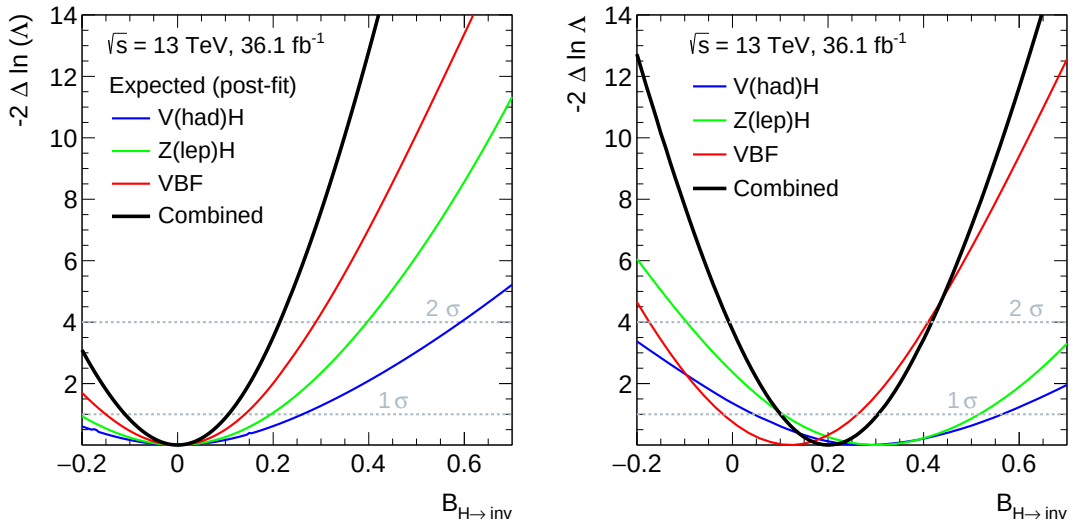

Figure 6.1.: The expected (left) and observed (right) profile likelihood ratios for the combination of all searches in Run 2 compared to the results in the individual searches as a function of $\mathcal{B}_{H\to\text{inv}}$.

profile likelihood ratios. A post-fit Asimov data set represents the SM prediction via construction with nuisance parameter values retrieved from a profile likelihood fit with the invisible branching fraction fixed to zero (post-fit values). The post-fit values are used instead of the pre-fit values to accommodate the constraints of the phase-spaces being probed by the searches. The phase-space will generally be distinct from the one used to obtain the constraining priors. The resulting post-fit Asimov data set thereby more closely resembles the SM expectation relevant to the observed data set, hence it is used as well for the calculation of the expected limit on the invisible branching fraction. The expected profile likelihood ratios are found found to be smooth in $\mathcal{B}_{H\to\text{inv}}$. This shows that there are no significant irregularities or biases in the individual or combined likelihood models arising from a specific analysis region or nuisance parameter. Furthermore, they are centred around the best-fit value of $\mathcal{B}_{H\to\text{inv}} = 0$ as expected from the underlying prediction. The width of the curves represent the size of the total uncertainty on the expected result and thereby quantify the sensitivities of the searches. The $V_{q\bar{q}}H$ search has the lowest sensitivity, and the VBF search features the highest sensitivity. The $Z_{\ell\bar{\ell}}H$ search sensitivity is found in between, as anticipated from the individual results. The VBF search is found to contribute most to the combined expected profile likelihood ratio. The profile likelihood ratio shows the improvement due to combination of different measurements by a more steeply rising parabola.

The observed profile likelihood ratios are constructed using the observed data sets of the searches, respectively of the combination. They are found to be smooth in $\mathcal{B}_{H\to\text{inv}}$. The observed sensitivities are quantified by their widths. The best-fit value at the minimum of the profile likelihood represents the most probable value for the invisible branching fraction in the respective input search. The excesses of events above SM expectation observed in all three input searches lead to the finite, positive most probable values. The most probable value of the combined likelihood is found between the individual minima as a result of summing the excesses in the input searches, weighted by their individual sensitivities. It lies above the minimum of the VBF curve which has the largest contribution. The combined observed profile likelihood features a larger upward slope compared to the individual curves alone, consistent with the combination of the inputs driven by the VBF search.

6.2.2. Limit on the Invisible Branching Fraction

The upper limits on the invisible branching fraction of the Higgs boson $\mathcal{B}_{H\to\text{inv}}$ are computed with the CL_S technique, see also Section 4.1.2. The combined observed (expected $^{+1\,\sigma}_{-1\,\sigma}$) upper limit at 95% confidence level is given by:

$$\mathcal{B}_{H\to\text{inv}} < 0.38\ (0.21\,^{+\,0.08}_{-\,0.06})\,,$$

and is graphically represented together with the results of the input searches in Figure 6.2. A summary of the numerical values for the upper limits and best-fit values of $\mathcal{B}_{H\to\text{inv}}$ together with the significances and corresponding p-values for a result at least as extreme as the observed result are given in Table 6.3.

The experimental sensitivity is given by the expected upper exclusion limit and its uncertainty bands. It is found to increase from the most sensitive VBF input search alone

$(0.28^{+0.11}_{-0.08})$ to a combined result of $(0.21^{+0.08}_{-0.06})$. This is due to the addition of information from searches in the $Z_{\ell\bar{\ell}}H$ and $V_{q\bar{q}}H$ topologies, and anticipated from the expected profile likelihood ratios.

The individual excesses of events observed over the SM expectation in all three inputs searches have to be taken into account for the observed upper exclusion limit. The combined best-fit value, together with the steep combined profile likelihood parabola results in a slightly weaker combined observed upper limit compared to the VBF search alone. The summation of weighted individual excesses in all Run 2 searches together with the stronger experimental sensitivity results in a more pronounced tension between the combined expected and observed results. This behaviour is anticipated when combining excesses in several searches irrespective of whether the excesses originate from the existence of a signal, or from background fluctuations. The observed significances of the input searches range from 0.86σ to 1.54σ, whereas the combined observed significance is 1.93 standard deviations.

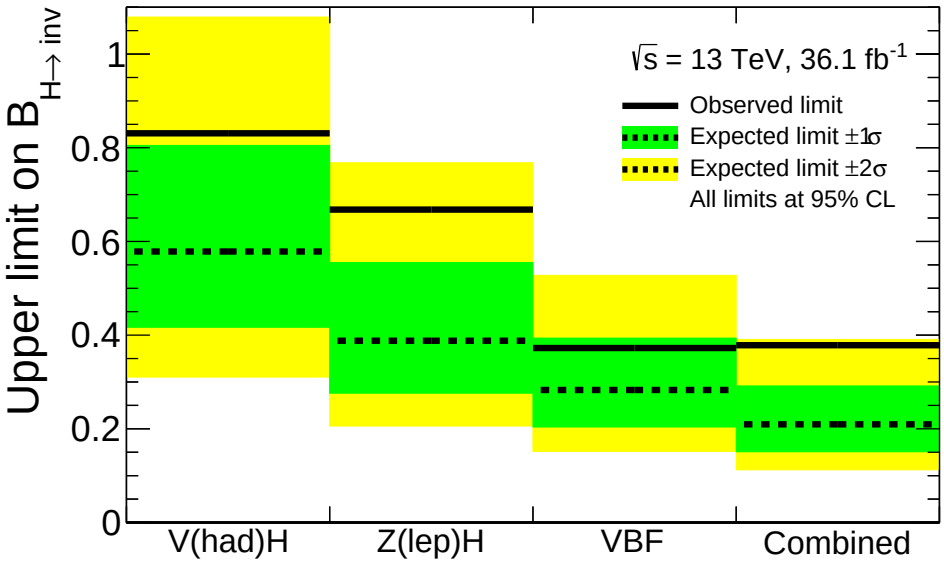

Figure 6.2.: The observed and expected upper CL_S exclusion limits on $\mathcal{B}_{H\to\text{inv}}$ at 95% CL for the combination of all channels in Run 2 compared to the results in the individual searches.

6.2.3. Ranking of Systematic Uncertainties

The nuisance parameters can be ranked according to their post-fit impact on the profiled value of the invisible branching fraction. Systematic uncertainties with a high impact on the result of one or more inputs are expected to have a large impact on the combined result as well. This impact is evaluated by a first fit of the combined profile likelihood to the observed data set to estimate the post-fit uncertainties on these parameters. Subsequently, two further fits are performed holding constant a specific nuisance parameter

Table 6.3.: The observed (expected $^{+1\,\sigma}_{-1\,\sigma}$) upper CL_S exclusion limits on $\mathcal{B}_{H\to\text{inv}}$ at 95% confidence level for the combination of all searches in Run 2 compared to the results in the individual searches with the corresponding significances, p-values and the most probable values for the invisible branching fraction (profiled $\mathcal{B}_{H\to\text{inv}}$).

Analysis	Exclusion limit	Significance	p-value	profiled $\mathcal{B}_{H\to\text{inv}}$	Ref.
Run 2 VBF	0.37 ($0.28^{+0.11}_{-0.08}$)	$0.86\,\sigma$	0.194	0.121 ± 0.135	[4]
Run 2 ZH	0.67 ($0.39^{+0.17}_{-0.11}$)	$1.54\,\sigma$	0.062	0.302 ± 0.204	[5]
Run 2 VH	0.83 ($0.58^{+0.23}_{-0.16}$)	$1.16\,\sigma$	0.122	0.281 ± 0.263	[6]
Run 2 combination	0.38 ($0.21^{+0.08}_{-0.06}$)	$1.93\,\sigma$	0.027	0.201 ± 0.103	[12]

at its positive and negative post-fit uncertainty values. The resulting discrepancy in the invisible branching fraction between these fits and the first, where all nuisance parameters are profiled, is used to estimate the effect of the NP at extremal values $\Delta\mathcal{B}_{H\to\text{inv}}$. This procedure is iterated for all nuisance parameters. Nuisance parameters are ordered by their summed effects at positive and negative variation. The ranking of nuisance parameters in the combination is shown in Figure 6.3, including the free background normalisations estimated in CRs which have no constraining prior. Further depicted are the profiled values and post-fit uncertainties of the nuisance parameters from the fit profiling all parameters. The yellow bands indicate the pre-fit effect of the nuisance parameters on the invisible branching fraction estimated from a similar procedure holding the parameters in fits constant at their pre-fit uncertainty values obtained from the prior constraints. The uncertainties due to the finite size of MC samples in the different analysis are binned for every process separately. The MC statistics depicted in the ranking each represent the nuisance parameter for a specific bin. The sources of systematic uncertainties are labelled with the originating input search, or labelled *correlated* if they are correlated between several inputs.

The ranking of the nuisance parameters is found to be consistent with the rankings obtained from the individual input searches, which are shown in Appendix D together with details on the profiled values. The general findings of the ranking comparison are:

- The absolute impact of these nuisance parameters on the combined invisible branching fraction is found to be reasonably well described by the absolute impact in the specific search alone weighted by the sensitivity that the input search adds to the combination. Parameters from the VBF search hence are found to have roughly the same absolute impact in the VBF search and in the combination. On the other hand, parameters from the $Z_{\ell\bar{\ell}}H$ and even more so from the $V_{q\bar{q}}H$ search are found to affect the combined branching fraction significantly less compared to their impact in the individual searches.

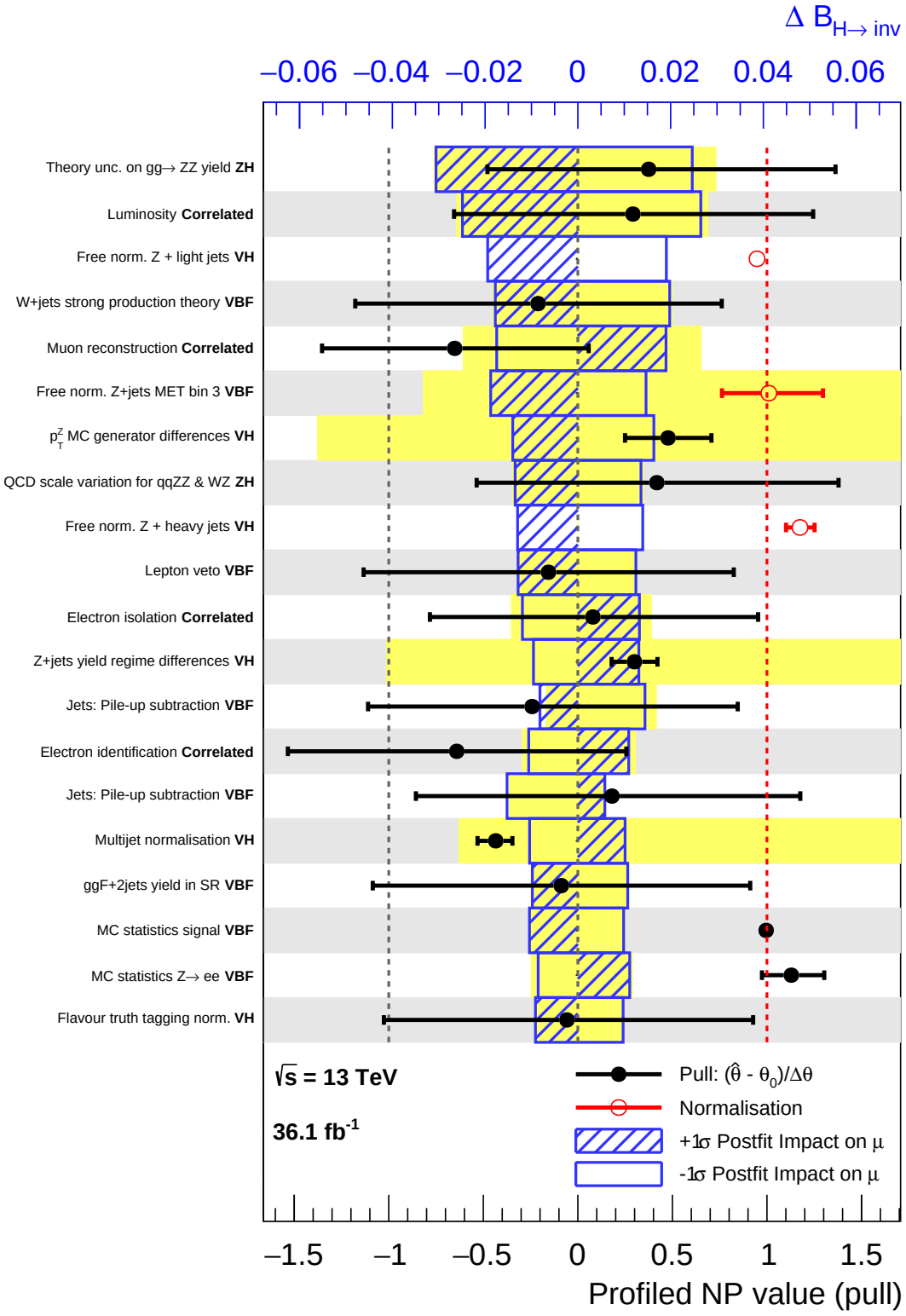

Figure 6.3.: The profiled values of nuisance parameters for the combination of the Run 2 searches, ranked according to their post-fit impact on $\mathcal{B}_{H\to\text{inv}}$. Free normalisation parameters shown in red and MC statistic parameters have their nominal value of unity, indicated by the vertical red dashed line.

- Nuisance parameters that are correlated between different searches are found to have an impact on the combined result that is driven by the more sensitive searches between which the nuisance parameters are correlated.

- Uncertainties due to the finite size of the MC samples in the VBF search are present in the combined ranking. These are expected since the VBF search is found to be partly limited by the available MC statistics, especially in regions of very high d-jet mass. Accordingly, these are also found in the ranking of the VBF search alone.

The absolute impact on the combined invisible branching fraction as sensitivity weighted impact in the inputs for uncorrelated and correlated sources of systematic uncertainty is exemplified in the following:

- The systematic uncertainty on the gluon-gluon initiated ZZ yield in the $Z_{\ell\bar{\ell}}H$ search from theory calculations is ranked highest. The process where one of the Z decays to electrons or muons and the other invisibly to neutrinos is the irreducible main background in this analysis. A variation of the prediction for this process thus has a significant impact on the result of the search in the $Z_{\ell\bar{\ell}}H$ topology. Its absolute impact in the combination is considerably reduced but still large.

- The impact of correlated sources of systematic uncertainty, such as the integrated luminosity and the muon reconstruction efficiency, are consistent with the impact of these sources in the VBF and $Z_{\ell\bar{\ell}}H$ searches. This is due to these inputs contributing most to the combined result.

- The free normalisation factor for the Z + light jets prediction in the $V_{q\bar{q}}H$ search is ranked high in the combination. The process with $Z \to \nu\nu$ and where the mass of the di-jet system or large-R jet is compatible with the W/Z boson mass is a major background in this search. The absolute impact of the corresponding parameter on the invisible branching fraction in the $V_{q\bar{q}}H$ search is very large. Hence, the impact on the combined invisible branching fraction is still significant, although its absolute value is strongly reduced because of the low sensitivity of the $V_{q\bar{q}}H$ search.

- The theory uncertainty on the strong and weak production of V+jets in the VBF search is divided in $E_{\mathrm{T}}^{\mathrm{miss}}$ bins, separately for the variation of different scales used in the computation. The uncertainty with the fourth largest impact of the combined result is such a variation in the highest and most sensitive $E_{\mathrm{T}}^{\mathrm{miss}}$ bin of the VBF search for the strong production of W+jets. The process where the W boson decays leptonically, and the charged lepton is not reconstructed constitutes one of the dominant backgrounds in this search. A variation of the prediction therefore has a considerable impact on the result. The uncertainty affects the invisible branching fraction in the combination nearly as much as in the VBF search alone, which is expected from the large contribution of the VBF search. This mechanism is also observed for the Z+jets background normalisation factor for the highest $E_{\mathrm{T}}^{\mathrm{miss}}$ bin of the VBF search.

6.2.4. Breakdown of Systematic Uncertainties

The impact of different categories of systematic uncertainty on the sensitivity of the combination is shown in Table 6.4. Details on the categorisation are given in Appendix C. The evaluation is performed on an expected post-fit Asimov data set constructed with $\mathcal{B}_{H\to\text{inv}} = 0$ to estimate the effect on the sensitivity only and prevent effects due to observed excesses. A specific category is taken out of consideration by setting the corresponding nuisance parameters constant to their post-fit values obtained in the generation of the Asimov data set. The uncertainty on the most probable invisible branching fraction resulting from a fit to the expected Asimov data set is quadratically subtracted from the total uncertainty that considers all systematic uncertainties.

The quadratic difference is stated as an *estimate* for the impact of a specific group of systematic uncertainties, since e.g. residual correlations between groups are neglected. Likewise, no full closure is expected from the quadratic addition of contributions from different groups of systematic uncertainty. The contribution of limited data statistics is obtained by ignoring all sources of systematic uncertainty. The combined effect of all systematic uncertainties is accordingly estimated by the quadratic difference between total uncertainty and the contribution of limited data statistics.

The observed impact of different groups of systematic uncertainty is summarised in the following.

- Large contributions are observed for the categories describing the detection of electrons and muons, as well as the reconstruction of jets. All three are key objects to all input searches. Reconstructed leptons are also used in the VBF and $V_{q\bar{q}}H$ searches in CRs to estimate background contributions, and in SRs to identify and discard events containing these. Charged leptons and jets with their uncertainties are further utilised for the hard term of the $E_{\text{T}}^{\text{miss}}$.

- The V+jets process as main background to the most sensitive VBF search, and also significant for the $V_{q\bar{q}}H$ search, is estimated as individual group. The modelling of other backgrounds such as diboson, top and top-antitop production and QCD induced processes involving multiple jets (multijet) is summarised in a second group. Both categories are found to have a considerable impact on the result given the importance of precise background predictions in searches with essentially zero signal prediction.

- The impact of the limited statistics of MC predictions is significant for the dominant VBF search as discussed for the ranking of systematic uncertainties in Section 6.2.3. This effect propagates to the combination and a large effect of the corresponding category is found.

- The modelling of the signal process for the expected sensitivity is found to be very small. This is due to the expected Asimov data set this study is based on, which contains no invisibly decaying Higgs boson signal.

- Flavour tagging information is used considerably only by the least sensitive VH search. The effect on the combined result is thus found to be small.

Group	Contribution		
Luminosity	+ 0.021	- 0.016	± 0.019
Leptons	+ 0.050	- 0.053	± 0.051
Jets	+ 0.037	- 0.042	± 0.040
Flavour tagging	+ 0.008	- 0.009	± 0.009
$E_{\mathrm{T}}^{\mathrm{miss}}$ soft term	+ 0.009	- 0.009	± 0.009
V+jets modelling	+ 0.037	- 0.037	± 0.037
Other backgr. modelling	+ 0.046	- 0.053	± 0.050
Signal modelling	+ 0.009	- 0.009	± 0.009
MC statistics	+ 0.043	- 0.047	± 0.045
All experimental	+ 0.072	- 0.076	± 0.074
All theory	+ 0.053	- 0.058	± 0.055
Theory and experimental	+ 0.087	- 0.092	± 0.090
All systematics	+ 0.095	- 0.099	± 0.097
Data statistics	+ 0.048	- 0.048	± 0.048
Total uncertainty	+ 0.106	- 0.110	± 0.108

Table 6.4.: The impact of different categories of systematic uncertainty on the profiled $\mathcal{B}_{H\to\mathrm{inv}}$ in the Run 2 combination estimated with fits to an Asimov data set with $\mathcal{B}_{H\to\mathrm{inv}} = 0$. The experimental uncertainty and the uncertainty related to the size of the MC sample are treated as separate categories.

These effects can additionally be studied by the variation of the combined expected upper limit on $\mathcal{B}_{H\to\mathrm{inv}}$. The procedure is analogous, but the expected limit is re-computed and subtracted from the nominal expected limit. The ordering of the groups by impact on the expected limit is found consistent to the ordering by impact on the uncertainty on the profiled invisible branching ratio. Details can be found in Appendix C.

6.3. Results for Run 1+2

In the following, the results of the statistical combination of Run 2 (using 2015+2016 data) [4–6] and Run 1 [3] searches for invisible decays of the Higgs boson are presented. The correlations between the sources of systematic uncertainty between Run 1 and 2 is described in Section 6.1.2.

6.3.1. Scans of the Likelihood Functions

The expected and observed profile likelihood ratios are shown for the individual combinations and the combination of Run 1+2 in Figure 6.4. The expected profile likelihood ratios are constructed using a post-fit Asimov data set, produced via enforcing $\mathcal{B}_{H\to\mathrm{inv}} = 0$. The combined observed data sets are used for the observed profile likelihood ratios. Given their similar sensitivities, the Run 2 and Run 1 results contribute accordingly to both the expected and observed total profile likelihood ratios. The Run 2 result has a slightly

stronger contribution as anticipated from the steeper parabola. In contrast to the discussed Run 2 results, the Run 1 searches observed deficits of events compared to the SM predictions resulting in a slightly negative best-fit value for the invisible branching fraction in the Run 1 combination. Hence, the combination of both runs shows a most probable value at $\mathcal{B}_{H\to\text{inv}} = 0.126$, which is consistent with the mechanism of a weighted average between both inputs at $\mathcal{B}_{H\to\text{inv}} = -0.023$ and $\mathcal{B}_{H\to\text{inv}} = 0.201$.

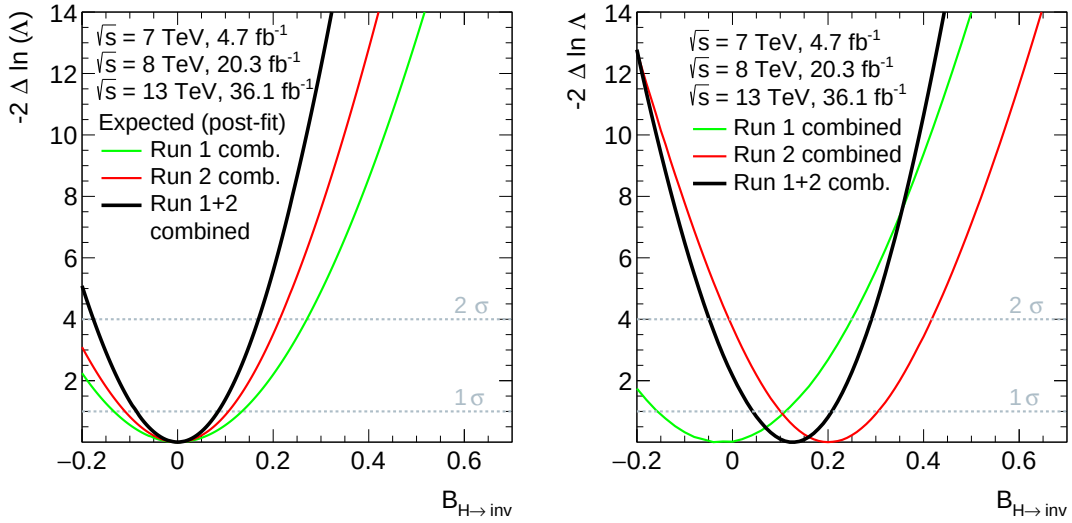

Figure 6.4.: The expected (left) and observed (right) profile likelihood ratios for the combination of Run 1 and Run 2 searches compared to the results of the individual combination as a function of $\mathcal{B}_{H\to\text{inv}}$.

6.3.2. Limit on the Invisible Branching Fraction

The upper exclusion limits are calculated using the CL_S technique that is described in Section 4.1.2. The observed (expected $^{+1\,\sigma}_{-1\,\sigma}$) upper exclusion limit at 95% confidence level for the combination of Run 1+2 searches is given by

$$\mathcal{B}_{H\to\text{inv}} < 0.26\ (0.17^{+0.07}_{-0.05})\,,$$

and is graphically represented together with the input results in Fig. 6.5. A summary of the resulting numerical values for all Run 2 input searches, the Run 1 combination and the combinations studied in this Thesis are given in Table 6.5.

The expected upper exclusion limit on the invisible branching fraction of the Higgs boson for the combined Run 2 searches is $(0.21^{+0.08}_{-0.06})$. The combination with the statistically independent searches with Run 1 data increases the sensitivity as can be seen in the expected upper limit of $(0.17^{+0.07}_{-0.05})$. This is consistent with the shrinkage of the width for the expected profile likelihood ratios found for the combination of both runs compared to results of individual runs as shown in Figure 6.4.

The individual most probable values for the invisible branching fraction and their weighted combination to the minimum of the combined observed profile likelihood ratio have to be considered for the observed limit of the combination in analogy to the

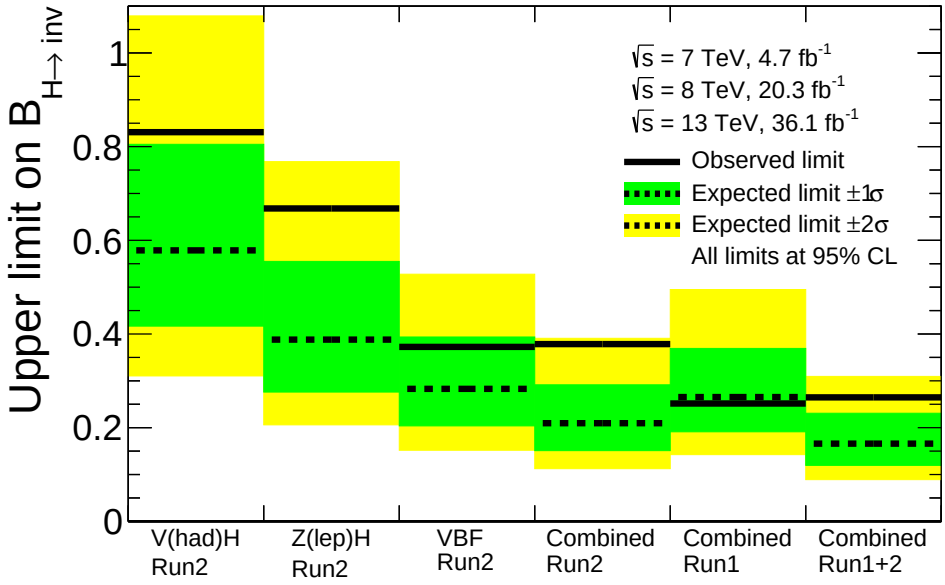

Figure 6.5.: The observed and expected upper limits on $\mathcal{B}_{H\to\text{inv}}$ at 95% CL for the combination of Run 1 and Run 2 compared to the results of the individual Run 1 and Run 2 combinations and the individual searches in Run 2.

Table 6.5.: The observed (expected$^{+1\sigma}_{-1\sigma}$) upper CL_S exclusion limits on $\mathcal{B}_{H\to\text{inv}}$ at 95% CL for the combination of all searches in Run 2 compared to the results of the individual analyses.

Analysis	Exclusion limit	Significance	p-value	profiled $\mathcal{B}_{H\to\text{inv}}$	Ref.
Run 2 VBF	$0.37\ (0.28^{+0.11}_{-0.08})$	$0.86\,\sigma$	0.194	0.121 ± 0.135	[4]
Run 2 ZH	$0.67\ (0.39^{+0.17}_{-0.11})$	$1.54\,\sigma$	0.062	0.302 ± 0.204	[5]
Run 2 VH	$0.83\ (0.58^{+0.23}_{-0.16})$	$1.16\,\sigma$	0.122	0.281 ± 0.263	[6]
Run 2 combination	$0.38\ (0.21^{+0.08}_{-0.06})$	$1.93\,\sigma$	0.027	0.201 ± 0.103	[12]
Run 1 combination	$0.25\ (0.27^{+0.10}_{-0.08})$	—	—	-0.023 ± 0.134	[3]
Run 1+2 combination	$0.26\ (0.17^{+0.07}_{-0.05})$	$1.47\,\sigma$	0.071	0.126 ± 0.083	[12]

Run 2 result. Here, the deficits of events observed in the Run 1 searches are combined with the excesses in the Run 2 searches. In conjunction with the steep observed likelihood parabola corresponding to the increase in sensitivity, this leads to an observed upper limit for the combination only slightly weaker than the the Run 1 result. In addition, the improvement due to combination is found to be stronger for the observed compared to the expected exclusion limits. This can be explained by the inclusion of the slight deficits in observed events in the Run 1 searches. Accordingly, the tension between the expected and observed results in turn relaxes from 1.93σ for the Run 2 combination to 1.47σ for the full combination of Run 1 and 2 searches.

6.3.3. Ranking of Systematic Uncertainties

The ranking of nuisance parameters according to their post-fit impact on the profiled invisible branching fraction if evaluated using the same technique discussed for the ranking in the Run 2 combination in Section 6.2.3 and is shown for the combination of Run 1+2 in Figure 6.6. The mechanism behind the impact of Run 2 nuisance parameters only is consistent with the ranking in the Run 2 combination. The absolute impact of nuisance parameters from separate runs on the profiled branching fraction in the Run 1+2 combination compared to their impact to the individual results is reduced following the relative contribution of the inputs to the full combination. However, the ordering is not expected to be precisely the same, since different highly ranked nuisance parameters have already similar absolute impacts on the individual Run 1 and Run 2 combination results.

Highly ranked uncertainties in the Run 1+2 combination from the Run 1 searches include:

- The highest ranked parton showering uncertainty describes the effect on the W+jets and Z+jets prediction in Run 1 which was correlated between the VBF and Mono-jet analyses. Both are major backgrounds to the searches. The nuisance parameter has a high impact on the Run 1 and Run 1+2 invisible branching fractions, since the VBF+Mono-jet search contributes most to the sensitivity of the Run 1 result.

- The free normalisation factors for the V+jets background in the two m_{jj} bins of the Run 1 Mono-jet analysis are highly ranked in Run 1 as well as in the Run 1+2 because the V+jets process constitutes the main background to the search. The signal sensitivity is rising with m_{jj} due to the decreasing backgrounds in this regime. Thus, the normalisation in the higher m_{jj} bin has a stronger impact on the invisible branching fraction.

- The uncertainty on the strongly produced W/Z+jets background yields in the Run 1 VBF search due to variation of the QCD scales directly impact the sensitivity, which is consistent with the high ranking of the nuisance parameter.

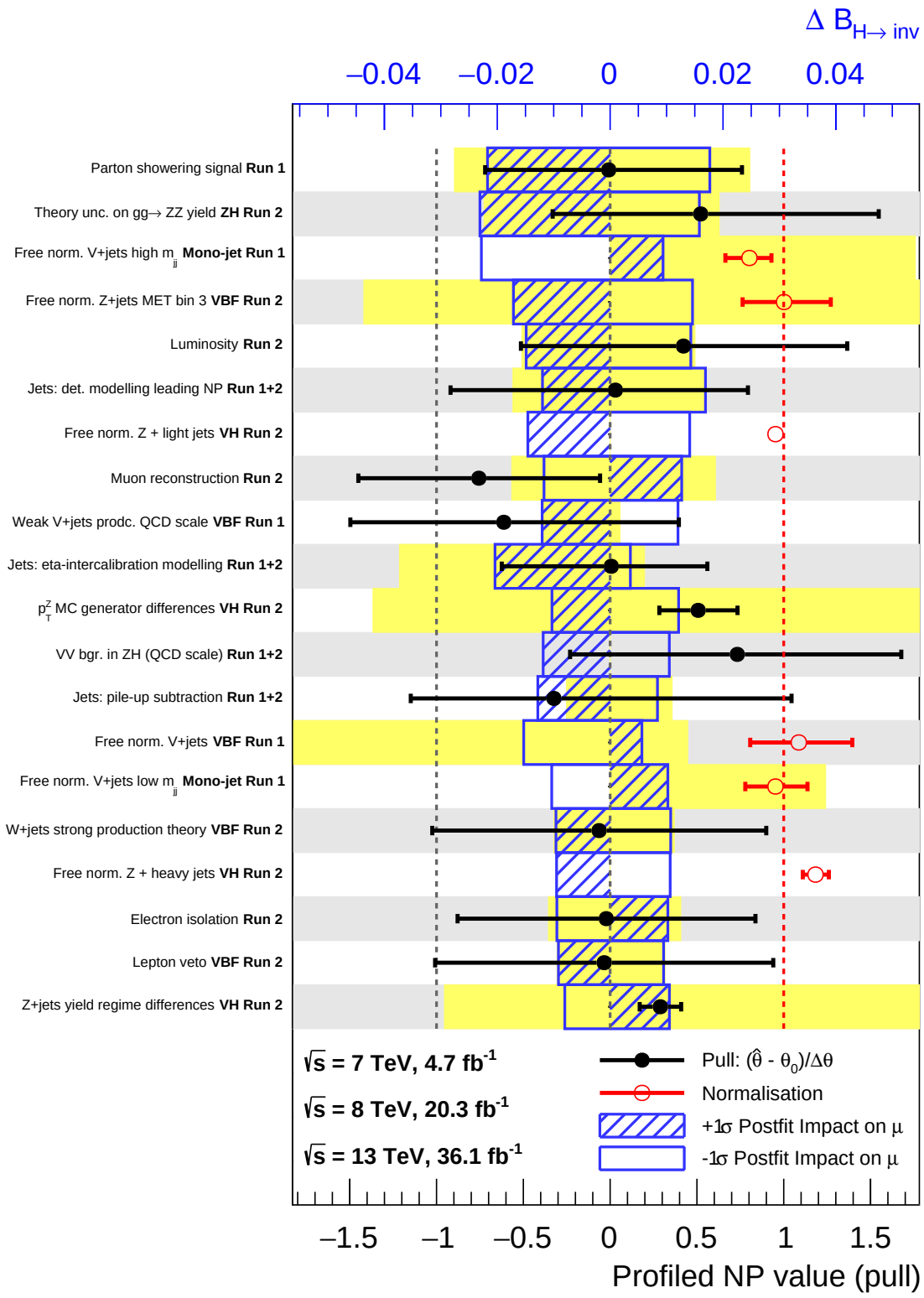

Figure 6.6.: The profiled values of nuisance parameters for the combination of the Run 1+2 searches, ranked according to their post-fit impact on $\mathcal{B}_{H\to\text{inv}}$. Free normalisation parameters shown in red and MC statistic parameters have their nominal value of unity, indicated by the vertical red dashed line.

6.3.4. Correlation Coefficients and Profiled NP Values

The linear correlation coefficients between nuisance parameters are estimated by the fit of the profile likelihood ratio. No significant linear correlation (above 50%) is observed between nuisance parameters from different inputs of Run 2, or between Run 1 and Run 2. All nuisance parameter pairs with sizeable linear correlations in the combined likelihood show this behaviour already in the individual likelihoods of the inputs. Hence, these are no artificial effects of the combination. The profiled nuisance parameter values in the combination are consistent to the inputs. Correlated uncertainties are profiled to values well described by a weighted average of the profiled values in the inputs. Additionally observed are slightly tighter constraints for some correlated nuisance parameters in the combination compared to the inputs since the fit combines information from several analyses. Details can be found in Reference [125].

6.3.5. Breakdown of Systematic Uncertainties

The impact of groups of different sources of systematic uncertainty on the combined Run 1+2 result is estimated via the same method employed for Run 2 in Section 6.2.4. The effect of a specific group is quantified by turning the corresponding nuisance parameters constant to their post-fit values from the generation of an expected post-fit Asimov data set with $\mathcal{B}_{H\to\text{inv}} = 0$. The resulting reduced uncertainty on the most probable invisible branching fraction is quadratically subtracted from the total uncertainty and stated as contribution of the group, summarised in Table 6.6. The general picture of the impact from different uncertainty groups is consistent with the Run 2 result. The contributions compared to Run 2 are generally smaller because of the decreased total uncertainty reflecting the higher sensitivity of the Run 1+2 combination. However, the signal modelling is found to have a larger impact on the Run 1+2 combination which is an effect propagated from higher uncertainties on the signal modelling in the Run 1 combination. This is also reflected by a larger number of nuisance parameters describing uncertainties on the signal modelling in the Run 1 searches. The signal predictions and hence the uncertainties on those have improved from Run 1 to 2 searches resulting in a lower impact of the group in the Run 2 combination. The largest contributions are found for the same groups as in the Run 2 combination, specifically the reconstruction of jets and leptons, the modelling of V+jets and other background sources, and the limited statistics in MC predictions. These observations are consistent with the impact on the expected exclusion limit detailed in Appendix C.

6.3.6. Compatibility between Run 1 and 2

The compatibility between the results of the separate Run 1 and Run 2 combinations is assessed using combined likelihoods. A likelihood model is constructed for the combination of Run 1 with Run 2 using the nominal correlation assumptions for uncertainties between the runs discussed in Section 6.1.2. In contrast to the nominal combination, both the invisible branching ratios of the Run 1 searches $\mathcal{B}^{\text{Run 1}}_{H\to\text{inv}}$ and the Run 2 searches $\mathcal{B}^{\text{Run 2}}_{H\to\text{inv}}$ are not combined but kept as separate parameters of interest, independent except

Group	Contribution		
Luminosity	+ 0.014	- 0.011	± 0.012
Leptons	+ 0.034	- 0.035	± 0.035
Jets	+ 0.030	- 0.032	± 0.031
Flavour tagging	+ 0.005	- 0.005	± 0.005
$E_{\mathrm{T}}^{\mathrm{miss}}$ soft term	+ 0.006	- 0.006	± 0.006
V+jets modelling	+ 0.031	- 0.031	± 0.031
Other backgr. modelling	+ 0.036	- 0.040	± 0.038
Signal modelling	+ 0.024	- 0.024	± 0.024
MC statistics	+ 0.034	- 0.036	± 0.035
All experimental	+ 0.052	- 0.054	± 0.053
All theory	+ 0.047	- 0.059	± 0.048
Theory and experimental	+ 0.068	- 0.070	± 0.069
All systematics	+ 0.074	- 0.076	± 0.075
Data statistics	+ 0.042	- 0.042	± 0.042
Total uncertainty	+ 0.085	- 0.087	± 0.086

Table 6.6.: The impact of different categories of systematic uncertainty on the profiled $\mathcal{B}_{H\to\mathrm{inv}}$ in the Run 2 combination estimated with fits to an Asimov data set with $\mathcal{B}_{H\to\mathrm{inv}} = 0$. The experimental uncertainty and the uncertainty related to the size of the MC sample are treated as separate categories.

for small correlations between the nuisance parameters of both runs. Subsequently, these two parameters are reparameterised to $\mathcal{B}_{H\to\mathrm{inv}}^{\mathrm{Run\,1}}$ and the difference between the invisible branching ratios $\Delta\mathcal{B}_{H\to\mathrm{inv}}$. The Run 2 invisible branching fraction is concurrently kept fixed to

$$\mathcal{B}_{H\to\mathrm{inv}}^{\mathrm{Run\,2}} \equiv \mathcal{B}_{H\to\mathrm{inv}}^{\mathrm{Run\,1}} + \Delta\mathcal{B}_{H\to\mathrm{inv}}\,, \tag{6.1}$$

while $\mathcal{B}_{H\to\mathrm{inv}}^{\mathrm{Run\,1}}$ and $\Delta\mathcal{B}_{H\to\mathrm{inv}}$ are the parameters of interest of the new combined likelihood ratio. A scan of this reparameterised combined profile likelihood ratio is shown as function of $\Delta\mathcal{B}_{H\to\mathrm{inv}}$ in Figure 6.7 as black curve. The second parameter of interest, $\mathcal{B}_{H\to\mathrm{inv}}^{\mathrm{Run\,1}}$ is separately profiled for each value of $\Delta\mathcal{B}_{H\to\mathrm{inv}}$ while $\mathcal{B}_{H\to\mathrm{inv}}^{\mathrm{Run\,2}}$ is fixed to the sum of both parameters as defined in Equation 6.1. The minimum of the parabola represents now the most probable value for the difference between the invisible branching fractions, which corresponds to the separation between the minima of the observed profile likelihood ratios of both runs in Figure 6.4. The value slightly differs from this separation because correlations between both runs are additionally taken into account. The value of the profile likelihood ratio at $\Delta\mathcal{B}_{H\to\mathrm{inv}} = 0$ corresponds to the compatibility between the Run 1 and Run 2 results, incorporating their individual sensitivities and correlations between systematic uncertainties. This can be translated into the number of standard deviations N via

$$-\Delta(\ln\Lambda(\Delta\mathcal{B}_{H\to\mathrm{inv}} = 0)) = \frac{N^2}{2}\,. \tag{6.2}$$

For a given value of $-\Delta(\ln\Lambda) = 2.1$ at $\mathcal{B}_{H\to\text{inv}} = 0$, this results in a compatibility of the Run 1 and Run 2 results at a level of $1.45\,\sigma$. To check the method, the result is re-derived using the reversed reparameterisation, as shown as red curve in Figure 6.7.

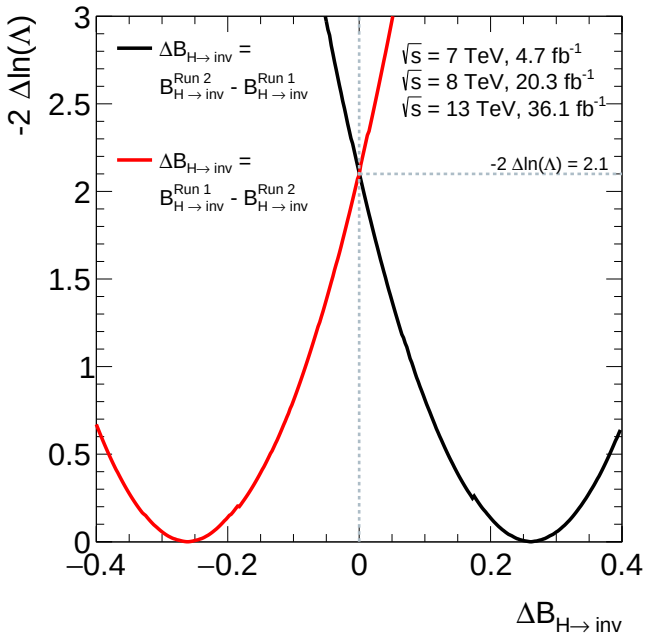

Figure 6.7.: Scan of the combined profile likelihood ratio as function of the difference between the separate invisible branching ratios from Run 1 and Run 2 for two opposite reparameterisations.

6.3.7. Comparison to Direct Detection

The upper exclusion limit on the invisible branching fraction of the Higgs boson can be translated into an upper exclusion limit on the WIMP - nucleon scattering cross section predicted by Higgs portal models. Details on the models and on the translation into $\sigma_{\text{WIMP-}N}$ are shown in Section 2.2.3. Direct Dark Matter detection experiments usually quote upper limits at a 90% confidence level. For a comparison, limits are derived at 90% confidence level with the CL_S method, described in Section 4.1.2 and employed for the previously discussed limits. The result for the Run 1+2 combination is given by

$$\mathcal{B}_{H\to\text{inv}} < 0.24\ (0.14^{+0.06}_{-0.04})\,.$$

This result is compared to exclusion limits from representative direct Dark Matter detection experiments [35–39] in Fig. 6.8. The translation of the presented result into a WIMP–nucleon scattering cross section $\sigma_{\text{WIMP-}N}$ is performed under the assumption that invisible Higgs boson decays to a pair of WIMPs are kinematically possible and that the WIMP is a scalar or a fermion [66, 69, 73]. The resulting $\sigma_{\text{WIMP-}N}$ in necessarily spin-independent since the scalar Higgs boson is assumed as mediator between SM and WIMP particles. As expected, the searches presented here are found not to be sensitive in the

kinematic region where the WIMP particles become too heavy for the Higgs boson to decay to pairs of WIMPs. At lower masses $\sigma_{\text{WIMP-}N}$ down to 10^{-45} cm can be excluded in the scalar WIMP scenario. If the WIMP is a fermion, the effective coupling is reduced by m_H^2 relative to the scalar scenario, resulting in a much stronger exclusion on $\sigma_{\text{WIMP-}N}$ down to 10^{-46} cm. The exclusion limits derived from the results presented here extend to smaller masses below a GeV. However this region is subject to uncertainties due to hadronic bound states. This affects comparisons with direct detection results as well as relic density calculations [12, 126]. In summary, the limits obtained from searches for invisible decays of the Higgs boson are found to be complementary to direct searches for dark matter in the lower WIMP mass region, particularly for $m_{\text{WIMP}} < 10\,\text{GeV}$.

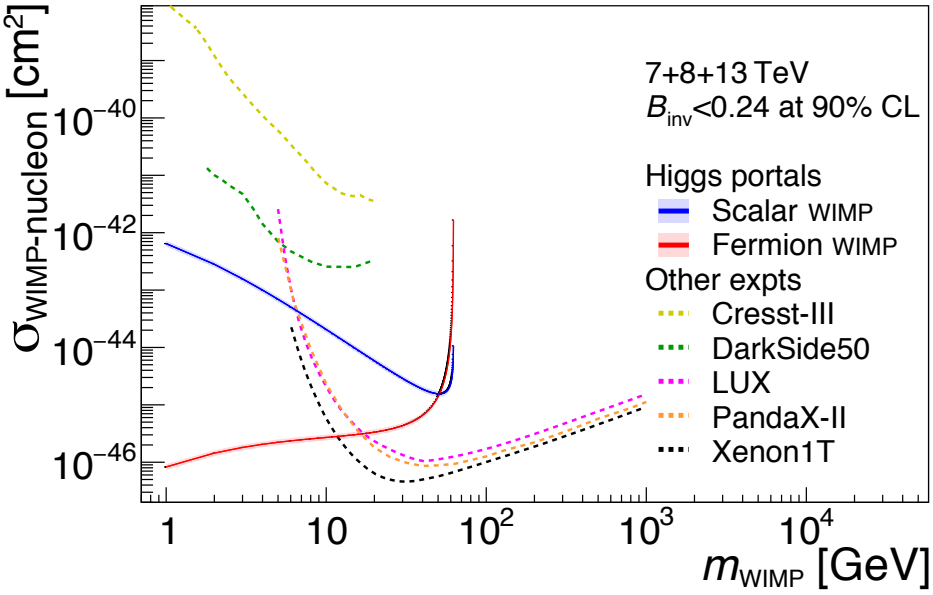

Figure 6.8.: Comparison of the CL_S exclusion limits at 90% confidence level from direct detection experiments [35–39] on the spin-independent WIMP-nucleon scattering cross section to the exclusion limits from this analysis, assuming that the DM particle is either a scalar or a fermion. The regions above the limit contours are excluded in the range shown in the plot.

7. Conclusions and Outlook

The Higgs sector was a significant building block of the Standard Model (SM) to be experimentally observed. Measurements of the Higgs boson properties constitute an important test of the SM and could hint to yet unknown physics. In particular the dark sector could be coupled to the SM via a Higgs portal, which would manifesting itself through invisible decays of the Higgs boson to DM particles if kinematically accessible. Invisible decays of the Higgs boson are directly searched for by the ATLAS collaboration in three different topologies: the vector boson fusion (VBF), Higgsstrahlung from a Z boson decaying into charged leptons ($Z_{\ell\bar{\ell}}H$), and Higgsstrahlung from a W or Z boson decaying into hadrons ($V_{q\bar{q}}H$).

A statistical combination of searches for invisible Higgs boson decays in these topologies using $36\,\text{fb}^{-1}$ of pp collision data as part of the LHC Run 2 is presented in this Thesis. A further combination is performed adding the combined ATLAS Run 1 result for invisible Higgs boson decays. The statistical interpretation of the searches is carried out with the modified frequentists CL_S limit setting procedure using the profile likelihood ratio as test statistic and the asymptotic approximation. Correlations between sources of systematic uncertainty are properly taken into account by affecting all combined searches simultaneously. The combined observed (expected) limit at 95% confidence level of the Run 2 searches is calculated to $\mathcal{B}_{H\to\text{inv}} < 0.38$ $(0.21^{+0.08}_{-0.06})$. A stronger expected limit is obtained by including information from different topologies, while the observed excesses over the expected number of events in all three input searches propagate to the combined result. The corresponding limit for the Run 1+2 combination of searches for invisible Higgs boson decays is $\mathcal{B}_{H\to\text{inv}} < 0.26$ $(0.17^{+0.07}_{-0.05})$. The sensitivity is further increased by adding the statistically independent Run 1 searches. The tension between expected and observed results relaxes due to the slight deficit of observed events in the Run 1 combination. The result is translated into an upper limit on the WIMP - nucleon cross section for scalar and fermionic WIMP hypotheses using the Higgs portal framework. The comparison to spin-independent results from different DM direct detection experiments indicated individual complementarity, especially for WIMP masses in the region $m_{WIMP} \lesssim 10\,\text{GeV}$. Sources of systematic uncertainty are grouped into categories and the impact of uncertainty categories on the result is estimated by turning off the effect of systematic uncertainties belonging to a specific category in the calculation of the most probable expected value for $\mathcal{B}_{H\to\text{inv}}$ and its systematic uncertainty. The largest effects on the Run 1+2 combined result are found for systematic uncertainties related to the modelling of V+jets and other backgrounds, the reconstruction and properties of jets and leptons, and the available statistical precision of Monte-Carlo predictions. Cross checks on the combined likelihood are performed by ranking the systematic uncertainties by their post-fit impact on the fitted $\mathcal{B}_{H\to\text{inv}}$. Furthermore, the deviation of fitted systematic uncertainties from the nominal values and linear correlation coefficients are studied. The

observations are found to be consistent with individual results obtained from the input searches alone. The results from combined ATLAS Run 1 and Run 2 searches separately are estimated to be consistent at a level of $1.4\,\sigma$.

The ATLAS collaboration published a combination of the presented Run 2 results with constraints obtained from measurements of visible decay channels of the Higgs boson [127] by fitting the couplings to visible particles and the invisible branching fraction simultaneously. The full Run 2 dataset including the data-taking periods in 2017 and 2018 will be used to conduct enhanced direct searches for invisible Higgs boson decays in the VBF, $Z_{\ell\bar{\ell}}H$ and $V_{q\bar{q}}H$ topologies. Additionally, the ggF, ttH and $W(\ell\nu)H$ topologies will be explored with dedicated searches. The findings of the studies presented here are intended as well to be used in the planing and construction of future searches for invisible Higgs boson decays and ATLAS searches for DM in general. Ideas in this direction include the implementation of event selections from all direct searches into the analyses. An event that passes selections of multiple searches could thus be prioritized for the search with the highest sensitivity and discarded by the remaining searches. Hence, complete statistical orthogonality of the searches would be enforced by construction. Another important aspect are parameterisations and reductions schemes for systematic uncertainties as well as the merging of different systematics into a single nuisance parameter. The unification across searches, especially for uncertainties on reconstructed objects, but also for theoretical determinations of systematics where applicable, would facilitate and increase the possible sensitivity reach of future combinations from the beginning.

Projections for upper limits on $\mathcal{B}_{H\to\text{inv}}$ including the planned increase in integrated luminosity with the HL-LHC stage range around a few percent. A difficulty arising from the higher luminosity is the large increase in pile-up. This imposes a peculiar challenge for the most sensitive search in the VBF topology. Here, the two VBF jets have to be reliably distinguished from pile-up jets despite the experimentally demanding conditions of the very forward region.

Searches for invisible decays of the Higgs boson can be conducted at future e^+e^- colliders as well. The design goals of the proposed colliders experiments include the precise measurements of Higgs boson properties. The invisible branching fraction can be inferred indirectly by measurements of the visible decay channels or directly through the statistically abundant $e^+e^- \to ZH$ production channel. Projections from the ILC and CLIC collaborations reach an upper limit on $\mathcal{B}_{H\to\text{inv}}$ around one percent.

Bibliography

[1] ATLAS Collaboration, *Observation of a new particle in the search for the Standard Model Higgs boson with the ATLAS detector at the LHC*, Phys. Lett. B **716** (2012) 1, arXiv: 1207.7214 [hep-ex].

[2] CMS Collaboration, *Observation of a new boson at a mass of 125 GeV with the CMS experiment at the LHC*, Phys. Lett. B **716** (2012) 30, arXiv: 1207.7235 [hep-ex].

[3] ATLAS Collaboration, *Constraints on new phenomena via Higgs boson couplings and invisible decays with the ATLAS detector*, JHEP **11** (2015) 206, arXiv: 1509.00672 [hep-ex].

[4] ATLAS Collaboration, *Search for invisible Higgs boson decays in vector boson fusion at $\sqrt{s} = 13$ TeV with the ATLAS detector*, Physics Letters B (2019), ISSN: 0370-2693, arXiv: 1809.06682 [hep-ex], URL: http://www.sciencedirect.com/science/article/pii/S0370269319302564.

[5] ATLAS Collaboration, *Search for an invisibly decaying Higgs boson or dark matter candidates produced in association with a Z boson in pp collisions at $\sqrt{s} = 13$ TeV with the ATLAS detector*, Phys. Lett. **B776** (2018) 318, arXiv: 1708.09624 [hep-ex].

[6] ATLAS Collaboration, *Search for dark matter in events with a hadronically decaying vector boson and missing transverse momentum in pp collisions at $\sqrt{s} = 13$ TeV with the ATLAS detector*, Submitted to: JHEP (2018), arXiv: 1807.11471 [hep-ex].

[7] CMS Collaboration, *Search for invisible decays of a Higgs boson produced through vector boson fusion in proton-proton collisions at $\sqrt{s} = 13$ TeV*, (2018), arXiv: 1809.05937 [hep-ex].

[8] CMS Collaboration, *Search for new physics in events with a leptonically decaying Z boson and a large transverse momentum imbalance in proton–proton collisions at $\sqrt{s} = 13$ TeV*, Eur. Phys. J. **C78** (2018) 291, arXiv: 1711.00431 [hep-ex].

[9] CMS Collaboration, *Search for new physics in final states with an energetic jet or a hadronically decaying W or Z boson and transverse momentum imbalance at $\sqrt{s} = 13$* TeV, Phys. Rev. **D97** (2018) 092005, arXiv: 1712.02345 [hep-ex].

[10] CMS Collaboration, *Searches for invisible decays of the Higgs boson in pp collisions at $\sqrt{s} = 7$, 8, and 13 TeV*, JHEP **02** (2017) 135, arXiv: 1610.09218 [hep-ex].

[11] CMS Collaboration, *Search for invisible decays of Higgs bosons in the vector boson fusion and associated ZH production modes*, Eur. Phys. J. **C74** (2014) 2980, arXiv: 1404.1344 [hep-ex].

[12] ATLAS Collaboration, *Combination of searches for invisible Higgs boson decays with the ATLAS experiment*, (2019), arXiv: 1904.05105 [hep-ex].

[13] S. Weinberg, *A Model of Leptons*, Phys. Rev. Lett. **19** (1967) 1264.

[14] S. L. Glashow, *Partial Symmetries of Weak Interactions*, Nucl. Phys. **22** (1961) 579.

[15] A. Salam and J. C. Ward, *Electromagnetic and Weak Interactions*, Phys. Lett. **13** (1964) 168.

[16] M. Tanabashi et al., *Review of Particle Physics*, Phys. Rev. **D98** (2018) 030001.

[17] P. W. Higgs, *Broken Symmetries, Massless Particles and Gauge Fields*, Phys. Lett. **12** (1964) 132.

[18] V. L Ginzburg and L. D. Landau, *On the Theory of Superconductivity*, Zh. Eksp. Teor. Fizz. **20** (1950) 1064.

[19] A. M. Cooper-Sarkar, *PDF Fits at HERA*, PoS **EPS-HEP2011** (2011) 320, arXiv: 1112.2107 [hep-ph].

[20] The LHC Higgs cross section working group, *Thoretical predictions of Higgs production cross sections.* 04.2019, URL: https://twiki.cern.ch/twiki/bin/view/LHCPhysics/CERNHLHE2019.

[21] L. Bergström, *Non-baryonic dark matter: observational evidence and detection methods*, Reports on Progress in Physics **63** (2000) 793, URL: https://doi.org/10.1088%2F0034-4885%2F63%2F5%2F2r3.

[22] D. Clowe et al., *A direct empirical proof of the existence of dark matter*, Astrophys. J. **648** (2006) L109, arXiv: astro-ph/0608407 [astro-ph].

[23] G. Bertone, D. Hooper, and J. Silk, *Particle dark matter: Evidence, candidates and constraints*, Phys. Rept. **405** (2005) 279, arXiv: hep-ph/0404175.

[24] A. H. Broeils, K. G. Begeman, and R. H. Sanders, *Extended rotation curves of spiral galaxies: dark haloes and modified dynamics*, Monthly Notices of the Royal Astronomical Society **249** (1991) 523, ISSN: 0035-8711, eprint: http://oup.prod.sis.lan/mnras/article-pdf/249/3/523/18160929/mnras249-0523.pdf, URL: https://doi.org/10.1093/mnras/249.3.523.

[25] R. Adam et al., *Planck 2015 results. I. Overview of products and scientific results*, Astron. Astrophys. **594** (2016) A1, arXiv: 1502.01582 [astro-ph.CO].

[26] D. Clowe, A. Gonzalez, and M. Markevitch,
Weak-Lensing Mass Reconstruction of the Interacting Cluster 1E 0657-558: Direct Evidence for the Existence of Dark Matter,
The Astrophysical Journal **604** (2004) 596,
URL: https://doi.org/10.1086%2F381970.

[27] *The Bullet Cluster 1E 0657-56, optical spectrum from Magellan and HST, x-ray spectrum from Chandra*, 04.2019,
URL: http://chandra.harvard.edu/photo/2006/1e0657/more.html.

[28] L. Roszkowski, E. M. Sessolo, and S. Trojanowski,
WIMP dark matter candidates and searches—current status and future prospects,
Rept. Prog. Phys. **81** (2018) 066201, arXiv: 1707.06277 [hep-ph].

[29] M. Taoso, G. Bertone, and A. Masiero,
Dark Matter Candidates: A Ten-Point Test, JCAP **0803** (2008) 022,
arXiv: 0711.4996 [astro-ph].

[30] G. Branco et al., *Theory and phenomenology of two-Higgs-doublet models*,
Physics Reports **516** (2012) 1 , Theory and phenomenology of two-Higgs-doublet models, ISSN: 0370-1573, URL:
http://www.sciencedirect.com/science/article/pii/S0370157312000695.

[31] R. Daido, F. Takahashi, and W. Yin,
The ALP miracle: unified inflaton and dark matter, JCAP **1705** (2017) 044,
arXiv: 1702.03284 [hep-ph].

[32] N. Du et al., *A Search for Invisible Axion Dark Matter with the Axion Dark Matter Experiment*, Phys. Rev. Lett. **120** (2018) 151301,
arXiv: 1804.05750 [hep-ex].

[33] T. Marrodán Undagoitia and L. Rauch, *Dark matter direct-detection experiments*,
J. Phys. **G43** (2016) 013001, arXiv: 1509.08767 [physics.ins-det].

[34] A. P. Colijng,
Particle Cosmology: DM Direct Detection, Topical Lectures "Dark Matter", 2015,
URL: https://indico.nikhef.nl/event/869/material/0/1.pdf.

[35] F. Petricca et al.,
'First results on low-mass dark matter from the CRESST-III experiment', 2017,
arXiv: 1711.07692 [astro-ph.CO].

[36] D. S. Akerib et al.,
Results from a search for dark matter in the complete LUX exposure,
Phys. Rev. Lett. **118** (2017) 021303, arXiv: 1608.07648 [astro-ph.CO].

[37] X. Cui et al.,
Dark Matter Results From 54-Ton-Day Exposure of PandaX-II Experiment,
Phys. Rev. Lett. **119** (2017) 181302, arXiv: 1708.06917 [astro-ph.CO].

[38] E. Aprile et al.,
Dark Matter Search Results from a One Ton-Year Exposure of XENON1T,
Phys. Rev. Lett. **121** (2018) 111302, arXiv: 1805.12562 [astro-ph.CO].

[39] P. Agnes et al., *Low-Mass Dark Matter Search with the DarkSide-50 Experiment*, Phys. Rev. Lett. **121** (2018) 081307, arXiv: 1802.06994 [astro-ph.HE].

[40] L. Roszkowski, E. M. Sessolo, and S. Trojanowski, *WIMP dark matter candidates and searches—current status and future prospects*, Rept. Prog. Phys. **81** (2018) 066201, arXiv: 1707.06277 [hep-ph].

[41] G. Bertone and D. Merritt, *Dark matter dynamics and indirect detection*, Mod. Phys. Lett. **A20** (2005) 1021, arXiv: astro-ph/0504422 [astro-ph].

[42] J. Conrad and O. Reimer, *Indirect dark matter searches in gamma and cosmic rays*, Nature Phys. **13** (2017) 224, arXiv: 1705.11165 [astro-ph.HE].

[43] M. Ackermann et al., *Constraining Dark Matter Models from a Combined Analysis of Milky Way Satellites with the Fermi Large Area Telescope*, Phys. Rev. Lett. **107** (2011) 241302, arXiv: 1108.3546 [astro-ph.HE].

[44] M. A. et al., *First Result from the Alpha Magnetic Spectrometer on the International Space Station: Precision Measurement of the Positron Fraction in Primary Cosmic Rays of 0.5–350 GeV*, Phys. Rev. Lett. **110** (14 2013) 141102, URL: https://link.aps.org/doi/10.1103/PhysRevLett.110.141102.

[45] H. Abdallah et al., *Search for dark matter annihilations towards the inner Galactic halo from 10 years of observations with H.E.S.S*, Phys. Rev. Lett. **117** (2016) 111301, arXiv: 1607.08142 [astro-ph.HE].

[46] F. Halzen and S. R. Klein, *IceCube: An Instrument for Neutrino Astronomy*, Rev. Sci. Instrum. **81** (2010) 081101, arXiv: 1007.1247 [astro-ph.HE].

[47] F. Kahlhoefer, *Review of LHC Dark Matter Searches*, Int. J. Mod. Phys. **A32** (2017) 1730006, arXiv: 1702.02430 [hep-ph].

[48] J. Abdallah et al., *Simplified Models for Dark Matter Searches at the LHC*, Phys. Dark Univ. **9-10** (2015) 8, arXiv: 1506.03116 [hep-ph].

[49] A. Albert et al., *Recommendations of the LHC Dark Matter Working Group: Comparing LHC searches for heavy mediators of dark matter production in visible and invisible decay channels*, (2017), arXiv: 1703.05703 [hep-ex].

[50] G. Busoni et al., *Recommendations on presenting LHC searches for missing transverse energy signals using simplified s-channel models of dark matter*, (2016), ed. by A. Boveia et al., arXiv: 1603.04156 [hep-ex].

[51] J. M. Lindert et al., *Precise predictions for V+ jets dark matter backgrounds*, Eur. Phys. J. **C77** (2017) 829, arXiv: 1705.04664 [hep-ph].

[52] M. Bauer, U. Haisch, and F. Kahlhoefer, *Simplified dark matter models with two Higgs doublets: I. Pseudoscalar mediators*, JHEP **05** (2017) 138, arXiv: 1701.07427 [hep-ph].

[53] T. Abe et al., *LHC Dark Matter Working Group: Next-generation spin-0 dark matter models*, (2018), arXiv: 1810.09420 [hep-ex].

[54] ATLAS Collaboration,
Search for dark matter and other new phenomena in events with an energetic jet and large missing transverse momentum using the ATLAS detector,
JHEP **01** (2018) 126, arXiv: 1711.03301 [hep-ex].

[55] ATLAS Collaboration,
Search for dark matter at $\sqrt{s} = 13$ TeV in final states containing an energetic photon and large missing transverse momentum with the ATLAS detector,
Eur. Phys. J. **C77** (2017) 393, arXiv: 1704.03848 [hep-ex].

[56] ATLAS Collaboration, *Summary plots from the ATLAS Exotic physics group*, March 2019, URL: https://atlas.web.cern.ch/Atlas/GROUPS/PHYSICS/CombinedSummaryPlots/EXOTICS/.

[57] B. Patt and F. Wilczek, *Higgs-field portal into hidden sectors*, (2006), arXiv: hep-ph/0605188 [hep-ph].

[58] I. Antoniadis, M. Tuckmantel, and F. Zwirner,
Phenomenology of a leptonic goldstino and invisible Higgs boson decays,
Nucl. Phys. **B707** (2005) 215, arXiv: hep-ph/0410165 [hep-ph].

[59] N. Arkani-Hamed, S. Dimopoulos, G. R. Dvali, and J. March-Russell,
Neutrino masses from large extra dimensions, Phys. Rev. **D65** (2001) 024032, arXiv: hep-ph/9811448 [hep-ph].

[60] A. Datta, K. Huitu, J. Laamanen, and B. Mukhopadhyaya,
Invisible Higgs in theories of large extra dimensions,
Phys. Rev. **D70** (2004) 075003, arXiv: hep-ph/0404056 [hep-ph].

[61] S. Kanemura, S. Matsumoto, T. Nabeshima, and N. Okada,
Can WIMP Dark Matter overcome the Nightmare Scenario?,
Phys. Rev. **D82** (2010) 055026, arXiv: 1005.5651 [hep-ph].

[62] A. Djouadi, O. Lebedev, Y. Mambrini, and J. Quevillon,
Implications of LHC searches for Higgs–portal dark matter,
Phys. Lett. **B709** (2012) 65, arXiv: 1112.3299 [hep-ph].

[63] A. Djouadi, A. Falkowski, Y. Mambrini, and J. Quevillon,
Direct Detection of Higgs-Portal Dark Matter at the LHC,
Eur. Phys. J. **C73** (2013) 2455, arXiv: 1205.3169 [hep-ph].

[64] R. E. Shrock and M. Suzuki, *Invisible decays of Higgs bosons*,
Physics Letters B **110** (1982) 250 , ISSN: 0370-2693, URL: http://www.sciencedirect.com/science/article/pii/0370269382912473.

[65] D. Choudhury and D. P. Roy,
Signatures of an invisibly decaying Higgs particle at LHC,
Phys. Lett. **B322** (1994) 368, arXiv: hep-ph/9312347 [hep-ph].

[66] O. J. P. Eboli and D. Zeppenfeld, *Observing an invisible Higgs boson*,
Phys. Lett. **B495** (2000) 147, arXiv: hep-ph/0009158 [hep-ph].

[67] H. Davoudiasl, T. Han, and H. E. Logan,
Discovering an invisibly decaying Higgs at hadron colliders,
Phys. Rev. **D71** (2005) 115007, arXiv: hep-ph/0412269 [hep-ph].

[68] R. M. Godbole, M. Guchait, K. Mazumdar, S. Moretti, and D. P. Roy, *Search for 'invisible' Higgs signals at LHC via associated production with gauge bosons*,
Phys. Lett. **B571** (2003) 184, arXiv: hep-ph/0304137 [hep-ph].

[69] P. J. Fox, R. Harnik, J. Kopp, and Y. Tsai,
Missing Energy Signatures of Dark Matter at the LHC,
Phys. Rev. **D85** (2012) 056011, arXiv: 1109.4398 [hep-ph].

[70] D. Ghosh, R. Godbole, M. Guchait, K. Mohan, and D. Sengupta,
Looking for an Invisible Higgs Signal at the LHC, Phys. Lett. **B725** (2013) 344,
arXiv: 1211.7015 [hep-ph].

[71] G. Belanger, B. Dumont, U. Ellwanger, J. F. Gunion, and S. Kraml,
Status of invisible Higgs decays, Phys. Lett. **B723** (2013) 340,
arXiv: 1302.5694 [hep-ph].

[72] D. Curtin et al., *Exotic decays of the 125 GeV Higgs boson*,
Phys. Rev. **D90** (2014) 075004, arXiv: 1312.4992 [hep-ph].

[73] A. De Simone, G. F. Giudice, and A. Strumia,
Benchmarks for Dark Matter Searches at the LHC, JHEP **06** (2014) 081,
arXiv: 1402.6287 [hep-ph].

[74] M. Hoferichter, P. Klos, J. Menéndez, and A. Schwenk,
Improved limits for Higgs-portal dark matter from LHC searches,
Phys. Rev. Lett. **119** (2017) 181803, arXiv: 1708.02245 [hep-ph].

[75] O. S. Bruning et al., *LHC Design Report Vol.1: The LHC Main Ring*, (2004).

[76] F. Marcastel,
CERN's Accelerator Complex. La chaîne des accélérateurs du CERN,
(2013), General Photo, URL: https://cds.cern.ch/record/1621583.

[77] ATLAS Collaboration, *Luminosity Public Results*, 04.2019,
URL: https://twiki.cern.ch/twiki/bin/view/AtlasPublic/LuminosityPublicResultsRun2.

[78] T. A. Collaboration, *The ALICE experiment at the CERN LHC*,
Journal of Instrumentation **3** (2008) S08002,
URL: https://doi.org/10.1088%2F1748-0221%2F3%2F08%2Fs08002.

[79] ATLAS Collaboration,
The ATLAS Experiment at the CERN Large Hadron Collider,
JINST **3** (2008) S08003.

[80] T. C. Collaboration, *The CMS experiment at the CERN LHC*,
Journal of Instrumentation **3** (2008) S08004,
URL: https://doi.org/10.1088%2F1748-0221%2F3%2F08%2Fs08004.

[81] T. L. Collaboration, **3** (2008) S08005,
URL: https://doi.org/10.1088%2F1748-0221%2F3%2F08%2Fs08005.

[82] M. Capeans et al., *ATLAS Insertable B-Layer Technical Design Report*,
ATLAS-TDR-19 (2010), URL: http://cds.cern.ch/record/1291633.

[83] G. Cowan et al., *Asymptotic formulae for likelihood-based tests of new physics*,
Eur. Phys. J. C **71** (2011) 1554, [Erratum: Eur. Phys. J. C **73** (2013) 2501],
arXiv: 1007.1727 [physics.data-an].

[84] M. Baak et al., *HistFitter software framework for statistical data analysis*,
Eur. Phys. J. **C75** (2015) 153, arXiv: 1410.1280 [hep-ex].

[85] F. James, *MINUIT Function Minimization and Error Analysis: Reference Manual Version 94.1*, (1994).

[86] J. Neyman and E. S. Pearson,
'On the Problem of the Most Efficient Tests of Statistical Hypotheses',
Breakthroughs in Statistics: Foundations and Basic Theory,
ed. by S. Kotz and N. L. Johnson, Springer New York, 1992 73,
ISBN: 978-1-4612-0919-5,
URL: https://doi.org/10.1007/978-1-4612-0919-5_6.

[87] A. Wald, *Tests of Statistical Hypotheses Concerning Several Parameters When the Number of Observations is Large*,
Transactions of the American Mathematical Society **54** (1943) 426,
ISSN: 00029947, URL: http://www.jstor.org/stable/1990256.

[88] A. L. Read, *Presentation of search results: the CL_s technique*,
J. Phys. G **28** (2002) 2693.

[89] R. Brun and F. Rademakers,
ROOT — An object oriented data analysis framework,
Nuclear Instruments and Methods in Physics Research Section A: Accelerators, Spectrometers, Detectors and Associated Equipment **389** (1997) 81 , New Computing Techniques in Physics Research V, ISSN: 0168-9002, URL:
http://www.sciencedirect.com/science/article/pii/S016890029700048X.

[90] B. Webber, *A QCD model for jet fragmentation including soft gluon interference*,
Nuclear Physics B **238** (1984) 492 , ISSN: 0550-3213, URL:
http://www.sciencedirect.com/science/article/pii/055032138490333X.

[91] T. D. Gottschalk, *An improved description of hadronization in the QCD cluster model for e^+e^- annihilation*, Nuclear Physics B **239** (1984) 349 , ISSN: 0550-3213,
URL:
http://www.sciencedirect.com/science/article/pii/0550321384902530.

[92] B. Andersson, *The Lund Model*, Cambridge Books Online,
Cambridge University Press, 1998, ISBN: 9780511524363,
URL: http://dx.doi.org/10.1017/CBO9780511524363.

[93] M. Cacciari, G. P. Salam, and G. Soyez, *The anti-k_t jet clustering algorithm*,
JHEP **04** (2008) 063, arXiv: 0802.1189 [hep-ph].

[94] A. J. Larkoski, G. P. Salam, and J. Thaler,
Energy Correlation Functions for Jet Substructure, JHEP **06** (2013) 108,
arXiv: 1305.0007 [hep-ph].

[95] J. Thaler and K. Van Tilburg, *Identifying Boosted Objects with N-subjettiness*,
JHEP **03** (2011) 015, arXiv: 1011.2268 [hep-ph].

[96] ATLAS Collaboration, *Identification of boosted, hadronically decaying W bosons and comparisons with ATLAS data taken at $\sqrt{s} = 8$ TeV*,
Eur. Phys. J. **C76** (2016) 154, arXiv: 1510.05821 [hep-ex].

[97] ATLAS Collaboration,
Jet energy scale measurements and their systematic uncertainties in proton–proton collisions at $\sqrt{s} = 13$ TeV with the ATLAS detector, (2017),
arXiv: 1703.09665 [hep-ex].

[98] ATLAS Collaboration,
Jet mass reconstruction with the ATLAS Detector in early Run 2 data,
ATLAS-CONF-2016-035 (2016), URL: https://cds.cern.ch/record/2200211.

[99] ATLAS Collaboration,
Flavor Tagging with Track Jets in Boosted Topologies with the ATLAS Detector,
(2014), URL: http://cds.cern.ch/record/1712269.

[100] ATLAS Collaboration,
Performance of b-Jet Identification in the ATLAS Experiment,
JINST **11** (2016) P04008, arXiv: 1512.01094 [hep-ex].

[101] ATLAS Collaboration,
Optimisation of the ATLAS b-tagging performance for the 2016 LHC Run,
ATL-PHYS-PUB-2016-012 (2016),
URL: https://cds.cern.ch/record/2160731.

[102] ATLAS Collaboration, *Performance of pile-up mitigation techniques for jets in pp collisions at $\sqrt{s} = 8$ TeV using the ATLAS detector*,
Eur. Phys. J. **C76** (2016) 581, arXiv: 1510.03823 [hep-ex].

[103] ATLAS Collaboration, *Jet performance group recommendations for JVT*,
04.2019, URL:
https://twiki.cern.ch/twiki/bin/view/AtlasProtected/JVTCalibration.

[104] ATLAS Collaboration, *Jet performance group recommendations*, 04.2019,
URL: https://twiki.cern.ch/twiki/bin/view/AtlasProtected/
JetUncertainties20152016Data20p7.

[105] ATLAS Collaboration, *Electron and photon energy calibration with the ATLAS detector using LHC Run 1 data*, Eur. Phys. J. C **74** (2014) 3071,
arXiv: 1407.5063 [hep-ex].

[106] ATLAS Collaboration, *Electron efficiency measurements with the ATLAS detector using the 2015 LHC proton-proton collision data*,
tech. rep. ATLAS-CONF-2016-024, CERN, 2016,
URL: https://cds.cern.ch/record/2157687.

[107] W Lampl et al., *Calorimeter clustering algorithms: description and performance*, (2008), URL: http://cdsweb.cern.ch/record/1099735.

[108] ATLAS Collaboration, *Electron+Photon performance group recommendations*, 04.2019, URL: https://twiki.cern.ch/twiki/bin/view/AtlasProtected/ElectronEfficiencyRun2.

[109] ATLAS Collaboration, *Muon reconstruction performance of the ATLAS detector in proton–proton collision data at $\sqrt{s}$ =13 TeV*, Eur. Phys. J. C **76** (2016) 292, arXiv: 1603.05598 [hep-ex].

[110] ATLAS Collaboration, *Muon performance group recommendations*, 04.2019, URL: https://twiki.cern.ch/twiki/bin/viewauth/AtlasProtected/MCPAnalysisGuidelinesMC15.

[111] ATLAS Collaboration, *Performance of missing transverse momentum reconstruction with the ATLAS detector using proton-proton collisions at $\sqrt{s}$ = 13 TeV*, Eur. Phys. J. **C78** (2018) 903, arXiv: 1802.08168 [hep-ex].

[112] ATLAS Collaboration, *MET performance group recommendations for track based soft term*, 04.2019, URL: https://twiki.cern.ch/twiki/bin/viewauth/AtlasProtected/EtmissRecommendationsRel20p7.

[113] D. Krohn, J. Thaler, and L.-T. Wang, *Jet trimming*, JHEP **02** (2010) 084, arXiv: 0912.1342 [hep-ph].

[114] ATLAS Collaboration, *Flavour tagging performance group recommendations*, 04.2019, URL: https://twiki.cern.ch/twiki/bin/view/AtlasProtected/BTagCalib2015.

[115] ATLAS Collaboration, *Extrapolating Errors for b-tagging - internal documentation*, tech. rep. ATL-COM-PHYS-2015-711, This is for internal information only, no approval to ever be seen outside of ATLAS.: CERN, 2015, URL: https://cds.cern.ch/record/2034234.

[116] ATLAS Collaboration, *MC tuning recommendations*, 04.2019, URL: https://twiki.cern.ch/twiki/bin/view/AtlasProtected/MCTuningRecommendations.

[117] ATLAS Collaboration, *ATLAS Pythia 8 tunes to 7 TeV data*, ATL-PHYS-PUB-2014-021, 2014, URL: http://cdsweb.cern.ch/record/1966419.

[118] ATLAS Collaboration, *Search for squarks and gluinos with the ATLAS detector in final states with jets and missing transverse momentum using 4.7 fb^{-1} of $\sqrt{s} = 7$ TeV proton-proton collision data*, Phys. Rev. **D87** (2013) 012008, arXiv: 1208.0949 [hep-ex].

[119] ATLAS Collaboration, *Search for invisible decays of a Higgs boson using vector-boson fusion in pp collisions at $\sqrt{s} = 8$ TeV with the ATLAS detector*, JHEP **01** (2016) 172, arXiv: 1508.07869 [hep-ex].

[120] ATLAS Collaboration, *Search for Invisible Decays of a Higgs Boson Produced in Association with a Z Boson in ATLAS*, Phys. Rev. Lett. **112** (2014) 201802, arXiv: 1402.3244 [hep-ex].

[121] ATLAS Collaboration, *Search for invisible decays of the Higgs boson produced in association with a hadronically decaying vector boson in pp collisions at $\sqrt{s}$ = 8 TeV with the ATLAS detector*, Eur. Phys. J. **C75** (2015) 337, arXiv: 1504.04324 [hep-ex].

[122] ATLAS Collaboration, *Combined measurements of Higgs boson production and decay using up to 80 fb^{-1} of proton–proton collision data at $\sqrt{s}$ = 13 TeV collected with the ATLAS experiment*, ATLAS-CONF-2018-031 (2018), URL: http://cdsweb.cern.ch/record/2629412.

[123] ATLAS Collaboration, *Luminosity determination in pp collisions at $\sqrt{s}$ = 8 TeV using the ATLAS detector at the LHC*, Eur. Phys. J. **C76** (2016) 653, arXiv: 1608.03953 [hep-ex].

[124] ATLAS Collaboration, *Electron efficiency measurements with the ATLAS detector using the 2012 LHC proton-proton collision data*, ATLAS-CONF-2014-032 (2014), URL: https://cds.cern.ch/record/1706245.

[125] ATLAS Collaboration, *Combination of searches for invisible Higgs boson decays with ATLAS - internal documentation*, tech. rep. ATL-COM-PHYS-2018-709, CERN, 2018, URL: https://cds.cern.ch/record/2320415.

[126] ATLAS Collaboration, *Common Dark Matter group recommendations for speakers*, 04.2019, URL: https://twiki.cern.ch/twiki/bin/viewauth/AtlasProtected/ASpeakersGuideToTheDM.

[127] ATLAS Collaboration, *Combined measurements of Higgs boson production and decay using up to 80 fb^{-1} of proton–proton collision data at $\sqrt{s}$ = 13 TeV collected with the ATLAS experiment*, tech. rep. ATLAS-CONF-2019-005, CERN, 2019, URL: http://cds.cern.ch/record/2668375.

Appendices

A. List of Nuisance Parameters

In this Appendix, the full listing of NPs used in the input searches is presented, with the exception of the MC statistical uncertainties on the single bins of the final observables used in the analysis, as these clearly represent statistically uncorrelated sources of uncertainty.

Table A.1.: Full list of NPs used in the VBF $H \rightarrow$ inv analysis except for the statistical uncertainties on the single bins of the final obversables used in the analysis. Sets of V+Jets theory uncertainties are present separetely for Electroweak (EWK) and Strong (QCD) production, only EWK is depicted.

Nuisance Parameter Name		
ATLAS_LUMI	$E_{\mathbf{T}}^{\mathbf{miss}}$	**Jets**
Leptons	MET_SoftTrk_ResoPara	JET_BJES_Response
EG_RESOLUTION_ALL	MET_SoftTrk_ResoPerp	JET_EffectiveNP_Detector1
EG_SCALE_ALL	MET_SoftTrk_Scale	JET_EffectiveNP_Detector2
EL_EFF_ID_TOTAL	MET_trigger	JET_EffectiveNP_Mixed1
EL_EFF_ISO	**V+Jets modelling**	JET_EffectiveNP_Mixed2
EL_EFF_Reco_TOTAL	EWK_W-ckkw1	JET_EffectiveNP_Mixed3
EL_EFF_TriggerEff_TOTAL	EWK_W-ckkw2	JET_EffectiveNP_Modelling1
MUON_EFF_STAT	EWK_W-ckkw3	JET_EffectiveNP_Modelling2
MUON_EFF_SYS	EWK_W-fac1	JET_EffectiveNP_Modelling3
MUON_EFF_TrigStat	EWK_W-fac2	JET_EffectiveNP_Modelling4
MUON_EFF_TrigSyst	EWK_W-fac3	JET_EffectiveNP_Statistical1
MUON_ID	EWK_W-pdf1	JET_EffectiveNP_Statistical2
MUON_ISO_STAT	EWK_W-pdf2	JET_EffectiveNP_Statistical3
MUON_ISO_SYS	EWK_W-pdf3	JET_EffectiveNP_Statistical4
MUON_MS	EWK_W-qsf1	JET_EffectiveNP_Statistical5
MUON_SAGITTA_RESBIAS	EWK_W-qsf2	JET_EffectiveNP_Statistical6
MUON_SAGITTA_RHO	EWK_W-qsf3	JET_EffectiveNP_Statistical7
MUON_SCALE	EWK_Z-ckkw1	JET_EtaInt
MUON_TTVA_STAT	EWK_Z-ckkw2	JET_EtaIntercalibration_Modelling
MUON_TTVA_SYS	EWK_Z-ckkw3	JET_EtaIntercalibration_TotalStat
antiIDSF	EWK_Z-fac1	JET_Flavor_Composition
Signal modelling	EWK_Z-fac2	JET_Flavor_Response
GGF_assumeUncert50 *(ggF+2jets in SR)*	EWK_Z-fac3	JET_JVT
HiggsPS	EWK_Z-pdf1	JET_Pileup_OffsetMu
Sig_PDF	EWK_Z-pdf2	JET_Pileup_OffsetNPV
VBF_uncert *(QCD scale & third jet veto)*	EWK_Z-pdf3	JET_Pileup_PtTerm
Pile-up	EWK_Z-qsf1	JET_Pileup_RhoTopology
PRW_DATASF	EWK_Z-qsf2	JET_PunchThrough_MC15
Normalistions	EWK_Z-qsf3	JET_SingleParticle_HighPt
kW1		JET_JER
kW2		
kW3		
kZ1		
kZ2		
kZ3		
norm_fakeel1		
norm_fakeel2		
norm_fakeel3		

Table A.2.: Full list of NPs used in the $Z_{\ell\bar{\ell}}H$ analysis except for the statistical uncertainties on the single bins of the final obversables used in the analysis.

Nuisance Parameter Name	
lumi	**V+J modelling**
$E_{\mathbf{T}}^{\mathbf{miss}}$	Wjets_Stat
MET_SoftTrk_ResoPara	Wjets_Sys
MET_SoftTrk_ResoPerp	Zjets_ABCD_Shape_ee
MET_SoftTrk_Scale	Zjets_ABCD_Shape_mm
Jets	Zjets_ABCD_Stat_ee
JET_EtaIntercalibration_NonClosure	Zjets_ABCD_Stat_mm
JET_GroupedNP_1	Zjets_ABCD_Sys
JET_GroupedNP_2	**Signal modelling**
JET_GroupedNP_3	SigPDF
JET_JER_SINGLE_NP	SigQCD
JET_JvtEfficiency	EW_pTZ *:EW corrections*
Leptons	**Pile-u**
EG_RESOLUTION_ALL	PRW_DATASF
EG_SCALE_ALL	**Other backgrounds**
EL_EFF_ID_TOTAL	QCDscale_VV
EL_EFF_Iso_TOTAL	OtherTheo *(ttV, VVV)*
EL_EFF_Reco_TOTAL	emu_Shape
EL_EFF_Trigger_TOT	ATLAS_pdf_qq (*(ZZ)*)
MUON_EFF_STAT_LOWPT	emu_Stat
MUON_EFF_STAT__1	emu_Sys
MUON_EFF_SYS_LOWPT	ggZZTheo
MUON_EFF_SYS__1	WZScaleInEff
MUON_EFF_TrigStatUncertainty	WZScaleStat
MUON_EFF_TrigSystUncertainty	WZScaleSys
MUON_ID	
MUON_ISO_STAT	**Flavour tagging**
MUON_ISO_SYS	FT_EFF_B_systematics
MUON_MS	FT_EFF_C_systematics
MUON_SAGITTA_RESBIAS	FT_EFF_Light_systematics
MUON_SAGITTA_RHO	FT_EFF_extrapol__1
MUON_SCALE	FT_EFF_extrapol_from_charm
MUON_TTVA_STAT	
MUON_TTVA_SYS	

Table A.3.: First list of NPs used in the $V_{q\bar{q}}H$ analysis except for the statistical uncertainties on the single bins of the final obversables used in the analysis.

Nuisance Parameter Name	
ATLAS_LUMI_2015	**V+J modelling**
$E_{\mathbf{T}}^{\mathbf{miss}}$	*generator differences*
SysMETTrigSyst	SysWPtV
SysMET_JetTrk_Scale	SysZPtV
SysMET_SoftTrk_ResoPara	SysWbcWbbRatio
SysMET_SoftTrk_ResoPerp	SysWblWbbRatio
SysMET_SoftTrk_Scale	SysWccWbbRatio
Jets	SysZbcZbbRatio
large-R (1.0)	SysZblZbbRatio
SysFATJET_JER	SysZccZbbRatio
SysFATJET_JMR	*norm. & shape uncert.*
SysFATJET_Weak_JET_Rtrk_Baseline_D2Beta1	SysWclNorm
SysFATJET_Weak_JET_Rtrk_Baseline_pT	SysZclNorm
SysFATJET_Weak_JET_Rtrk_Modelling_D2Beta1	SysMbbWShapeOnl *(Mbb=di-jet mass)*
SysFATJET_Weak_JET_Rtrk_Modelling_pT	SysMbbZShapeOnly
SysFATJET_Weak_JET_Rtrk_Tracking_D2Beta1	*Regime difference*
SysFATJET_Weak_JET_Rtrk_Tracking_pT	SysZjetsResVsMerged
small-R (0.4)	SysWjetsResVsMerged
SysJET_JET_GroupedNP_1	**Signal modelling**
SysJET_JET_GroupedNP_2	*QCD scale, PDF and Parton Shower*
SysJET_JET_GroupedNP_3	SysVHinvQCDscaleAcc
SysJET_JET_EtaIntercalibration_NonClosure	SysVHinvXSQCD
SysJET_JER_SINGLE_NP	SysVHinvXSPDF
Leptons	SysVHinvPDFAcc
SysEG_RESOLUTION_ALL	SysVHinvPDFShape
SysEG_SCALE_ALL	SysVHinvPSTunesAcc
SysEL_EFF_ID_TOTAL	SysVHinvPSTunesShape
SysEL_EFF_Iso_TOTAL	SysggHinvPDFAcc
SysEL_EFF_Reco_TOTAL	SysggHinvPDFshape
SysEL_EFF_Trigger_TOTAL	SysggHinvPSTunesAcc
SysMUON_EFF_STAT	SysggHinvPSTunesshape
SysMUON_EFF_SYS	SysggHinvQCDscaleAcc
SysMUON_ISO_SYS	SysggHinvXSPDF
SysMUON_TTVA_STAT	**Pile-up**
SysMUON_TTVA_SYS	SysPRW_DATASF

Table A.4.: Second list of NPs used in the $V_{q\bar{q}}H$ analysis except for the statistical uncertainties on the single bins of the final obversables used in the analysis.

Nuisance Parameter Name	
Flavour tagging	**Other backgrounds**
b-tagging efficiencies EVs	*regions: b-tag,regime,mass window*
FT_B_0_AntiKt2PV0TrackJets	SysMJ_Shape0mergedMassFail
FT_B_0_AntiKt4EMTopoJets	SysMJ_Shape0mergedMassPass
FT_B_1_AntiKt2PV0TrackJets	SysMJ_Shape0resolvedMassFail
FT_B_1_AntiKt4EMTopoJets	SysMJ_Shape0resolvedMassPass
FT_B_2_AntiKt2PV0TrackJets_Ys2015	SysMJ_Shape1mergedMassFail
FT_B_2_AntiKt4EMTopoJets	SysMJ_Shape1mergedMassPass
FT_C_0_AntiKt2PV0TrackJets	SysMJ_Shape1resolvedMassFail
FT_C_0_AntiKt4EMTopoJets	SysMJ_Shape1resolvedMassPass
FT_C_1_AntiKt2PV0TrackJets	SysMJ_Shape2mergedMassFail
FT_C_1_AntiKt4EMTopoJets	SysMJ_Shape2mergedMassPass
FT_C_2_AntiKt2PV0TrackJets	SysMJ_Shape2resolvedMassFail
FT_C_2_AntiKt4EMTopoJets	SysMJ_Shape2resolvedMassPass
FT_C_3_AntiKt2PV0TrackJets	Multijet0mergedMassFailNorm
FT_Light_0_AntiKt2PV0TrackJets	Multijet0mergedMassPassNorm
FT_Light_0_AntiKt4EMTopoJets	Multijet0resolvedMassFailNorm
FT_Light_1_AntiKt2PV0TrackJets	Multijet0resolvedMassPassNorm
FT_Light_1_AntiKt4EMTopoJets	Multijet1mergedMassFailNorm
FT_Light_2_AntiKt2PV0TrackJets	Multijet1mergedMassPassNorm
FT_Light_2_AntiKt4EMTopoJets	Multijet1resolvedMassFailNorm
FT_Light_3_AntiKt2PV0TrackJets	Multijet1resolvedMassPassNorm
FT_Light_3_AntiKt4EMTopoJets	Multijet2mergedMassFailNorm
FT_Light_4_AntiKt2PV0TrackJets	Multijet2mergedMassPassNorm
FT_Light_4_AntiKt4EMTopoJets	Multijet2resolvedMassFailNorm
SysFT_EFF_extrapol_AntiKt2PV0TrackJets	Multijet2resolvedMassPassNorm
SysFT_EFF_extrapol_AntiKt4EMTopoJets	*shape and norm. uncertainties var. bgr.*
SysFT_EFF_extrapol_c_AntiKt2PV0TrackJets	SysMbbTTbarShapeOnly
SysFT_EFF_extrapol_c_AntiKt4EMTopoJets	SysMbbVVMEShapeOnly_WZ
truth tagging norm. uncert.	SysMbbVVMEShapeOnly_ZZ
SysVBFH01MF	SysMbbVVPSUEShapeOnly_WZ
SysVBFH01MP	SysMbbVVPSUEShapeOnly_ZZ
SysVBFH02MF	SysstopWtNorm
SysVBFH02MP	SysstopsNorm
SysVBFH11SFMF	SysstoptNorm
SysVBFH11SFMP	SysZZNorm
SysVBFH11SPMF	SysWWNorm
SysVBFH11SPMP	SysWZNorm
SysVBFH12MF	SysTTbarPTV
SysVBFH12MP	SysTTbarResVsMerged
SysggH01MF	**Normalistions**
SysggH01MP	ATLAS_norm_Whf
SysggH02MF	ATLAS_norm_Wl
SysggH02MP	ATLAS_norm_Zhf
SysggH11SFMF	ATLAS_norm_Zl
SysggH11SFMP	ATLAS_norm_ttbar
SysggH11SPMF	
SysggH11SPMP	
SysggH12MF	
SysggH12MP	

Table A.5.: First list of NPs used in the Run 1 $H \rightarrow$ inv combination except for the statistical uncertainties on the single bins of the final obversables used in the analyses.

Nuisance Parameter Name		
ATLAS_LUMI_2012	SysBTagC13Effic_Y2012_VjjInv	ATLAS_JET_EB_ZllInv
ATLAS_LUMI_2011_ZllInv	SysBTagC14Effic_Y2012_VjjInv	ATLAS_JET_EDR_ZllInv
Leptons	SysBTagCPythia8_Y2012_VjjInv	ATLAS_JET_EE_ZllInv
ATLAS_E_EFF_ZllInv	SysBTagCSherpa_Y2012_VjjInv	ATLAS_JET_EFLAVR_ZllInv
ATLAS_E_RES_ZllInv	SysBTagL0Effic_Y2012_VjjInv	ATLAS_JET_EFLAV_ZllInv
ATLAS_E_SCALE_ZllInv	SysBTagL1Effic_Y2012_VjjInv	ATLAS_JET_MU_ZllInv
ATLAS_M_EFF_ZllInv	SysBTagL2Effic_Y2012_VjjInv	ATLAS_JET_PUPT_ZllInv
ATLAS_M_RES_ID_ZllInv	SysBTagL3Effic_Y2012_VjjInv	ATLAS_JET_PV_ZllInv
ATLAS_M_RES_MS_ZllInv	SysBTagL4Effic_Y2012_VjjInv	ATLAS_JVF_ZllInv
ATLAS_fakeelecSF_VBF	SysBTagL5Effic_Y2012_VjjInv	ATLAS_PV_ZllInv
ATLAS_fakemuSF_VBF	SysBTagL6Effic_Y2012_VjjInv	SysJVF_Y2012_VjjInv
$E_{\mathbf{T}}^{\mathbf{miss}}$	SysBTagL7Effic_Y2012_VjjInv	SysJetEtaModel_VjjInv
SysMETResoSoftTerms_Y2012_VjjInv	SysBTagL8Effic_Y2012_VjjInv	SysJetFlavComp_Top_VjjInv
SysMETScaleSoftTerms_Y2012_VjjInv	SysBTagL9Effic_Y2012_VjjInv	SysJetFlavComp_VHVV_VjjInv
Flavour tagging	**Jets**	SysJetFlavComp_VjjInv
SysBTagB0Effic_Y2012_VjjInv	JESPileup_OffsetMu_Monojet	SysJetFlavComp_Wjets_VjjInv
SysBTagB1Effic_Y2012_VjjInv	JER	SysJetFlavComp_Zjets_VjjInv
SysBTagB2Effic_Y2012_VjjInv	JESFlavorResponse	SysJetFlavResp_Top_VjjInv
SysBTagB3Effic_Y2012_VjjInv	JESEtaIntercalibration_Modelling	SysJetFlavResp_VHVV_VjjInv
SysBTagB4Effic_Y2012_VjjInv	JESEffectiveNP_Modelling1	SysJetFlavResp_Wjets_VjjInv
SysBTagB5Effic_Y2012_VjjInv	JESFlavorComp	SysJetFlavResp_Zjets_VjjInv
SysBTagB6Effic_Y2012_VjjInv	JESEffectiveNP_Detector1_Monojet	SysJetMu_VjjInv
SysBTagB7Effic_Y2012_VjjInv	JESEffectiveNP_Modelling2_Monojet	SysJetNP1_Y2012_VjjInv
SysBTagB8Effic_Y2012_VjjInv	ATLAS_JER_ZllInv	SysJetNP2_Y2012_VjjInv
SysBTagB9Effic_Y2012_VjjInv	ATLAS_JES1_ZllInv	SysJetNP3_Y2012_VjjInv
SysBTagBPythia8_Y2012_VjjInv	ATLAS_JES2_ZllInv	SysJetNP4_Y2012_VjjInv
SysBTagBSherpa_Y2012_VjjInv	ATLAS_JES3_ZllInv	SysJetNonClos_VjjInv
SysBTagC0Effic_Y2012_VjjInv	ATLAS_JES4_ZllInv	SysJetFlavB_VjjInv
SysBTagC1Effic_Y2012_VjjInv	ATLAS_JES5_ZllInv	SysJetFlavResp_VjjInv
SysBTagC2Effic_Y2012_VjjInv	ATLAS_JES6_ZllInv	SysJetPilePt_Y2012_VjjInv
SysBTagC3Effic_Y2012_VjjInv	ATLAS_JES7_ZllInv	SysJetPileRho_Y2012_VjjInv
SysBTagC4Effic_Y2012_VjjInv	ATLAS_JES8_ZllInv	SysJetNPV_VjjInv
SysBTagC5Effic_Y2012_VjjInv	ATLAS_JES9_ZllInv	SysJetEtaStat_Y2012_VjjInv
SysBTagC6Effic_Y2012_VjjInv	ATLAS_JES10_ZllInv	
SysBTagC7Effic_Y2012_VjjInv	ATLAS_JES11_ZllInv	
SysBTagC8Effic_Y2012_VjjInv	ATLAS_JES12_ZllInv	
SysBTagC9Effic_Y2012_VjjInv	ATLAS_JES13_ZllInv	
SysBTagC10Effic_Y2012_VjjInv	ATLAS_JES14_ZllInv	
SysBTagC11Effic_Y2012_VjjInv	ATLAS_JES15_ZllInv	
SysBTagC12Effic_Y2012_VjjInv	ATLAS_JES16_ZllInv	

Table A.6.: Second list of NPs used in the Run 1 $H \rightarrow$ inv combination except for the statistical uncertainties on the single bins of the final obversables used in the analyses.

Nuisance Parameter Name		
V+Jets modelling	**Other backgrounds**	**Signal modelling**
SysWMbb_WbbORcc_VjjInv	SysMJ_J2_T0_L0_Y2012_VjjInv	pdf_unc
SysWMbb_WbcORbl_VjjInv	SysMJ_J2_T1_L0_Y2012_VjjInv	PartonShowering
SysWMbb_Wcl_VjjInv	SysMJ_J2_T2_L0_Y2012_VjjInv	HPt_VH
SysZMbb_ZbORc_VjjInv	SysMJ_J3_T0_L0_Y2012_VjjInv	SysHiggsNorm_VjjInv
SysZPtV_ZbORc_VjjInv	SysMJ_J3_T1_L0_Y2012_VjjInv	SysTheoryAccPDF_qqVH_VjjInv
SysZPtV_Zl_VjjInv	SysMJ_J3_T2_L0_Y2012_VjjInv	SysTheoryAcc_J2_qqVH_VjjInv
SysWPtV_J2_Whf_VjjInv	SysMJ_L2_Y2012_T0_VjjInv	SysTheoryAcc_J3_qqVH_VjjInv
SysWPtV_J3_Whf_VjjInv	SysMJ_L2_Y2012_T1_VjjInv	SysTheoryQCDscale_ggZH_VjjInv
SysWclNorm_J3_VjjInv	SysMJ_L2_Y2012_T2_Spctopemucr_VjjInv	SysTheoryQCDscale_qqVH_VjjInv
SysWhfNorm_J3_VjjInv	SysMJ_L2_Y2012_T2_VjjInv	SysTheory_VjjInv
SysZclNorm_J3_VjjInv	SysVVJetPDFAlphaPt_VjjInv	ATLAS_QCDscale_VBFH
SysZbbNorm_J3_VjjInv	SysVVJetScalePtST1_VjjInv	ATLAS_QCDscale_ggFH
SysWlNorm_J3_VjjInv	SysVVJetScalePtST2_VjjInv	QCD_Monojet
SysZlNorm_J3_VjjInv	SysVVMbb_WW_VjjInv	ktfac_Monojet
SysWbcWbbRatio_VjjInv	SysVVMbb_WZ_VjjInv	qfac_Monojet
SysWblWbbRatio_VjjInv	SysVVMbb_ZZ_VjjInv	HiggsPt_Monojet
SysWccWbbRatio_VjjInv	SysWtChanAcerMC_VjjInv	HiggsPt_VBF
SysZbcZbbRatio_VjjInv	SysWtChanPythiaHerwig_VjjInv	CJV_Monojet *(Central Jet Veto)*
SysZblZbbRatio_J2_VjjInv	SysSChanAcerMCPS_VjjInv	CJV_VBFH
SysZblZbbRatio_J3_VjjInv	SysSChanAcerMC_VjjInv	jetBin *(ggF+2jets in SR)*
SysZccZbbRatio_VjjInv	SysstopWtNorm_VjjInv	SysTheoryAccPS_VjjInv
ATLAS_WCR_2011_zinv_ZllInv	SysstopsNorm_VjjInv	QCDscale_VH0j_ZllInv
ATLAS_WCR_2012_zinv_ZllInv	SysstoptNorm_VjjInv	**Normalisations**
ATLAS_ZABCDCR_2011_zinv_ZllInv	SysTChanPtB2_VjjInv	norm_kV
ATLAS_ZABCDCR_2012_zinv_ZllInv	SysTopPt_VjjInv	mu_A12
ATLAS_WPDF_2012_VBF	SysTtbarMBBCont_VjjInv	mu_A25
ATLAS_ZPDF_2012_VBF	SysTtbarMetCont_VjjInv	ATLAS_norm_Wbb_VjjInv
ATLAS_SherpaQ2EWK_2012_VBF	SysttbarNorm_J3_VjjInv	ATLAS_norm_Wcl_VjjInv
ATLAS_SherpaQ2QCD_2012_VBF	ATLAS_ZZshape_Generator_2011_ZllInv	ATLAS_norm_Wl_VjjInv
(corr. for data MC disagreem.	ATLAS_ZZshape_Generator_2012_ZllInv	ATLAS_norm_Zbb_VjjInv
SysWDPhi_J2_Wcl_VjjInv	ATLAS_ZZshape_PDF_2011_ZllInv	ATLAS_norm_Zcl_VjjInv
SysWDPhi_J2_Whf_VjjInv	ATLAS_ZZshape_PDF_2012_ZllInv	ATLAS_norm_Zl_VjjInv
SysWDPhi_J2_Wl_VjjInv	ATLAS_ZZshape_Scale_2011_ZllInv	ATLAS_norm_ttbar_L0_VjjInv
SysWDPhi_J3_Wcl_VjjInv	ATLAS_ZZshape_Scale_2012_ZllInv	ATLAS_norm_ttbar_L1_VjjInv
SysWDPhi_J3_Whf_VjjInv	ATLAS_emuCR_eff_2011_zinv_ZllInv	ATLAS_norm_ttbar_L2_VjjInv
SysWDPhi_J3_Wl_VjjInv	ATLAS_emuCR_eff_2012_zinv_ZllInv	
SysZDPhi_J2_ZbORc_VjjInv	ATLAS_emuCR_kfac_2011_zinv_ZllInv	
SysZDPhi_J2_Zl_VjjInv	ATLAS_emuCR_kfac_2012_zinv_ZllInv	
SysZDPhi_J3_ZbORc_VjjInv	ATLAS_emuCR_stat_2011_zinv_ZllInv	
SysZDPhi_J3_Zl_VjjInv	ATLAS_emuCR_stat_2012_zinv_ZllInv	
	QCDscale_VV_ZllInv	

B. Alternative Correlation Assumptions

The dependence of the results on the correlation model assumed is estimated by producing combined likelihood functions with alternative correlation scenarios and comparison of the computed limits. In case of the Run 2 $H \rightarrow$ inv combination discussed below, alternative correlation scenarios are considered for the JES, flavour tagging, and signal theory uncertainties. The impact on the result is quantified as absolute (signed) difference between the limit computed with the modified correlation assumption and the nominal limit, although such point-to-point comparisons represent only ad-hoc estimations of the systematic effect.

Run 2 Correlation Model

Jet energy scale uncertainties A cross-check studying the impact of a possible underestimation of correlations between the category based reduction and the strongly reduced set of JES uncertainties is performed. For each modified combined likelihood function, one of the three NPs from the strongly reduced set of JES NPs Table B.1 is correlated with one NP from the category based reduction Table B.2, resulting in $3 * 27 = 81$ different correlation scenarios. The `JET_GroupedNP_1` NP from the $V_{q\bar{q}}H$ search is left uncorrelated since it is found to be over-constrained, see Section 6.1. A study including anti-correlation of the `GroupedNP` and NP in the category based reduction is performed additionally since the direction of the NP relative to each other after the combination into grouped NP is not clear a-priori. This is done by flipping the sign of the `JET_GroupedNP` in the likelihood functions of the $V_{q\bar{q}}H$ and $Z_{\ell\bar{\ell}}H$ analyses. The largest effect on the observed (expected) limit for positive correlation is 0.008 for `JET_GroupedNP_3` and `JET_Pileup_OffsetMu` (0.002 for `JET_GroupedNP_1` and `JET_EffectiveNP_Modelling2`). For anti-correlation, the largest effect on the observed (expected) limit is 0.015 for `JET_GroupedNP_3` and `JET_EffectiveNP_Modelling2` (0.002 for `JET_GroupedNP_3` and `JET_EtaIntercalibration_Modelling`). The full results are shown in Table B.5.

Table B.1.: Strongly reduced set of JES uncertainties used for the correlation studies. The JVT and EtaIntercalibration uncertainties are excluded from this list as they are already correlated in the default combination.

Nuisance Parameter Name
JET_GroupedNP_1
JET_GroupedNP_2
JET_GroupedNP_3

Table B.2.: Category based reduced set of JES uncertainties used for the correlation studies. The JVT and EtaIntercalibrationNonClosure uncertainties are excluded from this list as they are already correlated in the default combination.

Nuisance Parameter Name	
JET_BJES_Response	JET_EtaIntercalibration_Modelling
JET_EffectiveNP_Detector1	JET_EtaIntercalibration_TotalStat
JET_EffectiveNP_Detector2	JET_Flavor_Composition
JET_EffectiveNP_Mixed1	JET_Flavor_Response
JET_EffectiveNP_Mixed2	JET_Pileup_OffsetMu
JET_EffectiveNP_Mixed3	JET_Pileup_OffsetNPV
JET_EffectiveNP_Modelling1	JET_Pileup_PtTerm
JET_EffectiveNP_Modelling2	JET_Pileup_RhoTopology
JET_EffectiveNP_Modelling3	JET_PunchThrough_MC15
JET_EffectiveNP_Modelling4	JET_SingleParticle_HighPt
JET_EffectiveNP_Statistical1	JET_EffectiveNP_Statistical5
JET_EffectiveNP_Statistical2	JET_EffectiveNP_Statistical6
JET_EffectiveNP_Statistical3	JET_EffectiveNP_Statistical7
JET_EffectiveNP_Statistical4	

Theoretical uncertainties The correlation assumptions concerning theoretical uncertainties is described in 6.1.1. To cross-check these decisions, combined likelihood functions are produced for four different correlation scenarios. The full results are shown in Table B.6.

- The PDF induced uncertainty on the $H \to$ inv signal acceptance in $V_{q\bar{q}}H$ might be sizeable. A cross-check is performed correlating this NP instead of the one describing the impact on the signal cross section with the PDF uncertainty on the signal in $Z_{\ell\bar{\ell}}H$. The resulting observed (expected) limit at 95% CL on $\mathcal{B}_{H\to\text{inv}}$ differ by 3×10^{-5} (7×10^{-6}) compared to the default combination.

- Similarly, the PDF induced uncertainty on the $E_{\text{T}}^{\text{miss}}$ shape in $V_{q\bar{q}}H$ is correlated with the PDF uncertainty on the signal in $Z_{\ell\bar{\ell}}H$. The resulting observed (expected) limit at 95% CL on $\mathcal{B}_{H\to\text{inv}}$ differ by 3×10^{-5} (3×10^{-5}) compared to the default combination.

- The QCD scale variation induced uncertainty on the $H \to$ inv signal acceptance in $V_{q\bar{q}}H$ might be sizeable as well. A cross-check is performed correlating this NP instead of the one describing the impact on the signal cross section with the QCD scale variation uncertainty on the signal in $Z_{\ell\bar{\ell}}H$. The resulting observed (expected) limit at 95% CL on $\mathcal{B}_{H\to\text{inv}}$ differ by 0.0002 (4×10^{-5}) compared to the default combination.

- The uncertainty on the $H \to$ inv signal due to modelling of the parton shower

with different MC generators/tunes between VBF and $V_{q\bar{q}}H$. The corresponding NP was pruned in $Z_{\ell\bar{\ell}}H$ as it was found to have negligible impact on the result. The resulting observed (expected) limit at 95% CL on $\mathcal{B}_{H\to\text{inv}}$ differ by 0.0003 (6×10^{-5}) compared to the default combination.

Flavour tagging uncertainties The correlation of flavour tagging uncertainties is described in Sec 6.1.1. The combined NP in $Z_{\ell\bar{\ell}}H$ are per default correlated with the zeroth Eigenvector in $V_{q\bar{q}}H$. This decision is justified by the fact that the Eigenvectors are ordered by their impact. Cross-checks are performed correlating the combined NP in $Z_{\ell\bar{\ell}}H$ Table B.3 with one of the other Eigenvectors in $V_{q\bar{q}}H$ at a time Table B.4 resulting in eight different correlation scenarios. The full results are shown in Table B.7. The extrapolation and extrapolation from charm NP are not split into Eigenvectors and are therefore nominally correlated between both channels. The largest difference arises when correlating the combined NP for light quarks in $Z_{\ell\bar{\ell}}H$ with the corresponding second Eigenvector in $V_{q\bar{q}}H$. The resulting observed (expected) limit at 95% CL on $\mathcal{B}_{H\to\text{inv}}$ differ by 0.0031 (0.0003) compared to the default combination. This study was performed before de-correlating over-constraint and largely pulled NP. The `FT_Eigen_B_0_AntiKt4EMTopoJets` from $V_{q\bar{q}}H$ is de-correlated in this procedure. A second study including anti-correlation of the combined and Eigenvector-split NP is performed. This is done by flipping the sign of the corresponding combined FT NP in the likelihood function of the $Z_{\ell\bar{\ell}}H$ analysis. Three different anti-correlation assumptions are tested since the zeroth `B` NP from $V_{q\bar{q}}H$ is not correlated and the effect of correlating the combined NP with other EV than the zeroth is small. Tested are anti-correlating the `C`, the `Light` and both combined NP in $Z_{\ell\bar{\ell}}H$ with the corresponding zeroth EV in $V_{q\bar{q}}H$. The largest effect is found for anti-correlating both NP and change the observed (expected) limit by 0.0030 (0.0002). All three results are shown in Table B.8.

Table B.3.: Combined flavour tagging NP in the $Z_{\ell\bar{\ell}}H$ analyses.

Nuisance Parameter Name
FT_B_systematics
FT_C_systematics
FT_Light_systematics
FT_extrapolation__1
FT_extrapolation_from_charm

Table B.4.: Flavour tagging NP splitted into Eigenvectors in the $V_{q\bar{q}}H$ analysis.

Nuisance Parameter Name	
FT_Eigen_B_0_AntiKt4EMTopoJets	FT_Eigen_Light_0_AntiKt4EMTopoJets
FT_Eigen_B_1_AntiKt4EMTopoJets	FT_Eigen_Light_1_AntiKt4EMTopoJets
FT_Eigen_B_2_AntiKt4EMTopoJets	FT_Eigen_Light_2_AntiKt4EMTopoJets
FT_Eigen_C_0_AntiKt4EMTopoJets	FT_Eigen_Light_3_AntiKt4EMTopoJets
FT_Eigen_C_1_AntiKt4EMTopoJets	FT_Eigen_Light_4_AntiKt4EMTopoJets
FT_Eigen_C_2_AntiKt4EMTopoJets	
FT_extrapolation_AntiKt4EMTopoJets	
FT_extrapolation_from_charm_AntiKt4EMTopoJets	

Summary The cross-check of JES NP correlation assumptions estimates an impact of at most 0.014 (0.005) on the observed (expected) exclusion limit on $\mathcal{B}_{H\to\text{inv}}$. Changes in the correlation model of flavour tagging and theoretical NP are found to impact the combined result even less. All studied modified correlation scenarios are found to change the limit on $\mathcal{B}_{H\to\text{inv}}$ negligibly compared to the combined systematic uncertainty on the result of 0.38 ($0.21^{+0.08}_{-0.06}$), computed with the asymptotic CL_s limit setting routine. The chosen correlation model for the combination of the 2015+2016 $H \to$ inv analyses is thus considered justified.

Run 1+2 Correlation Model

The correlation model for the Run 1 and Run 2 combination is described in 6.1.2.

In our correlation scheme described in Section 6.1.2, PDF uncertainties on the signal are not correlated in the combination due to different PDF sets used across runs. The VBF analyses estimate the impact of parton shower modelling uncertainty on the signal by comparing MC generators. The generators used differ between Run 1 and Run 2, thus a full correlation is not considered. To cross-check these decisions, workspaces are produced with three different correlation assumptions. The full results are shown in Table B.9. Tested are:

- A correlation of the PDF uncertainties on the $H \to$ inv signal between the correlated NP from the VBF and $Z_{\ell\bar{\ell}}H$ searches in Run 2, see 6.1.1, and the corresponding NP from the Run 1 VBF+Monojet analyses. The resulting observed (expected) limit at 95% CL on $\mathcal{B}_{H\to\text{inv}}$ differ by 0.0003 (0.0003) compared to the default combination.

- A correlation of the PDF uncertainties on the $H \to$ inv signal acceptance between the $V_{q\bar{q}}H$ Run 1 and Run 2 analyses. The resulting observed (expected) limit at 95% CL on $\mathcal{B}_{H\to\text{inv}}$ differ by 5×10^{-6} (4×10^{-6}) compared to the default combination.

- A correlation between the parton shower induced uncertainties on the $H \to$ inv signal between the VBF Run 1 and Run 2 analyses. The resulting observed (expected) limit at 95% CL on $\mathcal{B}_{H\to\text{inv}}$ differ by 0.0010 (0.0001) compared to the default combination.

- A correlation of the uncertainties due to QCD scale variations on the signal prediction in the $Z_{\ell\bar{\ell}}H$ searches of Run 1 and Run 2 is considered correlated by default, which is questionable given the differences in $\sqrt{s}$ and generator set-ups. Decorrelating the corresponding NP between Run 1 and 2 changes the observed (expected) limit at 95% CL on $\mathcal{B}_{H\to\text{inv}}$ by 5×10^{-5} (1×10^{-5}).

- Both the strong and weak JES correlation scenarios are adopted. The difference between both schemes in the expected branching ratio on $\mathcal{B}_{H\to\text{inv}}$ is found to be 0.0001. The strong correlation scheme results in the slightly weaker limit.

The impact of the different correlation assumptions on the limit on $\mathcal{B}_{H\to\text{inv}}$ are considerably less than the combined systematic uncertainty computed by the limit setting routine. The chosen correlation model between the Run 1 and Run 2 $H \to$ inv analyses is thus considered justified.

Numerical Values

Table B.5.: Summary of the JES correlation model cross-checks for the Run 2 combination. Considered are (anti-)correlation of the `JET_GroupedNP` 2 and 3 from $Z_{\ell\bar{\ell}}H$ and $V_{q\bar{q}}H$ with the category based reduced NP from VBF and (anti-)correlation of the `JET_GroupedNP_1` from $Z_{\ell\bar{\ell}}H$ with the category based reduced NP from VBF. Shown are the differences of the computed observed and expected limits to the nominal combination for correlation and anti-correlation.

Difference to nominal	Correlation		Anti-Correlation	
	observed	expected	observed	expected
NP_1 & BJES_Response	0.0000001	0.0000003	0.00000006	0.0000003
NP_1 & Detector1	-0.0004	0.0002	0.001	-0.0005
NP_1 & Detector2	-0.00008	0.00008	0.0009	-0.0004
NP_1 & Mixed1	0.001	-0.0002	-0.0008	-0.0002
NP_1 & Mixed2	0.0008	-0.0004	-0.00009	0.0001
NP_1 & Mixed3	-0.0001	-0.00002	0.0007	-0.0004
NP_1 & Modelling1	-0.004	-0.00008	0.005	0.0009
NP_1 & Modelling2	0.007	0.002	-0.00008	-0.0005
NP_1 & Modelling3	0.0004	-0.0009	-0.00002	0.0004
NP_1 & Modelling4	0.00002	-0.0001	0.00007	0.0001
NP_1 & Statistical1	-0.00009	-0.0008	-0.001	0.0006
NP_1 & Statistical2	-0.001	0.0004	0.0004	-0.001
NP_1 & Statistical3	0.0006	-0.0005	-0.00007	0.0001
NP_1 & Statistical4	-0.000006	0.00005	0.0003	-0.0007
NP_1 & Statistical5	0.0001	0.00009	0.0005	-0.0003
NP_1 & Statistical6	0.0004	-0.0004	0.0003	0.0001
NP_1 & Statistical7	-0.0001	0.0002	0.0009	-0.0003
NP_1 & EtaIntercal_Modelling	-0.0001	0.0008	-0.0002	-0.0005
NP_1 & EtaIntercal_TotalStat	0.00008	0.000002	-0.0002	0.0003
NP_1 & Flavor_Composition	-0.0007	0.0003	0.003	-0.0008
NP_1 & Flavor_Response	0.002	-0.0008	-0.0002	0.002
NP_1 & Pileup_OffsetMu	0.0008	-0.001	-0.004	-0.0002
NP_1 & Pileup_OffsetNPV	-0.004	0.0005	-0.001	-0.00006
NP_1 & Pileup_PtTerm	0.002	0.001	-0.002	-0.0009
NP_1 & Pileup_RhoTopology	-0.002	-0.00003	0.003	0.001
NP_1 & PunchThrough_MC15	-0.000009	0.000002	0.00006	-0.00003
NP_1 & SingleParticle_HighPt	0.0000008	0.0000001	0.0000002	0.0000001

Difference to nominal	Correlation		Anti-Correlation	
	observed	expected	observed	expected
NP_2 & BJES_Response	0.000003	0.000005	0.000002	0.000002
NP_2 & Detector1	0.001	-0.0004	-0.0006	0.00006
NP_2 & Detector2	0.0008	-0.0004	-0.0002	0.00006
NP_2 & Mixed1	-0.002	-0.0007	0.001	-0.0002
NP_2 & Mixed2	-0.0002	0.00007	0.0007	-0.0004
NP_2 & Mixed3	0.0007	-0.0003	-0.0001	-0.00002
NP_2 & Modelling1	0.005	0.001	-0.004	-0.0004
NP_2 & Modelling2	0.00003	-0.0004	0.006	0.002
NP_2 & Modelling3	-0.0006	0.0002	0.0005	-0.0007
NP_2 & Modelling4	-0.0003	-0.000007	0.0002	-0.00002
NP_2 & Statistical1	-0.001	0.0004	0.0003	-0.0005
NP_2 & Statistical2	0.0006	-0.0007	-0.002	0.0002
NP_2 & Statistical3	-0.0002	0.00007	0.0007	-0.0004
NP_2 & Statistical4	0.0005	-0.0006	0.00003	0.0001
NP_2 & Statistical5	0.0005	-0.0003	-0.00002	0.00003
NP_2 & Statistical6	0.0003	0.0001	0.0003	-0.0004
NP_2 & Statistical7	0.0007	-0.0004	-0.0004	0.0001
NP_2 & EtaIntercal_Modelling	-0.004	-0.002	-0.00003	0.0007
NP_2 & EtaIntercal_TotalStat	-0.0007	0.00001	0.0001	-0.000003
NP_2 & Flavor_Composition	0.001	-0.001	-0.0003	0.0004
NP_2 & Flavor_Response	-0.0006	0.0009	0.0007	-0.001
NP_2 & Pileup_OffsetMu	-0.006	-0.001	0.0004	-0.002
NP_2 & Pileup_OffsetNPV	-0.0006	-0.0003	-0.004	-0.0001
NP_2 & Pileup_PtTerm	-0.004	-0.002	0.002	0.001
NP_2 & Pileup_RhoTopology	0.003	0.001	-0.003	-0.0005
NP_2 & PunchThrough_MC15	0.00005	-0.00002	-0.000005	0.000005
NP_2 & SingleParticle_HighPt	0.000003	0.000004	0.000001	0.000003

Difference to nominal	Correlation		Anti-Correlation	
	observed	expected	observed	expected
NP_3 & BJES_Response	0.000002	0.000005	0.000001	0.000003
NP_3 & Detector1	0.002	-0.0001	-0.001	-0.00003
NP_3 & Detector2	0.001	-0.0001	-0.00007	0.00007
NP_3 & Mixed1	-0.004	-0.001	0.003	0.0005
NP_3 & Mixed2	-0.0003	0.00006	0.001	-0.0002
NP_3 & Mixed3	0.002	-0.00003	0.00007	0.00004
NP_3 & Modelling1	0.006	0.002	-0.008	-0.002
NP_3 & Modelling2	0.004	0.0005	0.01	0.00005
NP_3 & Modelling3	-0.001	0.0002	0.003	-0.0004
NP_3 & Modelling4	-0.001	-0.0001	0.0009	0.00007
NP_3 & Statistical1	-0.002	0.0005	0.003	-0.0003
NP_3 & Statistical2	0.004	-0.0003	-0.003	0.0002
NP_3 & Statistical3	-0.0003	0.0001	0.002	-0.0002
NP_3 & Statistical4	0.002	-0.0004	0.0006	0.0002
NP_3 & Statistical5	0.001	-0.00009	-0.00008	0.00009
NP_3 & Statistical6	0.0007	0.0003	0.0006	-0.0003
NP_3 & Statistical7	0.0007	-0.0002	-0.001	0.000007
NP_3 & EtaIntercal_Modelling	-0.002	0.0003	0.003	0.002
NP_3 & EtaIntercal_TotalStat	-0.002	-0.0003	-0.0003	-0.00008
NP_3 & Flavor_Composition	-0.002	0.0002	0.0004	0.0009
NP_3 & Flavor_Response	-0.002	0.001	-0.001	0.0002
NP_3 & Pileup_OffsetMu	-0.008	-0.002	0.006	-0.0002
NP_3 & Pileup_OffsetNPV	-0.003	-0.0005	-0.008	-0.0008
NP_3 & Pileup_PtTerm	-0.004	-0.002	0.004	0.002
NP_3 & Pileup_RhoTopology	0.002	-0.0004	-0.007	-0.002
NP_3 & PunchThrough_MC15	0.00008	-0.00001	0.000009	0.000007
NP_3 & SingleParticle_HighPt	0.000001	0.000004	0.000001	0.000003

Table B.6.: Summary of the signal theory correlation model cross-checks for the Run 2 combination. Shown are the differences of the computed observed and expected limits to the nominal combination as absolute values and relative to the nominal limit.

Difference to nominal	Absolute		Relative	
	observed	expected	observed	expected
PDF Acceptance	0.00003	0.000007	0.00008	0.00003
PDF Shape	0.00003	0.00003	0.00008	0.0001
Parton Shower	0.0003	0.00006	0.0008	0.0003
QCD Acceptance ZH+VH	0.0002	0.00004	0.0006	0.0002

Table B.7.: Summary of the flavour tagging correlation model cross-checks for the Run 2 combination. Shown are the differences of the computed observed and expected limits to the nominal combination as absolute values and relative to the nominal limit.

Difference to nominal	Absolute		Relative	
	observed	expected	observed	expected
FT_Eigen_B_1	0.0007	0.0001	0.002	0.0005
FT_Eigen_B_2	0.0005	0.00007	0.001	0.0003
FT_Eigen_C_1	0.00009	0.00002	0.0002	0.00008
FT_Eigen_C_2	0.0005	0.00004	0.001	0.0002
FT_Eigen_Light_1	-0.0003	0.00006	-0.0009	0.0003
FT_Eigen_Light_2	-0.003	-0.0003	-0.008	-0.001
FT_Eigen_Light_3	-0.0008	-0.00002	-0.002	-0.00008
FT_Eigen_Light_4	0.0003	0.0002	0.0007	0.0008

Table B.8.: Summary of the flavour tagging anti-correlation model cross-checks including the de-correlation of overconstraint and/or highly pulled NP resulting in not correlating `SysFT_Eigen_B_0_AntiKt4EMTopoJets_Y2015` from $V_{q\bar{q}}H$. Considered are anti-correlation of `FT_C_systematics`, `FT_Light_systematics` as well as both from $Z_{\ell\bar{\ell}}H$ with the corresponding zeroth EV NP from $V_{q\bar{q}}H$. Shown are the differences of the computed observed and expected limits to the nominal combination.

	observed	expected
FT_C_systematics	-0.0006	-0.00007
FT_Light_systematics	-0.0024	-0.00017
both	-0.0030	-0.00024

Table B.9.: Summary of the correlation model cross-checks for the Run 1+2 combination. Shown are the differences of the computed observed and expected limits to the nominal combination as absolute values and relative to the nominal limit.

Difference to nominal	Absolute		Relative	
	observed	expected	observed	expected
PDF VBF+$Z_{\ell\bar{\ell}}H$ VBF+Monojet	-0.0003	-0.0003	-0.001	-0.002
PDF acceptance VH	4×10^{-6}	4×10^{-6}	2×10^{-5}	2.5×10^{-5}
PS VBF	0.001	0.0001	0.004	0.0007

C. Nuisance Parameter Categorisation

The categorisation of the different sources of systematic uncertainty used in Sections 6.2.4 and 6.3.5. Correlated NP are shown first without a channel ending. Uncertainties correlated between Run 1 and Run 2 are shown in the Run 2 column, and are marked with an asterisk ($\star$). Uncertainties from a specific channel that are not correlated are shown with the corresponding ending and are ordered by rising sensitivity of the channel ($V_{q\bar{q}}H \rightarrow Z_{\ell\bar{\ell}}H \rightarrow$ VBF). The Monte-Carlo-Statistics category that contains all `gamma_stat` and `MCStat` NP is not separately depicted.

Table C.1.: The NP from the Run 1 and Run 2 $H \rightarrow$ inv analyses that contribute to the Luminosity category in the breakdown of systematic uncertainties.

Luminosity	
Run 1	Run 2
ATLAS_LUMI_2012	ATLAS_LUMI
ATLAS_LUMI_2011_ZllInv	

Table C.2.: The NP from the Run 1 and Run 2 $H \rightarrow$ inv analyses that contribute to the Leptons category in the breakdown of systematic uncertainties.

Leptons	
Run 1	Run 2
ATLAS_E_EFF_ZllInv	EG_RESOLUTION
ATLAS_E_RES_ZllInv	EG_SCALE
ATLAS_E_SCALE_ZllInv	EL_EFF_ID
ATLAS_M_EFF_ZllInv	EL_EFF_Iso
ATLAS_M_RES_ID_ZllInv	EL_EFF_Reco
ATLAS_M_RES_MS_ZllInv	EL_EFF_Trigger
ATLAS_fakeelecSF_VBF	MUON_EFF_STAT
ATLAS_fakemuSF_VBF	MUON_EFF_SYS
	MUON_EFF_TrigStat
	MUON_EFF_TrigSys
	MUON_ID
	MUON_ISO_STAT
	MUON_ISO_SYS
	MUON_MS
	MUON_SAGITTA_RESBIAS
	MUON_SAGITTA_RHO
	MUON_SCALE
	MUON_TTVA_STAT
	MUON_TTVA_SYS
	antiIDSF_VBF

Table C.3.: The NP from the Run 1 and Run 2 $H \rightarrow$ inv analyses that contribute to the $E_{\mathrm{T}}^{\mathrm{miss}}$ Soft Term category in the breakdown of systematic uncertainties.

$E_{\mathrm{T}}^{\mathrm{miss}}$ soft term	
Run 1	Run 2
SysMETResoSoftTerms_Y2012_VjjInv	MET_SoftTrk_ResoPara
SysMETScaleSoftTerms_Y2012_VjjInv	MET_SoftTrk_ResoPerp
	MET_SoftTrk_Scale
	MET_Trig_Syst
	SysMET_JetTrk_Scale_Y2015_VH
	SysMET_SoftTrk_ResoPara_Y2015_VH
	SysMET_SoftTrk_Scale_Y2015_VH

Table C.4.: The NP from the Run 1 and Run 2 $H \rightarrow$ inv analyses that contribute to the Jets category in the breakdown of systematic uncertainties.

Jets	
Run 1	Run 2
JER	jet_bjes_response ($\star$)
JESFlavorResponse	JET_EtaModelling ($\star$)
ATLAS_JER_ZllInv	JET_EtaStat ($\star$)
ATLAS_JES1_ZllInv	JET_FlavorComp ($\star$)
ATLAS_JES2_ZllInv	JET_FlavorResp ($\star$)
ATLAS_JES3_ZllInv	JET_Modelling1 ($\star$)
ATLAS_JES4_ZllInv	JET_Modelling2 ($\star$)
ATLAS_JES5_ZllInv	JET_NPV ($\star$)
ATLAS_JES6_ZllInv	JET_PileOffsetMu ($\star$)
ATLAS_JES7_ZllInv	JET_PilePt ($\star$)
ATLAS_JES8_ZllInv	JET_PileRho ($\star$)
ATLAS_JES9_ZllInv	JET_Detector1 ($\star$)
ATLAS_JES10_ZllInv	JET_EtaIntercal
ATLAS_JES11_ZllInv	JET_GroupedNP_1
ATLAS_JES12_ZllInv	JET_GroupedNP_2
ATLAS_JES13_ZllInv	JET_GroupedNP_3
ATLAS_JES14_ZllInv	JET_JER
ATLAS_JES15_ZllInv	JET_JvtEff
ATLAS_JES16_ZllInv	SysJET_JER_SINGLE_NP_Y2015_VH
ATLAS_JET_EB_ZllInv	SysJET_SR1_JET_GroupedNP_1_Y2015_VH
ATLAS_JET_EDR_ZllInv	SysFATJET_JER_Y2015_VH
ATLAS_JET_EE_ZllInv	SysFATJET_JMR_Y2015_VH
ATLAS_JET_EFLAVR_ZllInv	SysFATJET_Weak_JET_Rtrk_Baseline_D2Beta1_Y2015_VH
ATLAS_JET_EFLAV_ZllInv	SysFATJET_Weak_JET_Rtrk_Baseline_pT_Y2015_VH
ATLAS_JET_MU_ZllInv	SysFATJET_Weak_JET_Rtrk_Modelling_D2Beta1_Y2015_VH
ATLAS_JET_PUPT_ZllInv	SysFATJET_Weak_JET_Rtrk_Modelling_pT_Y2015_VH
ATLAS_JET_PV_ZllInv	SysFATJET_Weak_JET_Rtrk_Tracking_D2Beta1_Y2015_VH
ATLAS_JVF_ZllInv	SysFATJET_Weak_JET_Rtrk_Tracking_pT_Y2015_VH
ATLAS_PV_ZllInv	JET_EffectiveNP_Detector2_VBF
SysJVF_Y2012_VjjInv	JET_EffectiveNP_Mixed1_VBF
SysJetEtaModel_VjjInv	JET_EffectiveNP_Mixed2_VBF
SysJetFlavComp_Top_VjjInv	JET_EffectiveNP_Mixed3_VBF
SysJetFlavComp_VHVV_VjjInv	JET_EffectiveNP_Modelling3_VBF
SysJetFlavComp_VjjInv	JET_EffectiveNP_Modelling4_VBF
SysJetFlavComp_Wjets_VjjInv	JET_EffectiveNP_Statistical1_VBF
SysJetFlavComp_Zjets_VjjInv	JET_EffectiveNP_Statistical2_VBF
SysJetFlavResp_Top_VjjInv	JET_EffectiveNP_Statistical3_VBF
SysJetFlavResp_VHVV_VjjInv	JET_EffectiveNP_Statistical4_VBF
SysJetFlavResp_Wjets_VjjInv	JET_EffectiveNP_Statistical5_VBF
SysJetFlavResp_Zjets_VjjInv	JET_EffectiveNP_Statistical6_VBF
SysJetMu_VjjInv	JET_EffectiveNP_Statistical7_VBF
SysJetNP1_Y2012_VjjInv	JET_PunchThrough_MC15_VBF
SysJetNP2_Y2012_VjjInv	JET_SingleParticle_HighPt_VBF
SysJetNP3_Y2012_VjjInv	
SysJetNP4_Y2012_VjjInv	
SysJetNonClos_VjjInv	

Table C.5.: The NP from the Run 1 and Run 2 $H \rightarrow$ inv analyses that contribute to the Flavour Tagging category in the breakdown of systematic uncertainties.

Flavour Tagging	
Run 1	Run 2
SysBTagB0Effic_Y2012_VjjInv	FT_EFF_B
SysBTagB1Effic_Y2012_VjjInv	FT_EFF_C
SysBTagB2Effic_Y2012_VjjInv	FT_EFF_Light
SysBTagB3Effic_Y2012_VjjInv	FT_EFF_extrapol
SysBTagB4Effic_Y2012_VjjInv	FT_EFF_extrapol_charm
SysBTagB5Effic_Y2012_VjjInv	SysFT_EFF_Eigen_B_0_AntiKt2PV0TrackJets_Y2015_VH
SysBTagB6Effic_Y2012_VjjInv	SysFT_EFF_Eigen_B_0_AntiKt4EMTopoJets_Y2015_VH
SysBTagB7Effic_Y2012_VjjInv	SysFT_EFF_Eigen_B_1_AntiKt2PV0TrackJets_Y2015_VH
SysBTagB8Effic_Y2012_VjjInv	SysFT_EFF_Eigen_B_1_AntiKt4EMTopoJets_Y2015_VH
SysBTagB9Effic_Y2012_VjjInv	SysFT_EFF_Eigen_B_2_AntiKt2PV0TrackJets_Y2015_VH
SysBTagBPythia8_Y2012_VjjInv	SysFT_EFF_Eigen_B_2_AntiKt4EMTopoJets_Y2015_VH
SysBTagBSherpa_Y2012_VjjInv	SysFT_EFF_Eigen_C_0_AntiKt2PV0TrackJets_Y2015_VH
SysBTagC0Effic_Y2012_VjjInv	SysFT_EFF_Eigen_C_1_AntiKt2PV0TrackJets_Y2015_VH
SysBTagC1Effic_Y2012_VjjInv	SysFT_EFF_Eigen_C_1_AntiKt4EMTopoJets_Y2015_VH
SysBTagC2Effic_Y2012_VjjInv	SysFT_EFF_Eigen_C_2_AntiKt2PV0TrackJets_Y2015_VH
SysBTagC3Effic_Y2012_VjjInv	SysFT_EFF_Eigen_C_2_AntiKt4EMTopoJets_Y2015_VH
SysBTagC4Effic_Y2012_VjjInv	SysFT_EFF_Eigen_C_3_AntiKt2PV0TrackJets_Y2015_VH
SysBTagC5Effic_Y2012_VjjInv	SysFT_EFF_Eigen_Light_0_AntiKt2PV0TrackJets_Y2015_VH
SysBTagC6Effic_Y2012_VjjInv	SysFT_EFF_Eigen_Light_1_AntiKt2PV0TrackJets_Y2015_VH
SysBTagC7Effic_Y2012_VjjInv	SysFT_EFF_Eigen_Light_1_AntiKt4EMTopoJets_Y2015_VH
SysBTagC8Effic_Y2012_VjjInv	SysFT_EFF_Eigen_Light_2_AntiKt2PV0TrackJets_Y2015_VH
SysBTagC9Effic_Y2012_VjjInv	SysFT_EFF_Eigen_Light_2_AntiKt4EMTopoJets_Y2015_VH
SysBTagC10Effic_Y2012_VjjInv	SysFT_EFF_Eigen_Light_3_AntiKt2PV0TrackJets_Y2015_VH
SysBTagC11Effic_Y2012_VjjInv	SysFT_EFF_Eigen_Light_3_AntiKt4EMTopoJets_Y2015_VH
SysBTagC12Effic_Y2012_VjjInv	SysFT_EFF_Eigen_Light_4_AntiKt2PV0TrackJets_Y2015_VH
SysBTagC13Effic_Y2012_VjjInv	SysFT_EFF_Eigen_Light_4_AntiKt4EMTopoJets_Y2015_VH
SysBTagC14Effic_Y2012_VjjInv	SysFT_EFF_extrapolation_AntiKt2PV0TrackJets_Y2015_VH
SysBTagCPythia8_Y2012_VjjInv	SysFT_EFF_extrapolation_from_charm_AntiKt2PV0TrackJets_Y2015_VH
SysBTagCSherpa_Y2012_VjjInv	SysVBFH01MF_VH
SysBTagL0Effic_Y2012_VjjInv	SysVBFH01MP_VH
SysBTagL1Effic_Y2012_VjjInv	SysVBFH02MF_VH
SysBTagL2Effic_Y2012_VjjInv	SysVBFH02MP_VH
SysBTagL3Effic_Y2012_VjjInv	SysVBFH11SFMF_VH
SysBTagL4Effic_Y2012_VjjInv	SysVBFH11SFMP_VH
SysBTagL5Effic_Y2012_VjjInv	SysVBFH11SPMF_VH
SysBTagL6Effic_Y2012_VjjInv	SysVBFH11SPMP_VH
SysBTagL7Effic_Y2012_VjjInv	SysVBFH12MF_VH
SysBTagL8Effic_Y2012_VjjInv	SysVBFH12MP_VH
SysBTagL9Effic_Y2012_VjjInv	SysggH01MF_VH
	SysggH01MP_VH
	SysggH02MF_VH
	SysggH02MP_VH
	SysggH11SFMF_VH
	SysggH11SFMP_VH
	SysggH11SPMF_VH
	SysggH11SPMP_VH
	SysggH12MF_VH
	SysggH12MP_VH

Table C.6.: The NP from the Run 1 and Run 2 $H \rightarrow$ inv analyses that contribute to the V+Jets category in the breakdown of systematic uncertainties.

V+jets modelling		
Run 1	Run 2	
SysWMbb_WbbORcc_VjjInv	SysMbbWShapeOnly_Y2015_VH	
SysWMbb_WbcORbl_VjjInv	SysMbbZShapeOnly_Y2015_VH	
SysWMbb_Wcl_VjjInv	SysWPtV_Y2015_VH	
SysZMbb_ZbORc_VjjInv	SysWbcWbbRatio_VH	
SysZPtV_ZbORc_VjjInv	SysWblWbbRatio_VH	
SysZPtV_Zl_VjjInv	SysWccWbbRatio_VH	
SysWPtV_J2_Whf_VjjInv	SysWclNorm_VH	
SysWPtV_J3_Whf_VjjInv	SysWjetsResVsMerged_VH	
SysWclNorm_J3_VjjInv	SysZPtV_Y2015_VH	
SysWhfNorm_J3_VjjInv	SysZbcZbbRatio_VH	
SysZclNorm_J3_VjjInv	SysZblZbbRatio_VH	
SysZbbNorm_J3_VjjInv	SysZccZbbRatio_VH	
SysWlNorm_J3_VjjInv	SysZclNorm_VH	
SysZlNorm_J3_VjjInv	SysZjetsResVsMerged_VH	
SysWbcWbbRatio_VjjInv	Wjets_Stat_ZH	
SysWblWbbRatio_VjjInv	Wjets_Sys_ZH	
SysWccWbbRatio_VjjInv	Zjets_ABCD_Shape_ee_ZH	
SysZbcZbbRatio_VjjInv	Zjets_ABCD_Shape_mm_ZH	
SysZblZbbRatio_J2_VjjInv	Zjets_ABCD_Stat_ee_ZH	
SysZblZbbRatio_J3_VjjInv	Zjets_ABCD_Stat_mm_ZH	
SysZccZbbRatio_VjjInv	Zjets_ABCD_Sys_ZH	
SysWDPhi_J2_Wcl_VjjInv	EWK_W-ckkw1_VBF	QCD_W-ckkw1_VBF
SysWDPhi_J2_Whf_VjjInv	EWK_W-ckkw2_VBF	QCD_W-ckkw2_VBF
SysWDPhi_J2_Wl_VjjInv	EWK_W-ckkw3_VBF	QCD_W-ckkw3_VBF
SysWDPhi_J3_Wcl_VjjInv	EWK_W-fac1_VBF	QCD_W-fac1_VBF
SysWDPhi_J3_Whf_VjjInv	EWK_W-fac2_VBF	QCD_W-fac2_VBF
SysWDPhi_J3_Wl_VjjInv	EWK_W-fac3_VBF	QCD_W-fac3_VBF
SysZDPhi_J2_ZbORc_VjjInv	EWK_W-pdf1_VBF	QCD_W-pdf1_VBF
SysZDPhi_J2_Zl_VjjInv	EWK_W-pdf2_VBF	QCD_W-pdf2_VBF
SysZDPhi_J3_ZbORc_VjjInv	EWK_W-pdf3_VBF	QCD_W-pdf3_VBF
SysZDPhi_J3_Zl_VjjInv	EWK_W-qsf1_VBF	QCD_W-qsf1_VBF
ATLAS_WCR_2011_zinv_ZllInv	EWK_W-qsf2_VBF	QCD_W-qsf2_VBF
ATLAS_WCR_2012_zinv_ZllInv	EWK_W-qsf3_VBF	QCD_W-qsf3_VBF
ATLAS_ZABCDCR_2011_zinv_ZllInv	EWK_Z-ckkw1_VBF	QCD_Z-ckkw1_VBF
ATLAS_ZABCDCR_2012_zinv_ZllInv	EWK_Z-ckkw2_VBF	QCD_Z-ckkw2_VBF
ATLAS_WPDF_2012_VBF	EWK_Z-ckkw3_VBF	QCD_Z-ckkw3_VBF
ATLAS_ZPDF_2012_VBF	EWK_Z-fac1_VBF	QCD_Z-fac1_VBF
ATLAS_SherpaQ2EWK_2012_VBF	EWK_Z-fac2_VBF	QCD_Z-fac2_VBF
ATLAS_SherpaQ2QCD_2012_VBF	EWK_Z-fac3_VBF	QCD_Z-fac3_VBF
	EWK_Z-pdf1_VBF	QCD_Z-pdf1_VBF
	EWK_Z-pdf2_VBF	QCD_Z-pdf2_VBF
	EWK_Z-pdf3_VBF	QCD_Z-pdf3_VBF
	EWK_Z-qsf1_VBF	QCD_Z-qsf1_VBF
	EWK_Z-qsf2_VBF	QCD_Z-qsf2_VBF
	EWK_Z-qsf3_VBF	QCD_Z-qsf3_VBF

Table C.7.: The NP from the Run 1 and Run 2 $H \rightarrow$ inv analyses that contribute to the other backgrounds category in the breakdown of systematic uncertainties.

Other backgrounds modelling	
Run 1	Run 2
SysMJ_J2_T0_L0_Y2012_VjjInv	QCD_scale_VV ($\star$)
SysMJ_J2_T1_L0_Y2012_VjjInv	SysMJ_Shape0mergedMassFail_Y2015_VH
SysMJ_J2_T2_L0_Y2012_VjjInv	SysMJ_Shape0mergedMassPass_Y2015_VH
SysMJ_J3_T0_L0_Y2012_VjjInv	SysMJ_Shape0resolvedMassFail_Y2015_VH
SysMJ_J3_T1_L0_Y2012_VjjInv	SysMJ_Shape0resolvedMassPass_Y2015_VH
SysMJ_J3_T2_L0_Y2012_VjjInv	SysMJ_Shape1mergedMassFail_Y2015_VH
SysMJ_L2_Y2012_T0_VjjInv	SysMJ_Shape1mergedMassPass_Y2015_VH
SysMJ_L2_Y2012_T1_VjjInv	SysMJ_Shape1resolvedMassFail_Y2015_VH
SysMJ_L2_Y2012_T2_Spctopemucr_VjjInv	SysMJ_Shape1resolvedMassPass_Y2015_VH
SysMJ_L2_Y2012_T2_VjjInv	SysMJ_Shape2mergedMassFail_Y2015_VH
SysVVJetPDFAlphaPt_VjjInv	SysMJ_Shape2mergedMassPass_Y2015_VH
SysVVJetScalePtST1_VjjInv	SysMJ_Shape2resolvedMassFail_Y2015_VH
SysVVJetScalePtST2_VjjInv	SysMJ_Shape2resolvedMassPass_Y2015_VH
SysVVMbb_WW_VjjInv	Sysmultijet0mergedMassFailNorm_VH
SysVVMbb_WZ_VjjInv	Sysmultijet0mergedMassPassNorm_VH
SysVVMbb_ZZ_VjjInv	Sysmultijet0resolvedMassFailNorm_VH
SysWtChanAcerMC_VjjInv	Sysmultijet0resolvedMassPassNorm_VH
SysWtChanPythiaHerwig_VjjInv	Sysmultijet1mergedMassFailNorm_VH
SysSChanAcerMCPS_VjjInv	Sysmultijet1mergedMassPassNorm_VH
SysSChanAcerMC_VjjInv	Sysmultijet1resolvedMassFailNorm_VH
SysstopWtNorm_VjjInv	Sysmultijet1resolvedMassPassNorm_VH
SysstopsNorm_VjjInv	Sysmultijet2mergedMassFailNorm_VH
SysstoptNorm_VjjInv	Sysmultijet2mergedMassPassNorm_VH
SysTChanPtB2_VjjInv	Sysmultijet2resolvedMassFailNorm_VH
SysTopPt_VjjInv	Sysmultijet2resolvedMassPassNorm_VH
SysTtbarMBBCont_VjjInv	SysWWNorm_VH
SysTtbarMetCont_VjjInv	SysWZNorm_VH
SysttbarNorm_J3_VjjInv	SysZZNorm_VH
ATLAS_ZZshape_Generator_2011_ZllInv	SysMbbVVMEShapeOnly_WZ_VH
ATLAS_ZZshape_Generator_2012_ZllInv	SysMbbVVMEShapeOnly_ZZ_VH
ATLAS_ZZshape_PDF_2011_ZllInv	SysMbbVVPSUEShapeOnly_WZ_VH
ATLAS_ZZshape_PDF_2012_ZllInv	SysMbbVVPSUEShapeOnly_ZZ_VH
ATLAS_ZZshape_Scale_2011_ZllInv	SysMbbTTbarShapeOnly_VH
ATLAS_ZZshape_Scale_2012_ZllInv	SysTTbarPTV_VH
ATLAS_emuCR_eff_2011_zinv_ZllInv	SysTTbarResVsMerged_VH
ATLAS_emuCR_eff_2012_zinv_ZllInv	SysstopWtNorm_VH
ATLAS_emuCR_kfac_2011_zinv_ZllInv	SysstopsNorm_VH
ATLAS_emuCR_kfac_2012_zinv_ZllInv	SysstoptNorm_VH
ATLAS_emuCR_stat_2011_zinv_ZllInv	OtherTheo_ZH
ATLAS_emuCR_stat_2012_zinv_ZllInv	WZScaleInEff_ZH
	WZScaleStat_ZH
	WZScaleSys_ZH
	ATLAS_pdf_qq_ZH
	ggZZTheo_ZH
	emu_Shape_ZH
	emu_Stat_ZH
	emu_Sys_ZH

Table C.8.: The NP from the Run 1 and Run 2 $H \rightarrow$ inv analyses that contribute to the signal category in the breakdown of systematic uncertainties.

Signal modelling	
Run 1	Run 2
pdf_unc	vbf_jetbin ($\star$)
PartonShowering	QCD_Scale_SigXsec ($\star$)
HPt_VH	PS_VH ($\star$)
SysHiggsNorm_VjjInv	PDF_SigXsec
SysTheoryAccPDF_qqVH_VjjInv	SysVHinvPDFAcc_VH
SysTheoryAcc_J2_qqVH_VjjInv	SysVHinvPDFShape_VH
SysTheoryAcc_J3_qqVH_VjjInv	SysVHinvPSTunesShape_VH
SysTheoryQCDscale_ggZH_VjjInv	SysVHinvQCDscaleAcc_VH
SysTheoryQCDscale_qqVH_VjjInv	SysggHinvPDFAcc_VH
SysTheory_VjjInv	SysggHinvPDFshape_VH
ATLAS_QCDscale_VBFH	SysggHinvPSTunesAcc_VH
ATLAS_QCDscale_ggFH	SysggHinvPSTunesshape_VH
QCD_Monojet	SysggHinvQCDscaleAcc_VH
ktfac_Monojet	SysggHinvXSPDF_VH
qfac_Monojet	EW_pTZ_ZH
HiggsPt_Monojet	HiggsPS_VBF
HiggsPt_VBF	VBF_uncert_VBF
CJV_Monojet	
CJV_VBFH	

Table C.9.: The NP from the Run 1 and Run 2 $H \rightarrow$ inv analyses that contribute to the Experimental category in the breakdown of systematic uncertainties.

Experimental	
Run 1	Run 2
All Luminosity uncertainties, see Table C.1	
All Lepton uncertainties, see Table C.2	
All $E_{\mathrm{T}}^{\mathrm{miss}}$ Soft Term uncertainties, see Table C.3	
All Jet uncertainties, see Table C.4	
All Flavour tagging uncertainties, see Table C.5	
V+Jet modelling uncertainties:	
ATLAS_WCR_2011_zinv_ZllInv	Wjets_Stat_ZH
ATLAS_WCR_2012_zinv_ZllInv	Wjets_Sys_ZH
ATLAS_ZABCDCR_2011_zinv_ZllInv	Zjets_ABCD_Shape_ee_ZH
ATLAS_ZABCDCR_2012_zinv_ZllInv	Zjets_ABCD_Shape_mm_ZH
	Zjets_ABCD_Stat_ee_ZH
	Zjets_ABCD_Stat_mm_ZH
	Zjets_ABCD_Sys_ZH
Other Background modelling uncertainties:	
SysMJ_J2_T0_L0_Y2012_VjjInv	SysMJ_Shape0mergedMassFail_Y2015_VH
SysMJ_J2_T1_L0_Y2012_VjjInv	SysMJ_Shape0mergedMassPass_Y2015_VH
SysMJ_J2_T2_L0_Y2012_VjjInv	SysMJ_Shape0resolvedMassFail_Y2015_VH
SysMJ_J3_T0_L0_Y2012_VjjInv	SysMJ_Shape0resolvedMassPass_Y2015_VH
SysMJ_J3_T1_L0_Y2012_VjjInv	SysMJ_Shape1mergedMassFail_Y2015_VH
SysMJ_J3_T2_L0_Y2012_VjjInv	SysMJ_Shape1mergedMassPass_Y2015_VH
SysMJ_L2_Y2012_T0_VjjInv	SysMJ_Shape1resolvedMassFail_Y2015_VH
SysMJ_L2_Y2012_T1_VjjInv	SysMJ_Shape1resolvedMassPass_Y2015_VH
SysMJ_L2_Y2012_T2_Spctopemucr_VjjInv	SysMJ_Shape2mergedMassFail_Y2015_VH
SysMJ_L2_Y2012_T2_VjjInv	SysMJ_Shape2mergedMassPass_Y2015_VH
ATLAS_emuCR_eff_2011_zinv_ZllInv	SysMJ_Shape2resolvedMassFail_Y2015_VH
ATLAS_emuCR_eff_2012_zinv_ZllInv	SysMJ_Shape2resolvedMassPass_Y2015_VH
ATLAS_emuCR_stat_2011_zinv_ZllInv	Sysmultijet0mergedMassFailNorm_VH
ATLAS_emuCR_stat_2012_zinv_ZllInv	Sysmultijet0mergedMassPassNorm_VH
	Sysmultijet0resolvedMassFailNorm_VH
	Sysmultijet0resolvedMassPassNorm_VH
	Sysmultijet1mergedMassFailNorm_VH
	Sysmultijet1mergedMassPassNorm_VH
	Sysmultijet1resolvedMassFailNorm_VH
	Sysmultijet1resolvedMassPassNorm_VH
	Sysmultijet2mergedMassFailNorm_VH
	Sysmultijet2mergedMassPassNorm_VH
	Sysmultijet2resolvedMassFailNorm_VH
	Sysmultijet2resolvedMassPassNorm_VH
	WZScaleInEff_ZH
	WZScaleStat_ZH
	WZScaleSys_ZH
	emu_Shape_ZH
	emu_Stat_ZH
	emu_Sys_ZH
Other:	
	PRW_DATASF

Table C.10.: The NP from the Run 1 and Run 2 $H \to$ inv analyses that contribute to the Theory category in the breakdown of systematic uncertainties.

Theory		
Run 1	Run 2:	
V+Jets modelling uncertainties:		
SysWMbb_WbbORcc_VjjInv	SysMbbWShapeOnly_Y2015_VH	
SysWMbb_WbcORbl_VjjInv	SysMbbZShapeOnly_Y2015_VH	
SysWMbb_Wcl_VjjInv	SysWPtV_Y2015_VH	
SysZMbb_ZbORc_VjjInv	SysWbcWbbRatio_VH	
SysZPtV_ZbORc_VjjInv	SysWblWbbRatio_VH	
SysZPtV_Zl_VjjInv	SysWccWbbRatio_VH	
SysWPtV_J2_Whf_VjjInv	SysWclNorm_VH	
SysWPtV_J3_Whf_VjjInv	SysWjetsResVsMerged_VH	
SysWclNorm_J3_VjjInv	SysZPtV_Y2015_VH	
SysWhfNorm_J3_VjjInv	SysZbcZbbRatio_VH	
SysZclNorm_J3_VjjInv	SysZblZbbRatio_VH	
SysZbbNorm_J3_VjjInv	SysZccZbbRatio_VH	
SysWlNorm_J3_VjjInv	SysZclNorm_VH	
SysZlNorm_J3_VjjInv	SysZjetsResVsMerged_VH	
SysWbcWbbRatio_VjjInv	EWK_W-ckkw1_VBF	QCD_W-ckkw1_VBF
SysWblWbbRatio_VjjInv	EWK_W-ckkw2_VBF	QCD_W-ckkw2_VBF
SysWccWbbRatio_VjjInv	EWK_W-ckkw3_VBF	QCD_W-ckkw3_VBF
SysZbcZbbRatio_VjjInv	EWK_W-fac1_VBF	QCD_W-fac1_VBF
SysZblZbbRatio_J2_VjjInv	EWK_W-fac2_VBF	QCD_W-fac2_VBF
SysZblZbbRatio_J3_VjjInv	EWK_W-fac3_VBF	QCD_W-fac3_VBF
SysZccZbbRatio_VjjInv	EWK_W-pdf1_VBF	QCD_W-pdf1_VBF
SysWDPhi_J2_Wcl_VjjInv	EWK_W-pdf2_VBF	QCD_W-pdf2_VBF
SysWDPhi_J2_Whf_VjjInv	EWK_W-pdf3_VBF	QCD_W-pdf3_VBF
SysWDPhi_J2_Wl_VjjInv	EWK_W-qsf1_VBF	QCD_W-qsf1_VBF
SysWDPhi_J3_Wcl_VjjInv	EWK_W-qsf2_VBF	QCD_W-qsf2_VBF
SysWDPhi_J3_Whf_VjjInv	EWK_W-qsf3_VBF	QCD_W-qsf3_VBF
SysWDPhi_J3_Wl_VjjInv	EWK_Z-ckkw1_VBF	QCD_Z-ckkw1_VBF
SysZDPhi_J2_ZbORc_VjjInv	EWK_Z-ckkw2_VBF	QCD_Z-ckkw2_VBF
SysZDPhi_J2_Zl_VjjInv	EWK_Z-ckkw3_VBF	QCD_Z-ckkw3_VBF
SysZDPhi_J3_ZbORc_VjjInv	EWK_Z-fac1_VBF	QCD_Z-fac1_VBF
SysZDPhi_J3_Zl_VjjInv	EWK_Z-fac2_VBF	QCD_Z-fac2_VBF
ATLAS_WPDF_2012_VBF	EWK_Z-fac3_VBF	QCD_Z-fac3_VBF
ATLAS_ZPDF_2012_VBF	EWK_Z-pdf1_VBF	QCD_Z-pdf1_VBF
ATLAS_SherpaQ2EWK_2012_VBF	EWK_Z-pdf2_VBF	QCD_Z-pdf2_VBF
ATLAS_SherpaQ2QCD_2012_VBF	EWK_Z-pdf3_VBF	QCD_Z-pdf3_VBF
	EWK_Z-qsf1_VBF	QCD_Z-qsf1_VBF
	EWK_Z-qsf2_VBF	QCD_Z-qsf2_VBF
	EWK_Z-qsf3_VBF	QCD_Z-qsf3_VBF
Other Background modelling uncertainties:		
SysVVJetPDFAlphaPt_VjjInv	QCD_scale_VV ($\star$)	
SysVVJetScalePtST1_VjjInv	SysWWNorm_VH	
SysVVJetScalePtST2_VjjInv	SysWZNorm_VH	
SysVVMbb_WW_VjjInv	SysZZNorm_VH	
SysVVMbb_WZ_VjjInv	SysMbbVVMEShapeOnly_WZ_VH	
SysVVMbb_ZZ_VjjInv	SysMbbVVMEShapeOnly_ZZ_VH	
SysWtChanAcerMC_VjjInv	SysMbbVVPSUEShapeOnly_WZ_VH	
SysWtChanPythiaHerwig_VjjInv	SysMbbVVPSUEShapeOnly_ZZ_VH	
SysSChanAcerMCPS_VjjInv	SysMbbTTbarShapeOnly_VH	
SysSChanAcerMC_VjjInv	SysTTbarPTV_VH	
SysstopWtNorm_VjjInv	SysTTbarResVsMerged_VH	
SysstopsNorm_VjjInv	SysstopWtNorm_VH	
SysstoptNorm_VjjInv	SysstopsNorm_VH	
SysTChanPtB2_VjjInv	SysstoptNorm_VH	
SysTopPt_VjjInv	OtherTheo_ZH	
SysTtbarMBBCont_VjjInv	ggZZTheo_ZH	
SysTtbarMetCont_VjjInv		
SysttbarNorm_J3_VjjInv		
ATLAS_ZZshape_Generator_2011_ZllInv		
ATLAS_ZZshape_Generator_2012_ZllInv		
ATLAS_ZZshape_PDF_2011_ZllInv		
ATLAS_ZZshape_PDF_2012_ZllInv		
ATLAS_ZZshape_Scale_2011_ZllInv		
ATLAS_ZZshape_Scale_2012_ZllInv		
ATLAS_emuCR_kfac_2011_zinv_ZllInv		
ATLAS_emuCR_kfac_2012_zinv_ZllInv		
All Signal modelling uncertainties, see Table C.8		

Breakdown on the Expected Limit

Table C.11.: The impact of systematic uncertainty groups on the limit on $\mathcal{B}_{H\to\text{inv}}$ in the Run 2 combination. The combined likelihood is fitted to an expected post-fit Asimov dataset with a given group ignored.

	$\Delta\mathcal{B}_{H\to\text{inv}}$(expected)	
Group	Run 2	Run 1+2
Luminosity	0.0053	0.0027
Leptons	0.0207	0.0120
Jets	0.0133	0.0003
Flavour tagging	0.0013	0.0108
$E_{\text{T}}^{\text{miss}}$ soft term	0.0008	0.0005
V+jets modelling	0.0128	0.0114
Other backgrounds modelling	0.0189	0.0141
Signal modelling	0.0028	0.0078
MC statistics	0.0172	0.0134
All experimental	0.0523	0.0337
All theory	0.0276	0.0273
Theory and experimental	0.0908	0.0662
All systematics	0.1150	0.0843

D. Input Search Rankings

Shown are the rankings of the NP in the input searches for the Run 2 combination, and of the Run 2 combination individually.

Run 2 VBF Search Ranking

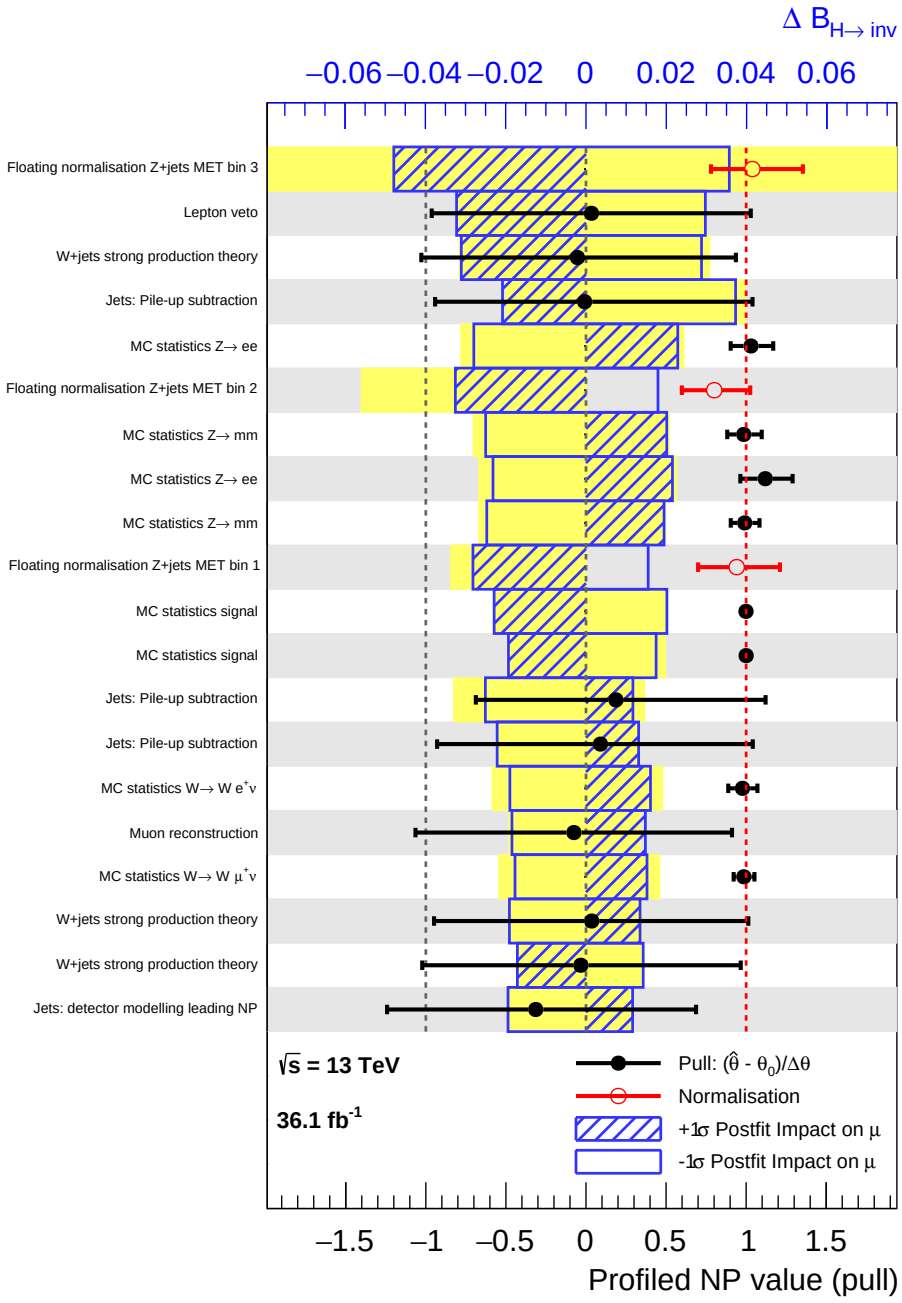

Figure D.1.: The fitted values of NPs for the Run 2 VBF search, ranked according to their impact on $\mu = \mathcal{B}_{H\to\text{inv}}$. Free normalisation parameters are shown in red, and their default value of unity is indicated with the vertical red dashed line. Uncertainties due to the finite size of MC samples have their default value at zero as well.

Run 2 $Z_{\ell\bar{\ell}}H$ search Ranking

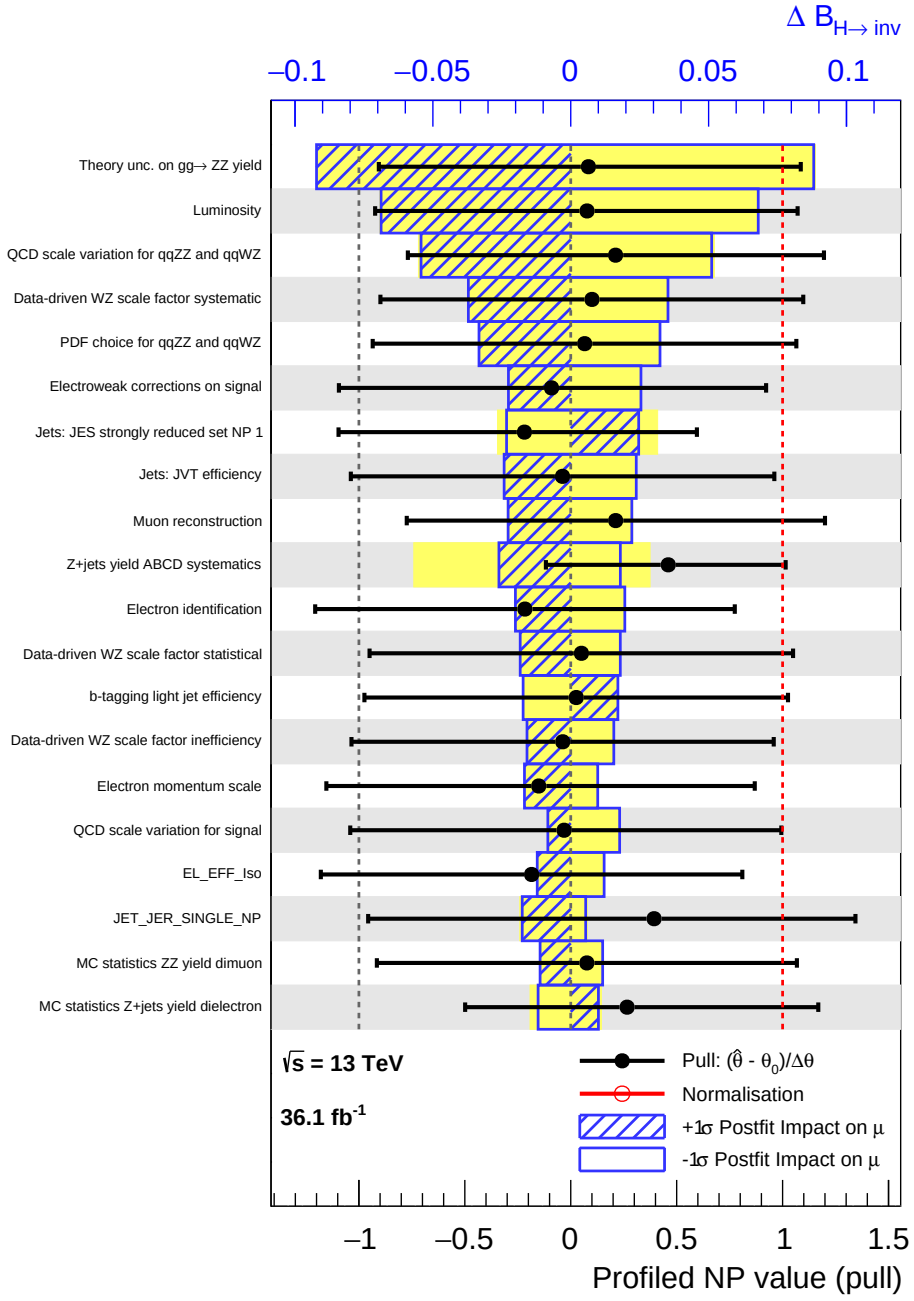

Figure D.2.: The fitted values of NPs for the Run 2 $Z_{\ell\bar{\ell}}H$ search, ranked according to their impact on $\mu = \mathcal{B}_{H\to\text{inv}}$.

Run 2 $V_{q\bar{q}}H$ search Ranking

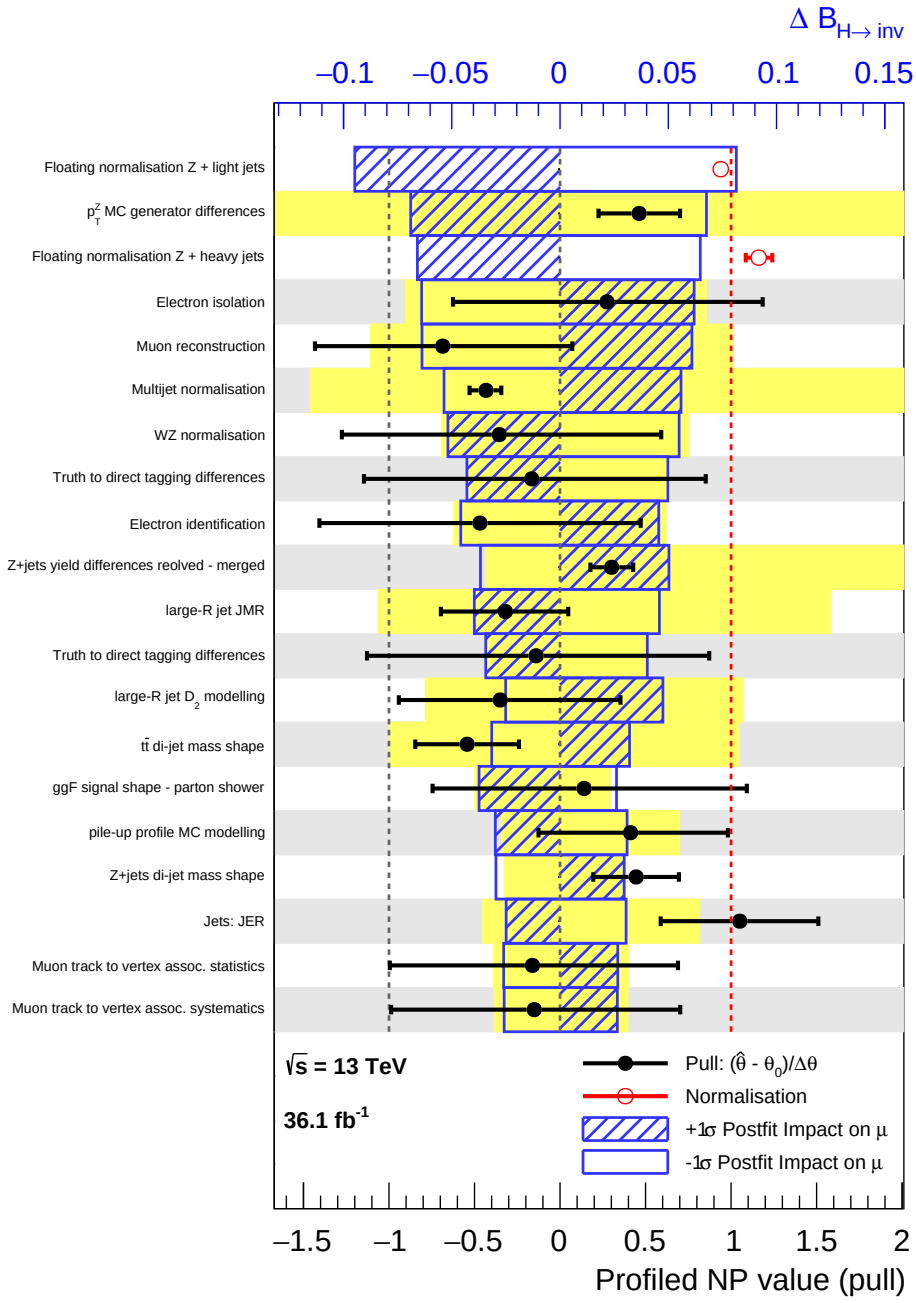

Figure D.3.: The fitted values of NPs for the Run 2 $V_{q\bar{q}}H$ search, ranked according to their impact on $\mu = \mathcal{B}_{H\to\text{inv}}$. Free normalisation parameters are shown in red, and their default value of unity is indicated with the vertical red dashed line. Uncertainties due to the finite size of MC samples have their default value at zero as well.

Run 1 combination Ranking

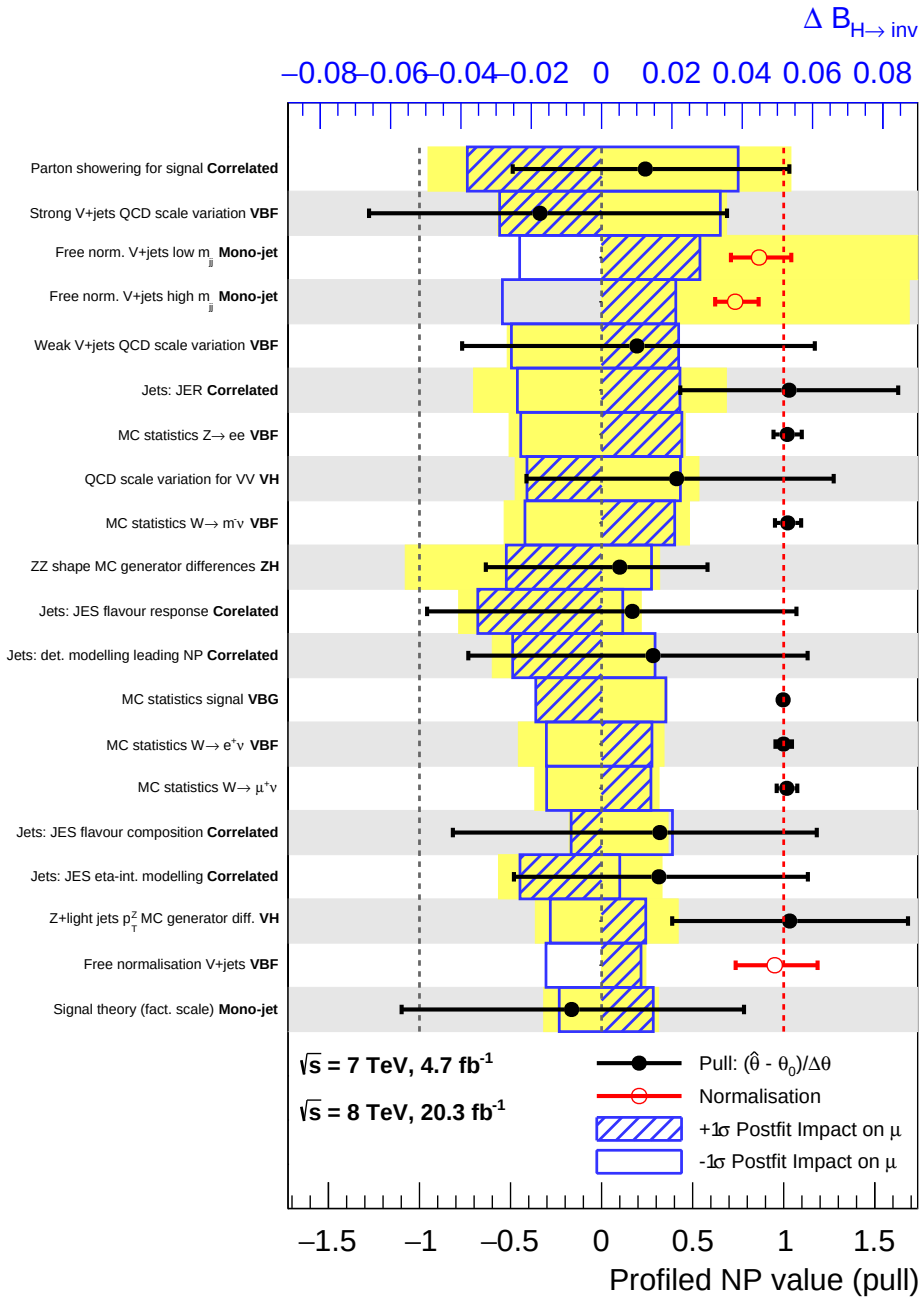

Figure D.4.: The fitted values of NPs for the Run 1 combination, ranked according to their impact on $\mu = \mathcal{B}_{H\to\text{inv}}$. Free normalisation parameters are shown in red, and their default value of unity is indicated with the vertical red dashed line. Uncertainties due to the finite size of MC samples have their default value at zero as well.

Acknowledgements

Foremost, I would like to thank my supervisor, Dr. Oleg Brandt for spending an extraordinary amount of time, energy and thoughts on supporting the combination and its approval process, as well as on my scientific education. He created countless opportunities for me to challenge myself and grow. I also would like to thank Prof. Dr. Hans-Christian Schultz-Coulon, whose experimental lectures taught me the basic principles of physics, and decisively influenced my physical intuition. Furthermore, his lectures on particle physics first woke my interest in working on HEP. Of course, many thanks go to the people of the ATLAS group at the KIP for their insight, technical support and establishing a great atmosphere. Special thanks to my proofreaders Lars, Martin and Falk for ensuring that this work became almost readable. Last but not least I would like to thank my family for their continuous and unconditional support over the time.

Erklärung:

Ich versichere, dass ich diese Arbeit selbstständig verfasst habe und keine anderen als die angegebenen Quellen und Hilfsmittel benutzt habe.

Heidelberg, den .....